POLITECNICO
MILANO 1863

SCUOLA DI INGEGNERIA INDUSTRIALE
E DELL'INFORMAZIONE

Computational hemodynamics for pulmonary valve replacement by means of a reduced Fluid-Structure Interaction model

Tesi di Laurea Magistrale in
Biomedical Engineering - Ingegneria Biomedica

Author: **Elisabetta Criseo**

Student ID: 964653
Advisor: Prof. Christian Vergara[a]
Co-advisors: Dr. Ivan Fumagalli[b], Stefano Maria Marianeschi, MD[c]
Academic Year: 2021-22

[a]Laboratory of Biological Structure Mechanics (LaBS), Dipartimento di Chimica, Materiali e Ingegneria Chimica "Giulio Natta" Politecnico di Milano, Milan, Italy
[b]Modellistica e Calcolo Scientifico (MOX), Dipartimento di Matematica, Politecnico di Milano, Milan, Italy
[c]Cardiac Surgery, ASST Grande Ospedale Metropolitano Niguarda, Milan, Italy.

Abstract

In this thesis we describe an innovative computational approach to study the pulmonary artery hemodynamics of two patients before and after pulmonary valve replacement. The study is carried out by identifying three scenarios for each patient and analysing the differences in the main fluid dynamics quantities between these cases. The study is patient-specific since the computational domains are reconstructed from the CTs of the two patients, provided by the the Division of Cardiovascular Surgery of Milan Niguarda Hospital. Moreover, the models used are calibrated in order to adhere as much as possible to the patients' available clinical data.

The pre-operative scenario aims at reproducing pulmonary artery hemodynamics before pulmonary valve replacement in the absence of the pulmonary valve; this is done using a Computational Fluid Dynamics (CFD) model. The post-operative scenario provides a simulation of the hemodynamics approximately six month after the pulmonary valve replacement and the follow-up scenario aims at representing the patients' hemodynamics 9 years after the pulmonary valve replacement; both these cases are simulated using a reduced Fluid-Structure Interaction (FSI) model in which the 3D fluid model is weakly coupled to a reduced structural model of the pulmonary valve. The 3D models are discretised using the Finite Elements method in space and Backwards Differentiation formula in time, suitable stabilisation methods are applied to guarantee the reliability of the solutions. The 0D model is solved using a 4th order Runge-Kutta Method.

All three scenarios differ by the boundary conditions applied to the artificial boundaries; indeed, the boundary conditions for all three scenarios are obtained using a lumped parameters model of the whole circulatory system calibrated in order to reproduce the available patients' clinical data; this is also solved using a 4th order Runge-Kutta Method.

The results allow to visualise the main changes in hemodynamics induced by the replacement of the pulmonary valve proving the suitability of this approach to reproduce the patients' clinical case.

Keywords: Pulmonary valve replacement, computational hemodynamics, reduced FSI

Abstract in lingua italiana

In questa tesi descriviamo un approccio computazionale innovativo per studiare l'emodinamica dell'arteria polmonare di due pazienti prima e dopo la sostituzione della valvola polmonare. Lo studio è condotto identificando tre scenari per ciascun paziente e analizzando le differenze nelle principali grandezze fluidodinamiche tra questi casi. Lo studio è paziente-specifico in quanto i domini computazionali sono ricostruiti dalle TAC dei due pazienti, ottenute grazie alla divisione di Chirurgia Cardiovascolare dell'ospedale Niguarda di Milano. Inoltre, i modelli utilizzati sono calibrati in modo da aderire il più possibile ai dati clinici disponibili dei pazienti.

Lo scenario pre-operatorio mira a riprodurre l'emodinamica dell'arteria polmonare prima della sostituzione della valvola polmonare in assenza di quest'ultima, utilizzando un modello di fluidodinamica computazionale (CFD). Lo scenario post-operatorio fornisce una simulazione dell'emodinamica circa sei mesi dopo la sostituzione della valvola polmonare e lo scenario di follow-up mira a rappresentare l'emodinamica dei pazienti 9 anni dopo la sostituzione della valvola polmonare; entrambi i casi sono simulati utilizzando un modello ridotto di interazione fluido-struttura (FSI) in cui il modello fluido 3D è debolmente accoppiato a un modello strutturale ridotto della valvola polmonare. I modelli 3D sono discretizzati utilizzando il metodo degli elementi finiti nello spazio e la formula di differenziazione di Backwords nel tempo; per garantire l'affidabilità delle soluzioni vengono applicati metodi di stabilizzazione adeguati. Il modello 0D è risolto con un metodo Runge-Kutta del quarto ordine.

Tutti e tre gli scenari si differenziano per le condizioni al contorno applicate ai confini artificiali; infatti, le condizioni al contorno per tutti e tre gli scenari sono ottenute utilizzando un modello a parametri forfettari dell'intero sistema circolatorio calibrato in modo da riprodurre i dati clinici dei pazienti disponibili; anche questo viene risolto utilizzando un Metodo Runge-Kutta del quarto ordine.

I risultati consentono di visualizzare i principali cambiamenti nell'emodinamica indotti dalla sostituzione della valvola polmonare, dimostrando l'idoneità di questo approccio a riprodurre il caso clinico dei pazienti.

Parole chiave: Sostituzione della valvola polmonare, emodinamica computazionale, modello FSI ridotto

Indice

1 | Overview on physiology and pathology of the pulmonary circulation

1.1. Physiology of the pulmonary circulation

The cardiovascular system comprehends a central pump, the heart, and blood vessels, which have the function of transporting blood from the centre to the periphery of the system and vice versa.

The heart is an organ composed by four cavities, two atria and two ventricles, the cavities are connected by four valves. Anatomically, the four valves can be divided in *semilunar* valves, which are the pulmonary valve (PV) and aortic valve (AV), and *atrio-ventricular* valves, which are the tricuspid valve (TV) and the mitral valve (MV). The aortic valve and pulmonary valve ensure unidirectional flow, respectively, from the left ventricle (LV) to the aorta and from the right ventricle (RV) to the pulmonary artery (PA). The AV and PV have three leaflets, also called *cusps*, which are similar in size and attached to the vessel wall. The free edges of the leaflets meet in the centre of the orifice when the valve is closed, this positioning of the leaflets is called *coaptation*. Moreover, the adjacent leaflets meet at the highest point of their attachment to the wall to form a so called *commissure*. The mitral valve and the tricuspid valve allow blood flow, respectively, from the left atrium (LA) to the left ventricle and from the right atrium (RA) to the right ventricle. These two valves are characterised by a more complex structure than the PV and AV, the leaflets are not equally sized and their geometry is not symmetrical. Furthermore, the leaflets are bound to the inner walls of the ventricle by a cord-like structure called *chordae tendinae*, these has the main function of preventing the collapse of the valve during the systole, when the pressure from the ventricle pushes the closed valve towards the atrium [19, 75].

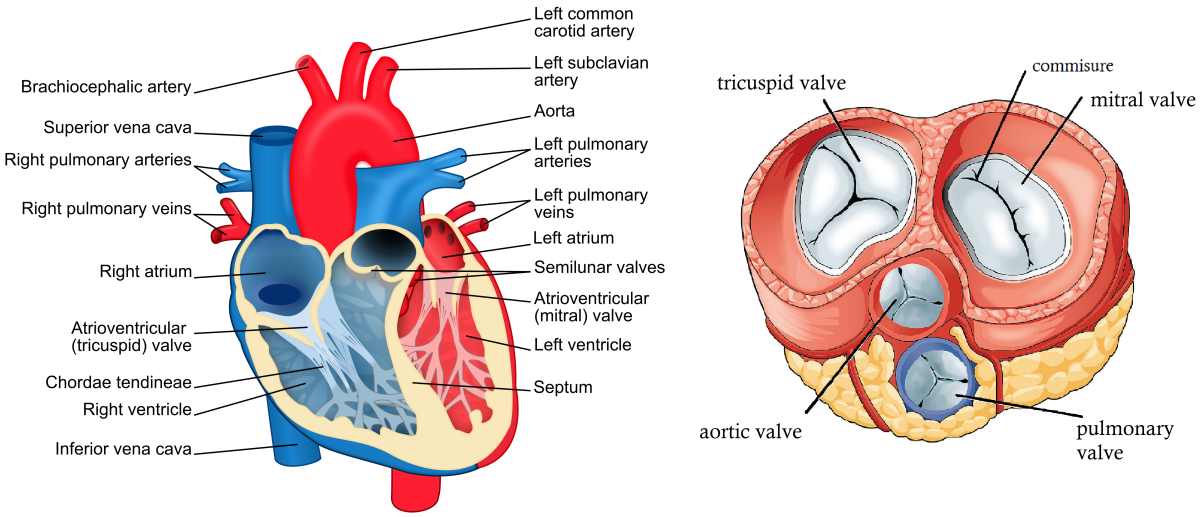

Figure 1.1: Schematic representation of the heart anatomy [70] (left) and cardiac valves anatomy (right).

The main function of the heart as a pump is to establish and ensure circulation of blood throughout the body. Blood circulation in the system can be divided in two main mechanisms: *pulmonary circulation* ad *systemic circulation*.

Pulmonary circulation, mainly, provides blood oxygenation, and so oxygenation of organs and tissues, through the exchange of CO2 and O2 at the alveolae in the lungs. Pulmonary circulation involves the circulation of blood from the right atrium to the pulmonary veins. The right atrium collects blood from the inferior and superior vena cava, this is unoxygenated blood coming from the peripheral districts of the body. Then blood flows from the RA to the RV and is ejected into the pulmonary artery, finally it is transported through pulmonary capillaries and, by gas exchange in the alveolae, oxygenated blood is obtained.

Systemic circulation instead allows the circulation of blood from the heart to the peripheral tissues and organs to allow the distribution of the fundamental nutrients and oxygen. Pulmonary veins bring blood to the left atrium, then it flows into the left ventricle and is ejected into the aorta. Blood is then transported into the system through arteries, gas exchange at the capillaries level allows oxygenation of tissues and then the unoxygenated blood coming from the tissues is transported back to the right atrium through venae cava.

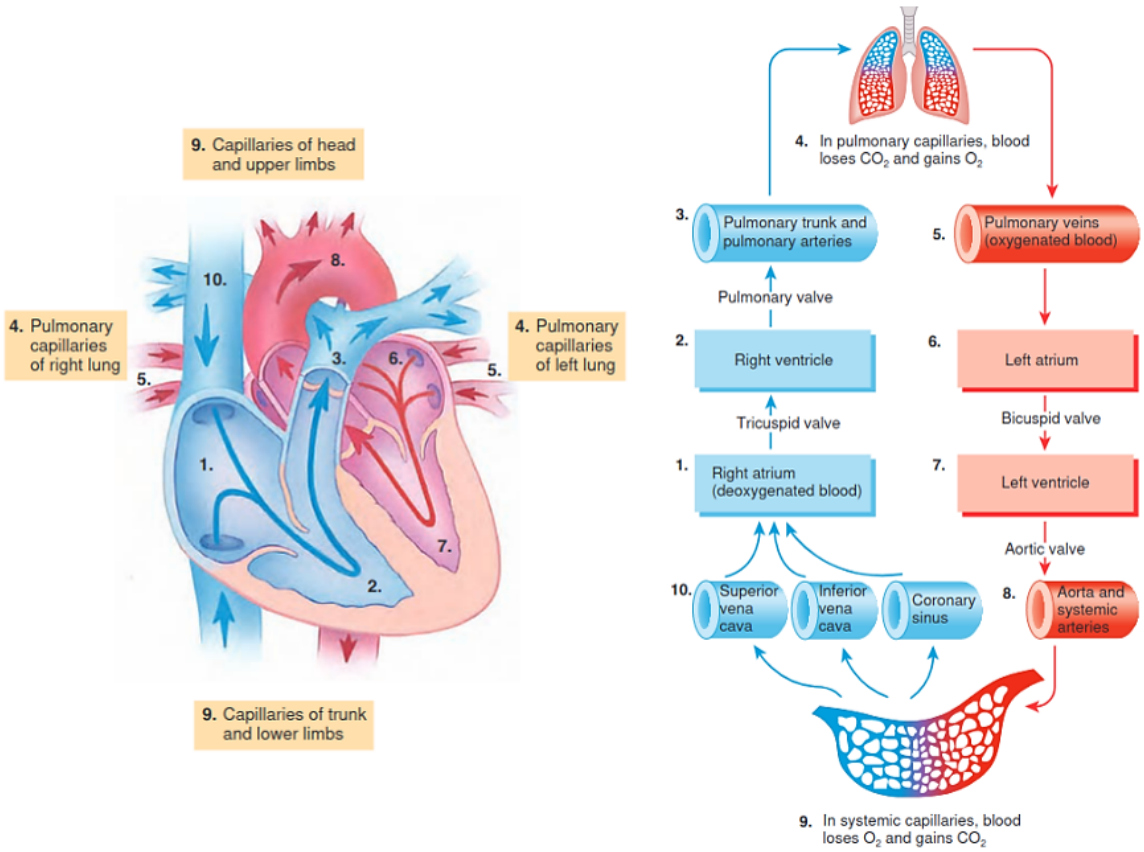

Figure 1.2: Cardiac circulation (left), pulmonary circulation (right, 3 to 5) and systemic circulation (right, 8 to 10) [88]

The heart performs his functions in a cyclic way, each cycle is called *cardiac cycle* and it is characterized by the cyclic contraction and relaxation of the cardiac muscles that determine the blood flow through the heart chambers and then throughout the body. In the cardiac cycle can be distinguished two main phases: *systole* and *diastole*. Since this thesis focuses on the study of pulmonary circulation, the cardiac cycle will be described considering the right ventricle, right atrium and the valves associated to these cavities. The cycle happens identically in the left side of the heart, the main difference regards the pressures developed (figure 1.3). As a matter of fact, the left ventricle is defined as a pressure chamber, the pressure in this chamber reaches 120 mmHg during systole (figure 1.3, top), much higher than the pressure in the right heart, 25-30 mmHg (figure 1.3, bottom). The right ventricle, instead, is classified as a volume chamber, the pressures developed are lower in order to allow the ejection of a blood volume equal to the one ejected by the left ventricle [19].

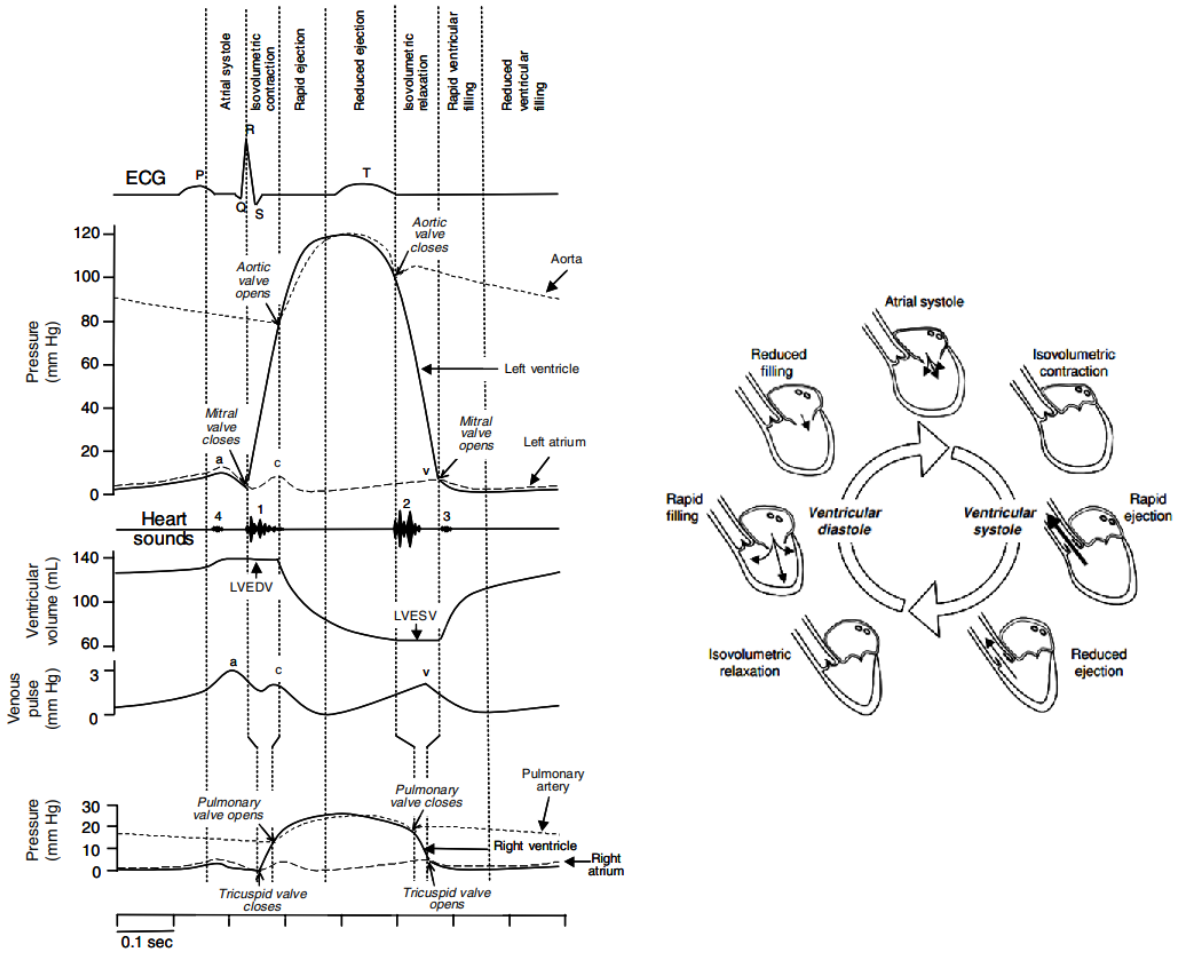

Figure 1.3: Wiggers diagram of the left heart (left, top) and the right heart (left,bottom) and schematic representation of the cardiac cycle (right) [47].

The right ventricular diastole begins when the pulmonary valve is closed, so when the pressure in pulmonary artery exceeds the right ventricular pressure. Indeed, the right ventricle has just emptied establishing a blood flow towards the pulmonary artery and so the pressure has lowered. Following the pulmonary valve closure, an *isovolumetric relaxation* takes place: the ventricle muscle fibers relax without changing the ventricle volume. Due to the isovolumetric relaxation, the intraventricular pressure reduces and becomes lower than the atrial pressure. When the pressure in the atrium is lower than the intraventricular pressure, the opening of the tricuspid valve is triggered and so a unidirectional blood flow from the right atrium to the right ventricle is established.

When the blood coming from the atrium starts to fill the ventricle, a distention of the ventricle muscle fibers takes place, this phase is called *isotonic relaxation* and has the aim to facilitate blood motion from the atrium to the ventricle.

The migration of blood from the atrium to the ventricle determines a decrease in the atrial pressure, so the flow of blood will decrease in time as the pressure gradient across the mitral valve reduces. When the 85% of the ventricle's volume is filled the *atrial systole*, also called *presystole*, takes place. In this phase the contraction of the atrium ensures that all the blood from the atrium passes to the ventricle before the valve closure.

After the presystole, the ventricular systole begins and an *isovolumetric contraction* takes place, the muscle fibers develop tension without shortening performing an isovolumetric contraction. The wall tension determines a rapid increase in intraventricular pressure, which then triggers the tricuspid valve closure while the pulmonary valve is still closed. At this point of the cycle, the chordae tendinae of the TV serve their function as they prevent the collapse of the valve due to the pressure developed in the ventricle. When the intraventricular pressure exceeds the pulmonary artery pressure, the pulmonary valve opens to allow the blood flow from the RV to the right ventricle outflow tract (RVOT) which corresponds to the first tract of the pulmonary artery.

The opening of the pulmonary valve is followed by the *isotonic contraction*, in this phase the maximum pressure in the ventricle is developed and the maximum ejection of blood in the pulmonary artery takes place, since the ventricle reduces its volume due to the muscle contraction. The muscle fibres reduce their length bringing the base of the heart nearer to the apex, the ventricle volume reduces, meanwhile the wall of the atrium relaxes to allow venous return. During the emptying of the ventricle the intraventricular pressure will become lower and lower until the pressure in the pulmonary artery exceeds the intraventricular pressure, in this moment the pulmonary valve will close to avoid the backflow from the artery to the ventricle. At this point of the cycle the ventricular diastole begins, both the tricuspid and pulmonary valve are closed, the wall tension is decreasing and the cycle starts again [19].

The cardiac cycle, in physiological conditions, has a duration of 0.8s, corresponding to a heartbeat of 75 bpm. To evaluate the performance of the heart, some parameters are taken into consideration:

- Stroke volume (SV) is the volume ejected by the ventricle during systole;
- The end systolic volume (ESV) is the residual volume present in the ventricle after the ejection of blood in the systolic phase;
- The end diastolic volume (EDV) is the volume present in the ventricle at the end of the diastole phase;
- The Ejection Fraction (EF), this corresponds to the ratio between the stroke volume

and the EDV.

Table 1.1 summarises the physiological values for these parameters in a healthy adult.

	Left Heart [19]	**Right Heart** [91]
SV (ml)	70	56.6
ESV (ml)	50-60	39-49
EDV (ml)	120-130	91-111
EF	0.55-0.65	0.54-0.57

Table 1.1: Values of SV, ESV, EDV and EF for the right and left heart

1.2. Pulmonary valve dynamics

Cardiac valve dynamics are governed by the force balance computed at the interface between the blood and the valve leaflets. The main forces contributing to the balance are elastic forces related to the leaflets curvature and fluid forces.

The fluid force acting on the leaflets interface is a traction force, consisting of a normal component and a tangential component. During the systole, the fluid traction acts on the leaflets, exceeding the opposing elastic force and causing the leaflets to open; at this point of the cycle, indeed, blood flows through the valve (Figure 1.4, top-left). After the complete opening of the valve the fluid traction tends to invert its direction, adding up to the elastic force and so, all in all, the force balance inverts. Accordingly, in this moment the valve closure begins while the flow rate decelerates (Figure 1.4, top-centre). As the systole is ending, the flow rate tends to reverse, however, the force balance drives the valve closing phase and induces the complete closure of the valve, impeding the generation of a flow going upstream the valve (Figure 1.4, top-right).

Usually, to simplify the description of the valve motion, some contributions to the valve dynamics are disregarded. One of the most used ways to reduce the model complexity, which will be used also in this thesis, is to consider the viscous component of the fluid traction to be negligible with respect to the normal component at the interface between the leaflets and the blood flow. Moreover, on the leaflets surface, the normal component of the fluid traction can be approximated with the pressure; thus, the force of the fluid acting on the valve leaflets is reduced to the pressure jump across the valve [34, 49].

In this way, the dynamics already described can be explained considering the pressure jump across the valve (Figure 1.4, bottom). Specifically, considering the pulmonary valve, when the pressure in the right ventricle (upstream the valve) is higher than the pressure

in the pulmonary artery (downstream the valve), the PV is forced to open. Indeed, the pressure jump wins the elastic forces, thus the ejection of blood from the RV to the PA takes place. After the complete opening of the valve, since the ventricle blood volume is flowing into the pulmonary artery, the intraventricular pressure decreases and the pressure in the pulmonary artery increases. When the pressure downstream the valve becomes higher than the pressure upstream, the effect of the pressure jump adds to the elastic forces and the valve closure is initiated. The flow decelerates and then inverts its direction, thus a backflow is established. However, the pressure jump and the eleastic forces lead to valve closure preventing the backflow from accessing the ventricle; moreover, the blood flowing upstream and near the walls tends to fill the space behind the cusps and distend them, contributing to their closure [19].

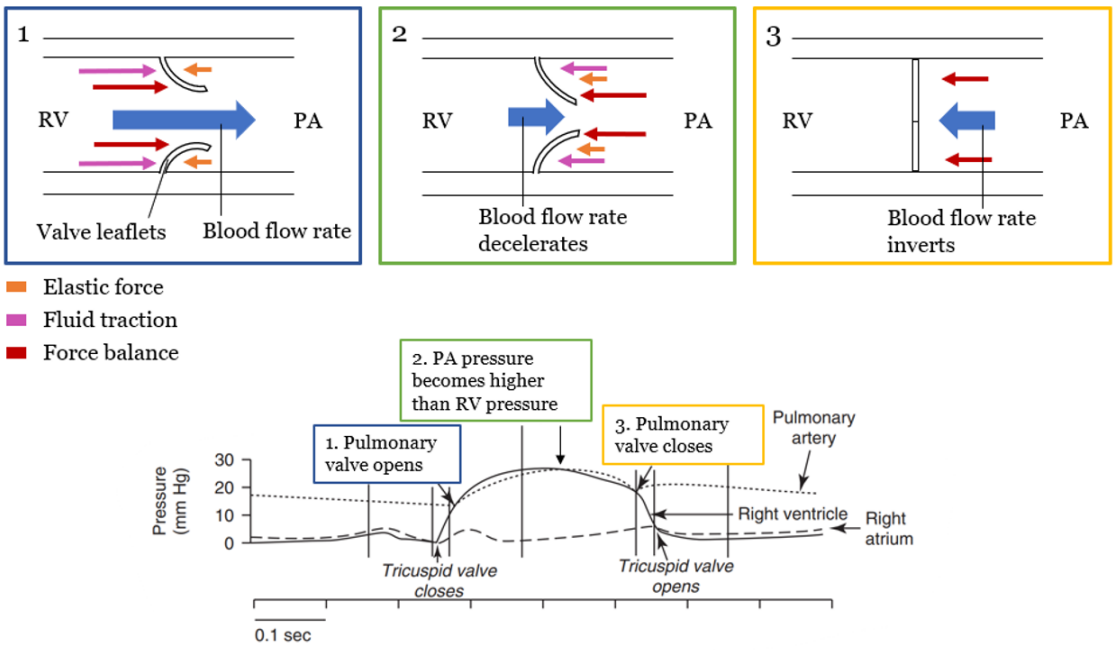

Figure 1.4: Schematic representation of valve opening (top, left) and closing (top, centre and right) and the pressure dynamics associated to valve leaflets motion (bottom).

1.3. Pathologies affecting the pulmonary valve

Pulmonary valve replacement (PVR) will be the focus of this thesis, thus the aim of this section is to describe which are the main causes that lead to the necessity of PV replacement.

A first, general, description of pathologies that can affect the pulmonary valve will be followed by the description of Tetralogy of Fallot, since this pathology can also affect the

pulmonary circulation and cardiac valves, sometimes leading to the necessity of pulmonary valve replacement.

1.3.1. Pulmonary valve pathologies

As stated in Section 1.1, the physiological behaviour of heart valves has the aim of guarantee unidirectional flow during the cardiac cycle. However, cardiac valves functioning could be affected by a pathological behaviour.

Heart valves pathologies can be divided in two types [75]:

- Congenital valve pathologies are a consequence of a congenital heart defect (CHD), an abnormality developed in the fetus. The result of the defect could be an abnormal valve size, anomalies in the shape of the leaflets or even an irregularity in the leaflets attachment;
- Acquired valve disease is related to the age and lifestyle of the patient and is mainly a degenerative disease.

The pulmonary valve could be affected by insufficiency or by stenosis but also unicuspid, biscuspid or quadricuspid arrangements could be present. Symptoms related to these defects could develop from infancy to adulthood, depending on the severity of the patient's condition [45].

Pulmonary valve stenosis determines an impaired blood flow from the RV to the pulmonary artery; the obstruction to the blood flow is caused by a non-physiological valve opening. When this pathology occurs, the valve is characterised by an incomplete opening during the systole, causing a decrease in blood flow to the PA (Figure 1.5, right). Most of the patients do not present symptoms until the narrowing of the orifice during the valve opening becomes significant. If an additional narrowing of the RVOT is present, this condition requires intervention in early childhood. Pulmonary valve stenosis determines, mainly, an increase in the velocity of fluid passing through the valve orifice and an increase in the pressure jump across the valve. In severe pulmonary valve stenosis the maximum velocity of blood reaches $4m/s$ and the pressure jump is $> 60mmHg$ [74].

Bicuspid PV is a rare condition and is often associated with other congenital defects like Tetralogy of Fallot, quadricuspid PV instead is more likely to be asymptomatic but is associated with pulmonary insufficiency (also called pulmonary regurgitation).

Pulmonary valve insufficiency occurs when the blood flow from the RV to the pulmonary artery is not unidirectional, as in physiological conditions. In this case a retrograde flow

is present and it takes place because the cusps of the PV are not competent, i.e. there is not a complete apposition of the cusps in the centre of the valve orifice. So, when the valve should be closed, due to the pressure gradient between the RV and pulmonary artery, a backflow is established (Figure 1.5, left). This can be a mild and well tolerated condition for some patients, as well as a component of a more complex disease. Even if the patients can be initially asymptomatic, this condition determines an increase of load for the RV, which will be processing a higher volume of blood due to the backflow. In time, this leads to progressive volume overload implying RV dilation and ultimately RV dysfunction, arrhythmia and right sided heart failure [37]. Because this condition causes dilation the ventricle, its severity is indicated by the values of the RVEDV and RVESV which could exceed, respectively, $150ml/m^2$ and $80ml/m^2$ [74]; physiological values for these parameters in an adult are $78\pm11ml/m^2$ for the RVEDV and $27\pm7ml/m^2$ for the RVESV [56]. This pathology might be a secondary result of another pathology, as it happens in the case of pulmonary hypertension, or it can be the consequence of intervention for pulmonary stenosis or other CHDs [24, 76].

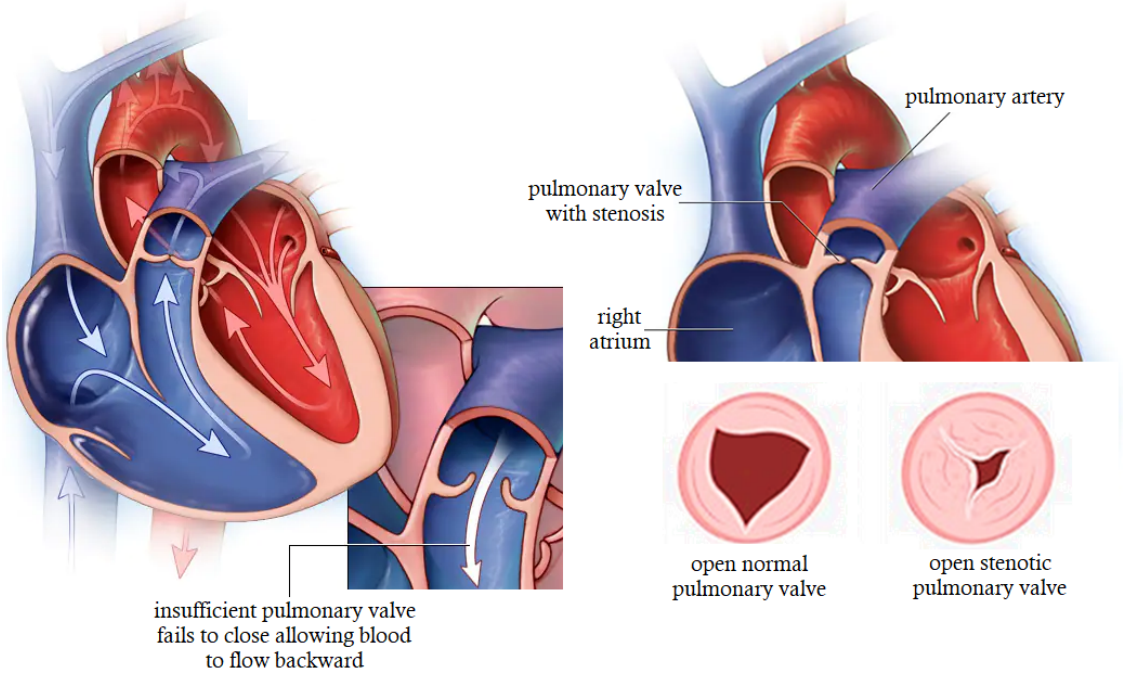

Figure 1.5: Schematic representation of pulmonary valve insufficiency (left) and stenosis (right).

1.3.2. Tetralogy of Fallot

Tetralogy of Fallot (TOF) is one of the most common congenital heart diseases, it is called a *cyanotic* congenital heart disease because the characteristics of the patients carrying this malformation is to be cyanotic at birth. This kind of congenital heart disease is present in 3 of every 10.000 new-borns and accounts for 3 to 10% of all congenital cardiac malformations [3, 7, 79].

Although the severity of the malformations can vary in different patients, the main feature of TOF is a tetrad of anatomical heart defects (Figure 1.6):

- Ventricular septal defect (VSD): it is an opening in the ventricular septum that usually maintains the RV and the LV separated. In TOF the ventricular septal defect is the result of a misalignment and anterior leftward deviation of the *infundibular septum*, this causes the creation of a large and non-restrictive VSD. Moreover, the infundibular septum is a structure that separates the PV from the VSD; due to the defect the septum now sists below the pulmonary valve in the RVOT, causing an obstruction to the flow.
- Right ventricular outflow tract obstruction (RVOTO): this defect, as already mentioned, is linked to the wrong position of the infundibular septum. In most cases, there is also a narrowing of the PV annulus and the PV leaflets are characterised by a thickening and restricted motion. Due to the abnormal flow that is established, also the main and branch pulmonary arteries can develop anomalies. The severity of TOF symptoms largely depends on the severity of the RVOTO. If the RVOTO is moderate, infants maintain saturation values around 90% and do not necessitate immediate intervention at birth, while infants with severe RVOTO feature deoxygenated blood because of a right-to-left blood shunt caused by a stenosis of the RVOT. As a matter of fact, in this case the resistance of the right heart gets higher than the left heart resistance, so a lower volume of blood will flow through pulmonary circulation and so oxygenation of blood will decrease.
- Overriding of the aorta: because of the VSD, the aorta overrides the ventricular septum, thus the inflow of blood in the aorta will be of both oxygenated blood, coming from the LV, and unoxygenated blood, coming from the RV. Indeed, apart from the less common cases in which the severity of RVOTO is mild, the communication between ventricles will be right-to-left.
- Right ventricular hypertrophy: the musculature of the RV is thickened and implies dysfunction of the ventricle [31, 79].

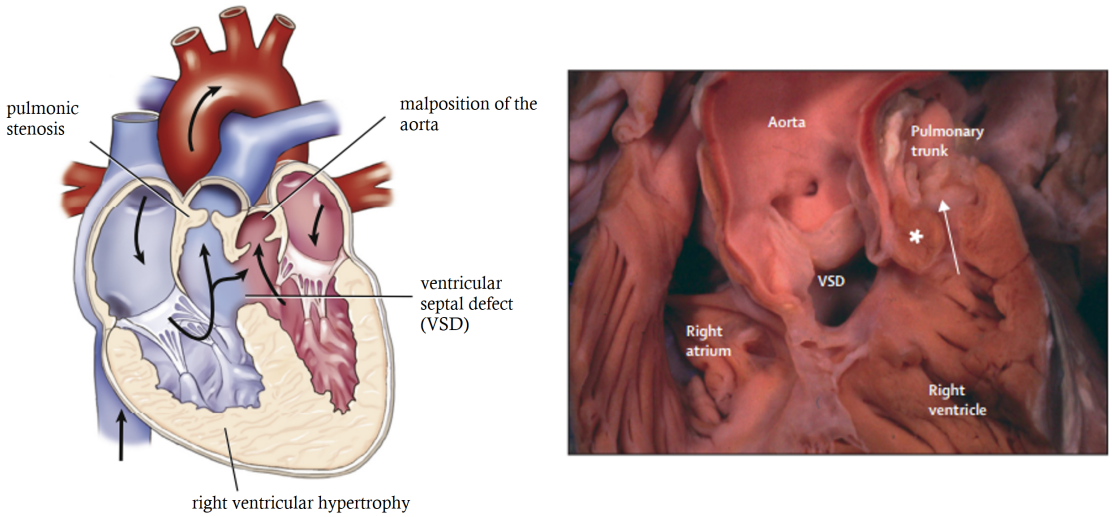

Figure 1.6: Schematic of the tetrad of anatomical features that characterise TOF (left [80]), common morphological characteristics of TOF (right [3]), the arrow indicates the subpulmonary narrowing while the asterisk highlights the malaligned septum.

1.4. Surgical procedures for pulmonary valve and circulation

In this section, the main surgical procedures, used to palliate and repair the pathologies affecting the pulmonary valve and pulmonary circulation, will be described. Subsection 1.4.1 concerns the procedures used to palliate and then repair the tetrad of defects which characterises the TOF. Subsection 1.4.2 is dedicated to the description of *Ross procedure* while Subsection 1.4.3 concerns the main procedures used to replace the pulmonary valve with a prosthetic one.

1.4.1. Palliation and repair of Tetralogy of Fallot

When TOF does not require immediate intervention, commonly palliative surgery is performed on the infant and the repair surgery is delayed of 3 to 6 months, however the best approach is still discussed [3, 31, 79]. Palliation aims mainly at reducing the severity of the RVOTO, to decrease the resistance of the RVOT and improve saturation by increasing the blood flow to the pulmonary arteries. Some of the options for surgical palliation include balloon dilation of the RVOT or its stenting but the most common palliative procedure concerns the use of a systemic-to-pulmonary arterial shunt called *modified Blalok-Taussing shunt* [7, 31, 79]. The use of the modified Blalok-Taussig shunt (mBT shunt) allows forming a connection between the subclavian artery and the PA using a graft (Figure 1.7), in

this way flow to the pulmonary artery, an so oxygenation of blood, is granted[31, 79].

Surgical repair, instead, should ideally ensure the complete closure of VSD, the protection of the RV form and function, moreover the RVOTO should be minimised and include a competent PV. Techniques used in the past included the repair of the VSD by accessing septum through the ventricle, this approach, however, led to extensive resection of the RV wall, of the RVOT and to damage of the PV leaflets. Nowadays, thanks to improvements in the transatrial-transpulmonary approach, the access is performed through the atrium and allows avoiding the scarring and subsequent dysfunction of the ventricle [3, 31].

In the past years, the interest in preserving the competence of the PV has grown more and more. This is because clinicians could observe the long-term outcome of previous surgical approaches, in which the main goal was to obtain a complete relief of the RVOT obstruction even at the expense of a insufficient PV. The incompetence of the PV after the repair, however, has been linked to progressive exercise intolerance, right heart dysfunction due to volume overload, which then leads to ventricular arrythmia and even sudden death [3, 31, 79]. The observation of this progression of symptoms in the patients highlights the importance of protecting the PV function when intervening on the right heart.

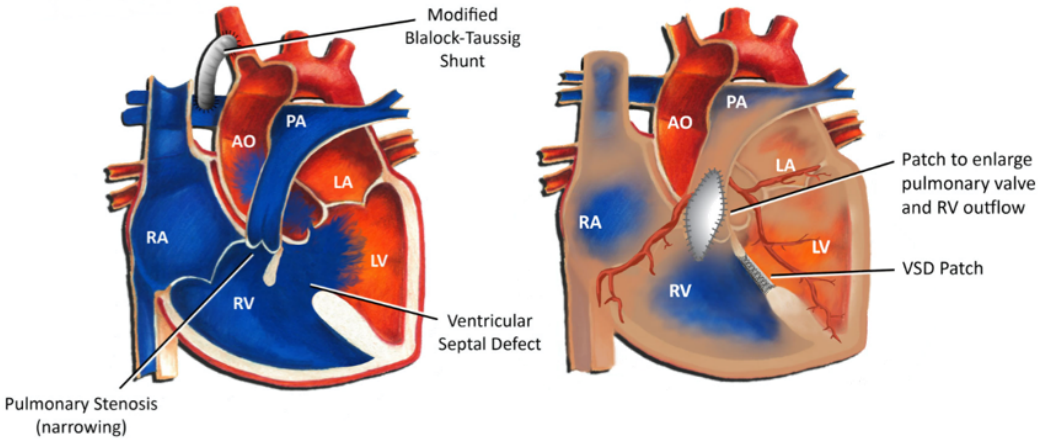

Figure 1.7: An example of palliative surgery using the mBT shunt (left) and of the repair surgery (right) [1].

1.4.2. Ross Procedure

A congenital heart defect like the Tetralogy of Fallot could be characterised by other anatomical abnormalities that are peculiar to the patient considered. In the case of the two patients examined in this thesis, the defect interested also aortic valve and because of it the patients were treated using the *Ross Procedure*.

The Ross procedure consists in a pulmonary autograft, i.e. the aortic valve is removed and substituted with another valve, namely the pulmonary valve, explanted from the patient itself. The pulmonary valve is then substituted with a prosthetic valve. This technique was first described in 1967 by Sir Donald Ross but initially was scarcely adopted by other surgeons because of its complexity. Afterwards, the technique was slightly modified and was performed by more and more surgeons which appreciated the potentiality of the procedure [46].

This technique is beneficial especially to young patients suffering from a CHD that alters the aortic valve physiology because the valve that substitutes the AV is a living valve; this means that it grows and adapts to the patient's physiology and so guarantees superior haemodynamics if compared to the use of mechanical or biological prosthetic valves. Other fundamental advantages of this technique are the possibility to avoid anticoagulant therapy (the valve is not recognised as a foreign object) and the risk of endocarditis [83, 92].

Because the right ventricle could adapt to pulmonary insufficiency without severe adverse effects for a long period of time [24], the pulmonary valve of the patient may not be substituted right after the Ross procedure. This is the case of the patients examined in this thesis. So the patients suffered from pulmonary regurgitation due to the absence of the pulmonary valve.

1.4.3. Pulmonary valve replacement

Pulmonary valve replacement is the substitution of the patient's native PV with a prosthetic one, which can be a mechanical prosthetic valve or a bioprosthesis [48].

This procedure can be carried out by accessing the heart through open heart surgery or by avoiding opening the patient's chest and access the PV position using a catheter. In the fist case the surgeon performs a *surgical valve replacement* while in the second case the procedure is called *transcatheter valve replacement*.

Surgical valve replacement. This technique implies the use of a sternotomy, i.e. the heart is accessed by executing a longitudinal cut in the patient's chest and opening the sternum. Moreover, the patient undergoes *cardiopulmonary bypass*. The blood flow going into the heart is deviated into a reservoir and treated by a machine which oxygenates it and then it is infused back into the patient by using a pump. This allows having a clean field for the surgical intervention to the heart. In the case of surgical valve replacement both mechanical and bioprosthetic valves could be used [16, 78]. This technique is very invasive and may imply some complications linked to the use of cardio pulmonary bypass

[78], however it allows having a direct access to the heart and the opportunity to correct possible residual defects if the patient is affected by CHDs [39].

Transcatheter valve replacement. This procedure is used when the location of the PV is easily accessible by using a catheter, usually a *transfermoral* access or a *trasapical* access is used. In the first case the catheter is inserted in the patient's femoral vein and is advanced until reaching the pulmonary artery, while in the second case the position of the PV is accessed by making an incision on the ventricles apex [44, 82]. This procedure can be performed both using cardiopulmonary bypass or on the beating heart [39] and the prosthetic PV in this case can only be a bioprosthesis. The valve is placed inside a stent featuring a sleeve of biological tissue, the stent is then crimped onto a deflated balloon which is inserted in the catheter, as it is displayed in Figure 1.8.

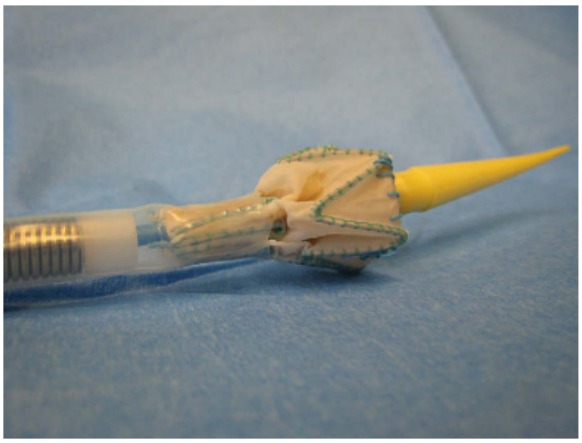

Figure 1.8: A stented valve crimped and partially loaded into its delivery system [44].

During the procedure, the bioprosthetic valve is positioned using a guide catheter, fluoroscopic and echographic imaging allow having a reference for the valve positioning [44, 52]. Once identified the right position for the stent, it is deployed and expanded by inflating the balloon, ensuring the fixation of the stent to the desired position [37, 52, 67]. Examples of this kind of devices are showed in Figure 1.9. This procedure is not free of complications, the stent could fracture and leading to the patient's need for re-intervention; however, this technique can represent a safer, cost-effective and equally efficient option if compared to open heart surgery [82].

Figure 1.9: Two examples of transcatheter valves, Medtronic Melody valve and the Ensemble Delivery system (left) and Edwards SAPIEN XT Valve and the NovaFlex Delivery System (right) [37].

Moreover, the advantage of avoiding an invasive surgery like open heart surgery is crucial for patients with a higher risk for complications like older patients and patients with other coexisting disorders like CHDs [82]. Indeed, patients with congenital heart diseases are subjected to multiple re-operations during their life to allow the correction of their defects and the subsequent side effects, the transcatheter option would reduce the otherwise required repeated sternotomy and improve the long term clinical outcome [37].

This kind of procedure is the same as the Transcatheter Aortic Valve Implantation (TAVI), which is the object of study of many works in both the clinical [20, 42, 50, 61] and computational framework [10, 36, 40, 54, 55]. The use of this technique on the pulmonary valve is more recent and less investigated.

Hybrid procedure. In clinical practice, also a third surgical option has been developed. However, since the device implanted using this procedure will be the focus of this work, the procedure will be described in detail in Section 2.1.

Guidelines on correct timing for PVR. As, previously mentioned, pulmonary valve regurgitation leads to right ventricular volume overload which then causes right ventricular dilation and dysfunction. While it is well established that in this case pulmonary valve replacement is necessary and beneficial [18], the definition of an optimal timing for intervention, regardless of the technique used, is still discussed. Indeed, a threshold for indicators of ventricular function, after which the PVR has not an effect anymore, has

not been identified yet.

According to European Society of Cardiology guidelines [8], the indication of PVR for pulmonary insufficiency relies on the presence of severe pulmonary regurgitation and/or stenosis, this is the case of symptomatic patients. As for asymptomatic patients, the indication of PVR is identified by specific situations: a decrease in objective exercise capacity, progressive RV dilation, progressive RV systolic dysfunction, progressive tricuspid regurgitation or RVOTO with a RV systolic pressure over 80 mmHg. In [33], the indications considered for surgical pulmonary valve replacement were the presence of severe PV regurgitation (with a regurgitant fraction $\geq 35\%$), reduced exercise capacity, atrial and/or ventricular arrhythmia, progressive RV dilation and dysfunction, a RV to LV volume ratio ≥ 1.5 in the presence of symptoms and ≥ 2 in asymptomatic patients.

It should be acknowledged that the clinician might want to delay as much as possible the intervention, in order to avoid the possibility of needing a further substitution of the valve prosthesis, due to the fact that the time of valve deterioration is lower than the life expectancy of the patient. The risk, however, is that delaying too much the operation could lead to the impossibility of normalizing the RV function [33, 64].

Therrien et al. [87] analysed the outcome of PVR for 17 patients, none of the patients with a preoperative RV end-diastolic volume $> 170\ ml/m^2$ or a RV end-systolic volume $>85\ ml/m^2$ showed normalized volumes after surgery. This could indicate that a well-time intervention should be performed before the patient reaches this condition. Also, Oosterof et al. [64] tried to find a threshold value for normalization of the RV volume. In this case it was concluded that normalization could be accomplished when the preoperative RVEDV was $< 160\ ml/m^2$ or if the RVESV was $< 82\ ml/m^2$. However, above this threshold it was still observed an improvement, so there were not found values above which the RV volume did not improve after surgery. Finally, Geva et al. [38] identified indicators of optimal and suboptimal outcome of the transcatheter PVR. An optimal outcome was linked to a preoperative RVEDV $\leq 114ml/m^2$, RV ejection fraction (i.e. the volume of blood ejected by the RV during systole) $\geq 48\%$ and RVESV $< 90\ ml/m^2$. A suboptimal outcome, instead, was connected to a RVEDV $\geq 120ml/m^2$ and a RVEF $\leq 45\%$, particularly if the RVEF was $< 45\%$ a persistent post-operative RV dilation and dysfunction was observed. All these indicators are summed in Table 1.2

Authors	RVEDV	RVESV	RVEF
Therrien et al. [87]	$< 170\ ml/m^2$	$< 85\ ml/m^2$	-
Oosterof et al. [64]	$< 160\ ml/m^2$	$< 82\ ml/m^2$	-
Geva et al. [38]	$\leq 114 ml/m^2$	$< 90\ ml/m^2$	$\geq 48\%$

Table 1.2: Threshold values of RVEDV, RVESV and RVEF connected to a normalization of RV function after surgery.

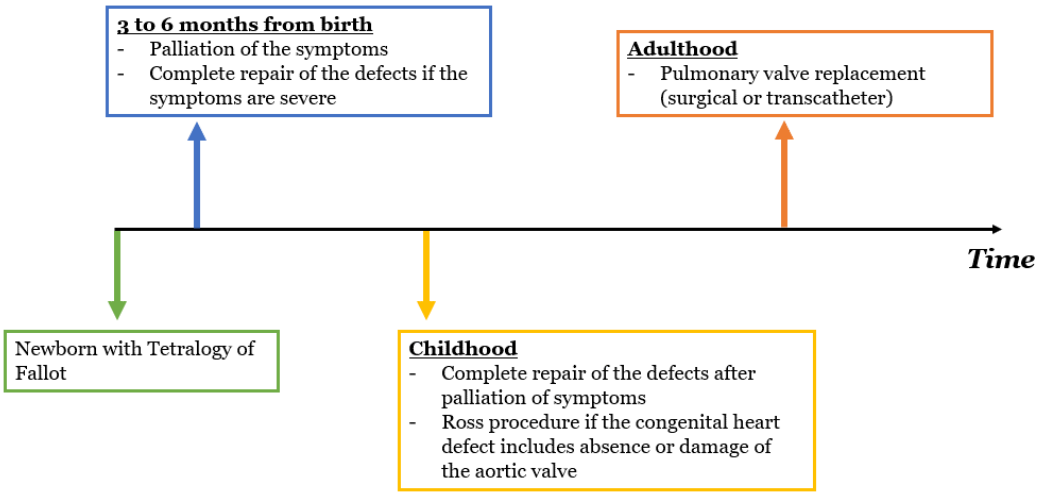

Figure 1.10: Timeline of surgical procedures during the lifetime of a patient affected by Tetralogy of Fallot.

1.5. Mathematical and numerical modelling of pulmonary circulation: State of the art

In the last few decades, mathematical and numerical models have been increasingly used to study pathologies and support clinical research by providing quantitative analyses of various mechanism characterising the cardiovascular system such as electrical activity of the heart or haemodynamics [71].

A relevant aspect to consider when modelling the cardiovascular system is its *multiscale* nature. The events that are involved in the physiological and pathological activity of the heart and the cardiovascular system can take place in a span of months or years, e.g. events such as the formation of aneurysms or atherosclerotic plaques, but also in 0.8 s in the case of the heartbeat or even in a time scale of $10^{-4} ms$, if the event examined is the propagation of the electrical signal which triggers the heart contraction. The same can be

noted from a spatial point of view, the whole cardiovascular system is characterised by a length scale of meters, but if the analysis carried out interests a localised portion the the system the length scale could reduce to cm, for example the flow patterns in the outflow tract of a ventricle, or even mm, e.g. blood flow in the capillaries [30, 68, 69].

It can be useful to simulate the functioning of the whole cardiovascular system, in order to analyse the interaction between different districts. Remembering that the analyses are often used for clinical purposes, the numerical treatment of the problem should have a reasonable computational cost; this implies a sufficiently simple mathematical model, which is still capable to provide the essential data for the assessment of the phenomena considered. These requirements lead to the exclusion of a 3D model to carry out this type of analysis, both because the 3D model for an analysis at a systemic level would have huge computational costs and because it would exceed the accuracy requested for such analysis. In this case are rather used *reduced models*, such as 1D or 0D models of the circulation [30, 68].

One-Dimensional (1D) Models. These models describe the problem using only one spatial coordinate. To characterise the cardiovascular haemodynamics only the axial dynamics are considered, some simplifying assumptions are assigned to apply conservation of mass and momentum along one dimension and a conservative law is introduced in order to establish a relation between the area of the vessel and the pressure to include arterial compliance (i.e. the capacity of the vessel to distend under the forces exerted by blood pressure [70]).

Lumped Parameters Models. In lumped parameters models, or *0D models*, the cardiovascular system is broke down into *compartments* which will be the units constituting the network modelling the whole system. In this case the spatial dimension is not considered anymore, in each compartment the behaviour of the variables of interest, e.g. flow rate and pressure, is described by a set of ordinary differential equations (ODEs) deduced from the application of mass and momentum conservation equations. The system, finally, describes the time evolution of the variables mean values over the compartments. The resulting system is often reinterpreted as an electrical network, associating to the description of the compartment a network of electrical components such as resistances, capacities and inductances; electrical variables such as electrical current and potential are associated respectively to blood flow rate and pressure [30].

This approach is extensively used to study the haemodynamics of the circulatory system. An example is [81] in which a 0D model is used to simulate congenital heart diseases. The model is constituted by a time-varying chamber component, which allows to describe

instantaneous ventricular and atrial pressure–volume relations, and a modified Windkessel component describing the haemodynamics in arterial and venous trees. The combination of these two allows to simulate the activity of the left and right heart, and systemic and pulmonary circulations. This is a simplified model, however, the small time required for the computations makes it a good choice for a clinical use, such as replicate the effect on the haemodynamics of different therapeutic approaches. Indeed, it is highlighted that lumped parameters models could lead to the definition of clinically relevant models that would allow the simulation of the patient's hemodynamic in real time when using data acquired directly from the patient [81].

Three-dimensional (3D) Models. Due to the high computational cost, this kind of model usually comprehends only a small portion of the cardiovascular system, as a portion of vasculature interested by a localised phenomenon. An example of this approach is [84], in which the haemodynamics in the pulmonary artery (both in resting and exercise conditions) are studied. A 3D model of the pulmonary artery is obtained from MRI acquisitions and the computational fluid dynamics (CFD) approach is used to calculate the *Wall Shear Stress (WSS)* on the pulmonary artery. The values of WSS are then analysed in order to understand the relation of this variable to pathology development. This approach has also been used in [85] to study the effects of pulmonary artery hypertension (PAH). In both studies, the 3D model is used as a *stand-alone* model, so the boundary conditions applied, for example inlet and outlet flow rate or pressure, were not computed but simply assigned to the model.

Geometric Multiscale Approach. As already noted, the study of the cardiovascular system interests different scales and, because of this, it can happen that a localised event, developing on a small geometrical scale, is influenced by phenomena acting on a much bigger scale. In this case, the description of the localised phenomena could require an accuracy different from the one used to outline the cardiovascular system on a larger scale. One of the most used approaches, when this kind of problem arises, is the *geometric multiscale approach*. The cardiovascular system is divided in two parts: the zone interested by the localised phenomena is described through a 3D model while the rest of the system is characterised by means of a reduced model (1D or 0D). In this way, the computational cost of the solution is much reduced, but it is still possible to observe the interaction of phenomena acting on different geometrical scales [68, 93, 94].

The 0D and 3D models are then *coupled*, as they have to exchange information, and to do this two algorithmic strategies can be used:

- The reduced model and the 3D model are solved sequentially once at each time step

using different numerical solvers and they exchange information at the interface at each time step;

- The reduced model is solved independently and afterwards the variables values found are passed to the 3D model without feedback. This can be referred to as a *One-way algorithm* and will be adopted in the current work.

In [57] the comparison between the two approaches is analysed with application to the pulmonary artery haemodynamics. Indeed, in this study the 3D model of a pulmonary artery is coupled with a 0D closed model of the cardiovascular system in order to understand if this kind of model could have a clinical relevance. Although the model could still benefit from some improvements, which could lead to more reliable results, the study showed the possibility to use such model to make a comparison between physiological and pathological conditions in the pulmonary artery haemodynamics.

Valve modelling. Valve modelling can be carried out in different ways depending on the approach adopted for the study of circulation. For instance, if a lumped parameters model is used, the cardiac valves are usually mathematically modeled by using a diode, exploiting again the analogy with an electrical network. Indeed, the diode is an element which guarantees a uni-directional flow mimicking the physiological behaviour of heart valves [30, 81].

However, if the valve dynamics are accounted for in a 3D fluid dynamics model, the presence of the valve implied the need to use Fluid-Structure Interaction (FSI). Computational methods for FSI can be divided in:

- *Boundary-conforming methods.* An example is the *Arbitrary-Lagrangian-Eulerian (ALE) formulation*, in which the computational mesh is deformed dynamically to conform to the computational domain boundaries. The practicality of this technique is restricted to simple geometries and small deformations [90], so it can be a useful approach to investigate the cases in which there is a relevance in simulating haemodynamics in arteries with a compliant wall but not when the moving surface performs large deformations as in valve dynamics.

- *Non-boundary conforming methods.* In this case the mesh does not have to conform to the moving boundaries and the effect of the moving immersed body in the fluid is considered by adding, implicitly or explicitly, body forces to the governing equations. Some examples are the *Immersed Boundary (IB) method* and the *Fictitious Domain (FD) method*. In the first case the suitable forces are added to the fluid equation and distributed over the mesh nodes of the fluid domain using a smoothed Dirac

delta function, while in the second case the coupling between the fluid and solid problem is carried out using Lagrange multipliers [26, 90].

Differently from the right heart, the left heart has been extensively studied, so the application of these methods to simulate the effect of heart valves presence on haemodynamics is mostly restricted to the aortic or mitral valve. For instance, in [41] the IB method is used to describe aortic valve fluid dynamics.

A novel computational method for FSI is presented in [26] and [35]. The presence, respectively, of the aortic and mitral valve is accounted for in the computed blood fluid dynamics by means of a *reduced FSI model* based on the *Resistive Immersed Implicit Surface (RIIS) method*. This method is based on the *Resistive Immersed Surface (RIS) approach* proposed in [28] and applied to the aortic valve in [6]. In RIIS method the presence of the leaflets surface is considered by adding a penalisation term (resistive term) which weakly enforces the adherence of blood to the valve leaflets [26].

Recently, this method has been applied to the pulmonary valve in order to study pulmonary artery haemodynamics [60]. Since this approach will be used in this thesis, the model will be further described in Chapter 4.

2 | Clinical context and objectives

In this chapter, the clinical condition characterising the patients analysed in this thesis will be described. Then, the aim of the work will be defined.

2.1. The case study

The two patients, whose data will be used in this study, underwent pulmonary valve replacement surgery in Milan's *Niguarda Hospital*, in order to correct their severe pulmonary valve insufficiency. Indeed, they were born with Tetralogy of Fallot and, after the repair of TOF, their pulmonary valve was removed during a Ross procedure leading to regurgitation.

In *Niguarda Hospital* the optimal timing for surgery is decided by the presence of symptoms but also the RV volume is assessed, for instance an indication for surgery is a RVEDV $> 140\ ml/m^2$. Another indication for surgery is defined using the ratio between EDV and ESV, the surgery is performed if this ratio is ≥ 1.4 for the symptomatic patient or ≥ 2 for the asymptomatic [58].

The implanted valve is the *No-React® BioPulmonic™*, it is composed by a porcine PV covered with a bovine pericardium sleeve, these two elements are then mounted on a Nitinol stent (Figure 2.1). The stent has the characteristic to be self-expandable so, when the valve is injected, it expands without the aid of a balloon. Both the pericardium sleeve and the porcine valve are affixed with glutaraldehyde and then detoxified using a proprietary process called *No-React®*, during which any free residual aldehyde is eliminated from surfaces.

One of the benefits of using this valve is that it is implanted with a *hybrid procedure* which puts together the advantages of both the surgical and the transcatheter ones. Indeed, unlike the transcatheter approach, the surgical procedure allows the implantation of valve prosthesis without access limitations and offers the opportunity to intervene on other residual defects that could be present in the heart of patients affected by CHD. Moreover, this injectable valve prosthesis allows the implantation either on cardiopulmonary bypass

or on the beating heart if the patient's pathology does not require additional procedures. Finally, it is designed to be less obstructive thanks to the low profile and a soft stent which reduces the stretch on the annulus and the risk of coronary artery obstruction. Differently from other valves designed for surgical implantation, this device lacks of a suture ring, this allows the implant of a larger prosthesis (diameter ranges from 15 mm to 30 mm), avoiding right ventricle outflow tract obstruction and maintaining laminar flow inside the valve.

Figure 2.1: The *No-React® BioPulmonic™* prosthetic valve [39].

To be positioned, the stented valve is crimped and inserted into the barrel of the delivery trocar (figure 2.2 left), then it is performed an incision on the right ventricle outflow tract and the valve is inserted into the main pulmonary artery (figure 2.2 right). When the delivery system is retracted, the valve expands and the Nitinol becomes more rigid, since it is exposed to heat as it comes in contact with the tissue. Lastly, the prosthesis is fixed with 4 stitches through the pulmonary wall. This technique requires minimal mobilization of the heart and great vessels so it reduces the operative time and the risk linked to the surgery. Furthermore, this device, having a larger diameter, grants subsequent valve-in-valve implantation if needed, allowing the clinician to correctly plan future re-operation often needed in patients with CHD [39].

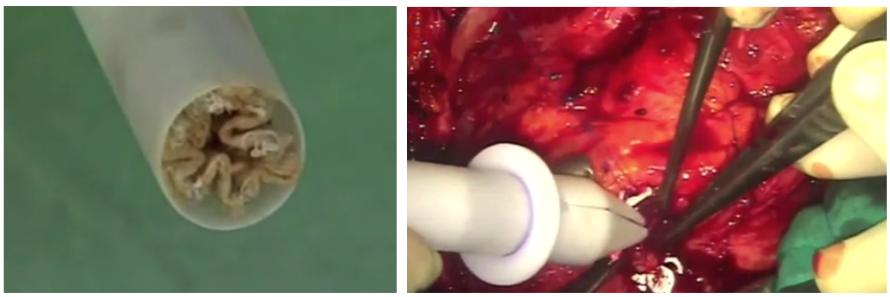

Figure 2.2: Crimping (left) and delivery (right) of the *No-React® BioPulmonic™* prosthetic valve [39].

2.2. Aim of the work

The aim of this thesis is to analyse the haemodynamics in the pulmonary artery using a computational model to reproduce the blood fluid dynamics before and after pulmonary valve replacement performed with a stented bioprosthesis. The study is patient-specific; indeed, it is carried out using as computational domain the three-dimensional pulmonary artery geometries of two patients which were reconstructed from clinical imaging provided by the *Niguarda Hospital* of Milan.

The analysis will comprehend the simulation of three scenarios for each patient:

- A pre-operative scenario, characterised by pulmonary valve insufficiency. In this configuration, the model of the pulmonary artery is characterised by the absence of the pulmonary valve since, as already mentioned, the patients underwent Ross procedure.
- A post-operative scenario, describing the patient's condition approximately 6 months the pulmonary valve replacement. In this case, the fluid-structure interaction between the valve leaflets and the blood is modeled.
- A follow-up scenario characterising the patient's condition approximately 9 years after the pulmonary valve replacement. Also in this scenario, the interaction between the blood and valve leaflets is included in the model.

The temporal distinction between the three scenarios will allow having an overview on the effect of such intervention on the pulmonary artery haemodynamics; moreover, considering two different patients allows to analyse the diversification of the effects observed when different geometries are considered.

To implement the three scenarios described above, the following models have been adopted:

- A closed-0D model of the whole cardiovascular system to extract pressure boundary conditions which are then applied to the artificial boundaries of the three dimensional models describing the pre-operative, post-operative and follow-up scenarios. Notice that the 0D model of the circulation has been characterised differently for each scenario in order to obtain three sets of pressure: each one of these pressure sets will be applied as boundary condition of the respective scenario;
- A 3D Computational Fluid Dynamics model of the pulmonary arteries haemodynamics, in the case of the pre-operative scenario;
- A reduced FSI model which employs the Resistive Immersed Implicit Surface (RIIS)

method, for the post-operative scenario and follow-up scenario. This approach consists in modelling the interaction between the blood and the valve leaflets by adding to the fluid conservation of the momentum equation a resistive penalty term which weakly enforces the adherence of the fluid velocity to the leaflets velocity in proximity of the valve surface. The model is *reduced* in the sense that the structural model for the valve is a reduced 0D model.

Concerning the modeling choices of this thesis, the post-operative and follow-up scenarios are described using the same geometry and reduced FSI model: their differences lay in the boundary conditions applied, as explained in Section 4.2.

The haemodynamics in the pulmonary artery are studied to verify how the presence of the stented valve affects fluid dynamics quantities such as the velocity of blood, pressure and wall shear stress on the pulmonary artery walls. Specifically, it can be interesting to exploit the model in order to analyse the recovery of the physiological haemodynamics condition after the treatment of the pulmonary valve insufficiency.

Since most of the studies on cardiac valve replacement concentrate on the aortic and mitral valves, this study could give an additional point of view in the analysis of cardiac valves behaviour as it takes into consideration the pulmonary circulation and prosthetic pulmonary valve dynamics, which are far less observed.

This thesis consists in a follow-up of the work already carried out by [60] and [21]; the main novelty with respect to [21] is the use of a reduced FSI model for the pulmonary valve, instead of a diode. Moreover, with respect to the work presented in [60], here the lumped parameters model of the circulation is calibrated to reproduce as much as possible the conditions of the patients considered, so that the boundary conditions imposed to the 3D models are patient-specific.

In Chapter 3, the preprocessing techniques used to obtain the domains of the numerical model for patients are described. Chapter 4, is dedicated to the description of the numerical method used to model the problem. Chapter 5, instead, concerns the definition of the settings used for the simulations and the discussion of the results for each patient in the two scenarios. Finally, in Chapter 6 limitations and possible further developments of the work will be presented.

3 | Imaging and Preprocessing

Clinical data in this thesis is of utmost usefulness since it allows obtaining a patient-specific computational domain for the simulations. Indeed, the computational domain is segmented and reconstructed starting from CT acquisitions of the two patients. These were provided by the Division of Cardiovascular Surgery of the Department of Cardiology of Niguarda Hospital.

The preprocessing necessary to obtain the computational domain and the meshes was carried out using three tools:

- *VMTK (Vascular Modeling ToolKit)*: a collection of libraries and tools for 3D reconstruction, geometric analysis, mesh generation and surface data analysis for image-based modeling of blood vessels [25, 89];
- *Paraview*: an open source post-processing visualization engine which allows building visualizations to analyse data quickly [65];
- *Matlab*: a programming platform which allows building quickly algorithms for data analysis [59].

The fluid computational domain corresponds to a portion of the patients' pulmonary artery. In the following sections, the preprocessing of the pulmonary artery clinical images will be detailed in order to describe the reconstruction process which allows to obtain the geometries for both the pre-operative (Section 3.2) and post-operative scenarios (Section 3.3) and then generate the computational mesh of the fluid domain (Section 3.5). Specifically, in the post-operative case the geometry reconstruction involves not only the pulmonary arteries but also the inclusion of the pulmonary valve in the domain, as it will be described in Section 3.4.

3.1. Acquisition and segmentation of the pulmonary artery geometries

The clinical images used for the domain reconstruction were acquired using Computed Tomography (CT) imaging with a contrast agent. This technique consists in using a narrow beam of x-rays generating from a source which rotates around the body of the patient lying supine; x-ray detectors are located directly opposite to the source so, as the x-ray go through the patient's body, they are picked up by the detectors and then transmitted to a computer. The different x-rays absorption properties of the tissues in the body allow the visualisation of the structures in a 2D image [62, 70].

For each turn of the x-rays beam around the patient's body, a 2D slice of the patient is constructed and the thickness of the tissue pictured in each 2D slice usually ranges from 1 to 10 mm depending on the machine used. When a slice is completed, the patient's bed is moved forward in order to allow the construction of another 2D slice. Finally, the acquisitions obtained can be either analysed individually or stacked together by the software in order to generate a 3D image.

Since the detection of soft tissues using x-rays can be difficult, contrast agents are often used when there is the necessity of visualise the circulatory system. In particular, the contrast agent is injected in the bloodstream to enhance the detection of blood vessels. This technique can be used to evaluate possible abnormalities or obstructions to the flow [62].

Medical images could be affected by noise, which could decrease the quality of the pre-processing results. Therefore, before reconstructing the geometry, usually an imaging enhancement step is performed [70].

Finally, the medical acquisitions are converted from the DICOM format, which is the standard for CT imaging, in the MetaImage MetaHeader (mhd) format. This format allows the representation of medical images on three planes at the same time, the planes can be tilted or translated to identify the zone of interest [21].

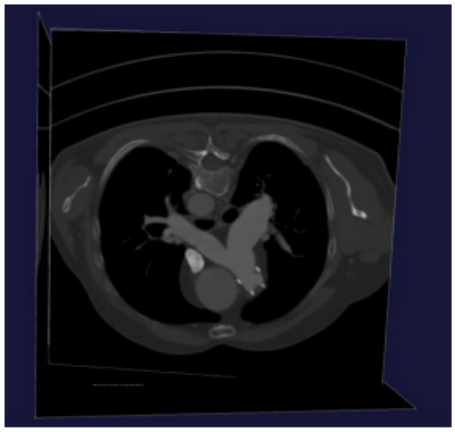

Figure 3.1: An example of a CT representing the pulmonary artery visualised using VMTK [21].

Using the images in mhd format, the first step necessary to obtain the computational domain of the patients is *segmentation*. The aim of this procedure is to construct the shape of the vessel from the image, obtained after the enhancement step, by identifying the points belonging to the boundary of the vessel [70]. Moreover, it is the point in which the distinction between *physical boundaries* and *artificial boundaries* is performed. Indeed, the boundaries characterising the final geometry can be divided in two types: the boundaries identified by the geometry itself are physical boundaries while the ones created by the user when establishing the zone of interest are artificial boundaries. This distinction is shown in Figure 3.2.

The segmentation process was carried out by [21] and [66] using the *thresholding* method. This method consists in selecting a threshold k, which corresponds to an intensity value in the grey-scale that separates different anatomical structures, specifically the lumen of the vessel from the artery wall. The aim of the method is to isolate the points in which the intensity is higher than the threshold. After the best value for k has been chosen, the *front propagation* technique is applied. So, the propagation of a suitable wavefront is tracked, in particular, the wavefront slows down where the gray-scale intensity value changes rapidly, namely near the boundary. Following this technique, only the structure of interest, so the lumen of the vessel, will be extracted from the medical images and the background will be excluded. Finally, it was reconstructed, for both patients, the part of the artery containing the valve stent, since the artifacts in the image given by the presence of the stent made the initial reconstructions particularly irregular [21, 70]. The final geometry obtained using this process is shown in figure 3.2.

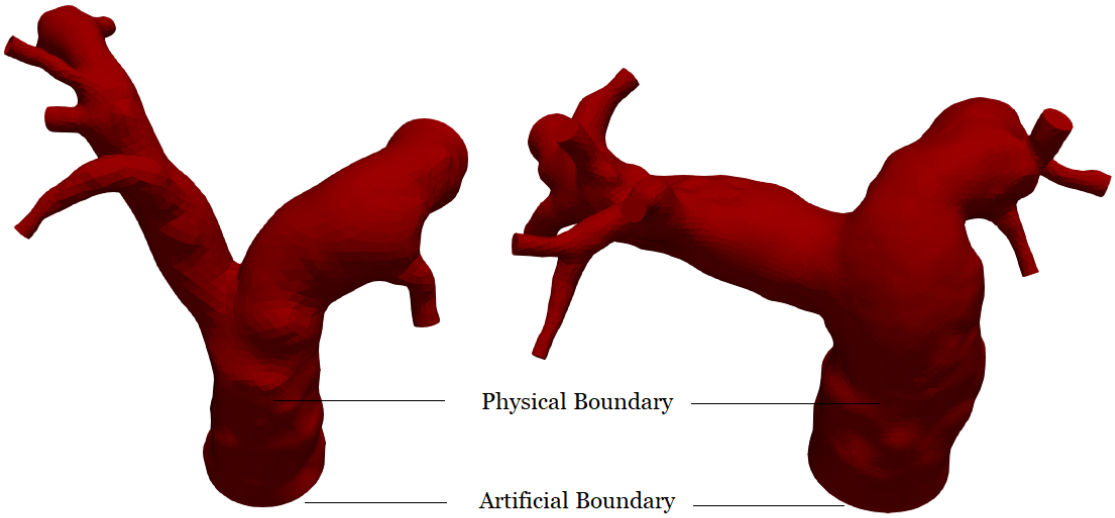

Figure 3.2: Results of the segmentation process for Patient 1 (right) and Patient 2 (left)

3.2. Computational domain definition for the pre-operative scenario

The geometry obtained from the previous preprocessing step was then further modified to obtain the final computational domain. In particular, the segmented pulmonary artery was composed by one inflow zone, the *pulmonary trunk*, and multiple outlets; however, the haemodynamics are affected by the pulmonary valve replacement mainly in the pulmonary trunk and in proximity of the first bifurcation.

Therefore, the geometry was modified on Paraview, using the *clip* functionality, in order to obtain a domain constituted by the pulmonary trunk and two outflow zones which correspond to the two branches originating from the first bifurcation of the pulmonary artery. Moreover the pulmonary trunk was cut using the same method such that the inlet of the pulmonary trunk was corresponding to the inlet of the stent, identified on the CTs in a previous work [21]. Hence, the pre-operative scenario and the post-operative scenario (defined by the presence of the stent) are characterised by a domain having the same length of the inflow zone, this allows having more comparable results between the two scenarios. After these modifications, which led to an open geometry and the presence of orifices on the two main branches, the VMTK command *vmtksurfacecapper* was applied in order to obtain a closed surface which corresponds to the pre-operative geometry.

This process is carried out both for Patient 1 and Patient 2, as shown in Figure 3.3.

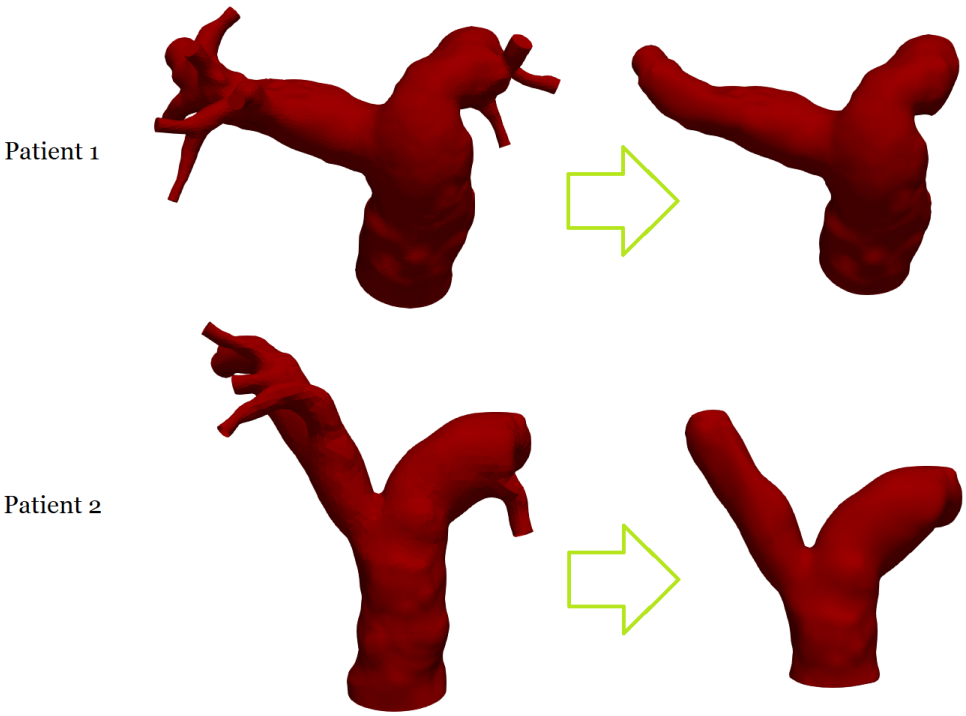

Figure 3.3: The pulmonary artery geometries before and after the modifications used to obtain the computational domain for the pre-operative scenario

3.3. Computational domain definition for the post-operative and follow-up scenarios

The geometry used for the post-operative and follow-up scenarios is different from the one used in the pre-operative case. Indeed, the geometry in which the blood flows after the pulmonary valve replacement is much more regular if compared to a physiological geometry because of the presence of the stent and pericardial sleeve. Therefore, it was decided to include this aspect in the model.

The stent geometry was not reproduced exactly, however, as in a previous work [21], it was decided to model its presence using a cylinder which has the same length (20 mm) and diameter (29 mm) as the valve. Even if the stent shape is characterised by specific angles, this is still a fairly accurate way of modelling the stent presence, since what comes in contact with blood is only the internal part of the stent which is more rounded. Finally, in [21], the cylinder was positioned and directed in the same way as it was observed in the CT scans of the two patients using the VMTK command *vmtkicpregistration*, which translates and then iteratively rotates the cylinder in order to adapt the shape as much

as possible to the points seeded on the CT scans.

Having the cylinder model, its connection to the pulmonary artery geometry was performed. To obtain the final geometry, two steps were followed. The pulmonary artery obtained for the pre-operative scenario was cut using the *clip* command on Paraview to discard the part of the pulmonary trunk in which the pulmonary valve is located.

Then the command *vmtksurfaceharmonicconnect* was used to generate a continuous surface between the cylinder and the pulmonary artery by deforming its boundary surface, the deformation is extended through a harmonic map [25]. The result of this process is shown in Figure 3.4 both for Patient 1 and Patient 2.

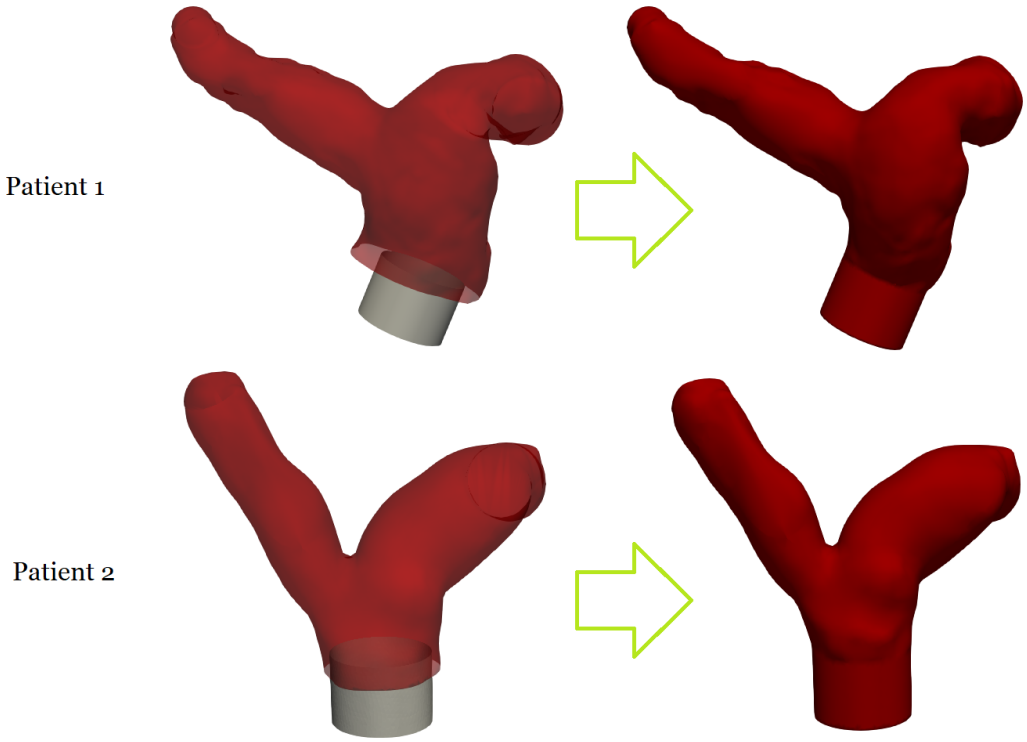

Figure 3.4: Patient's 1 and Patient's 2 pulmonary artery geometry before and after connecting the cylinder modelling the stent.

3.4. Pulmonary valve reconstruction

The valve used in the post-operative case was not reconstructed from the CTs of the patients, this was due to the low resolution of the available medical images which made the leaflets not recognisable. Instead, it was employed a valve model provided by MOX Laboratory of Politecnico di Milano, developed for the iHEART project starting from a

model obtained by Zygote [95].

In a previous work [60], the valve had already been adapted to the stentless pulmonary artery geometry of the patients considered in the current work. So, the valve used had already been correctly oriented but it had to be resized in order to fit the pulmonary artery geometry featuring the cylinder modelling the stent. The process was carried out in the same way both for Patient 1 and Patient 2.

To resize the valve, a scaling factor had to be identified. This was carried out by considering the size ratio between the pulmonary artery circumference and the cylinder circumference. In fact the valve, already oriented, had been resized to fit in the pulmonary trunk whereas, in this case, it had to fit in the cylinder representing the stent. Once the ratio was found, it was used the VMTK command *vmtksurfacescaling* to modify the valve size. Afterwards the valve was positioned and centered in the cylinder using the VMTK command *vmtkicpregistration* and considering as references the commisures previously identified on the CTs and the circumference of the cylinder.

Afterwards, the valve was modified to fit the walls of the cylinder. To do so, using the command *vmtksurfaceharmonicsolver* the valve surface points were assigned values going from 0 in the centre of the valve to 1 in the outer surface of the valve and stored in an array called *phi* (Figure 3.5, left).

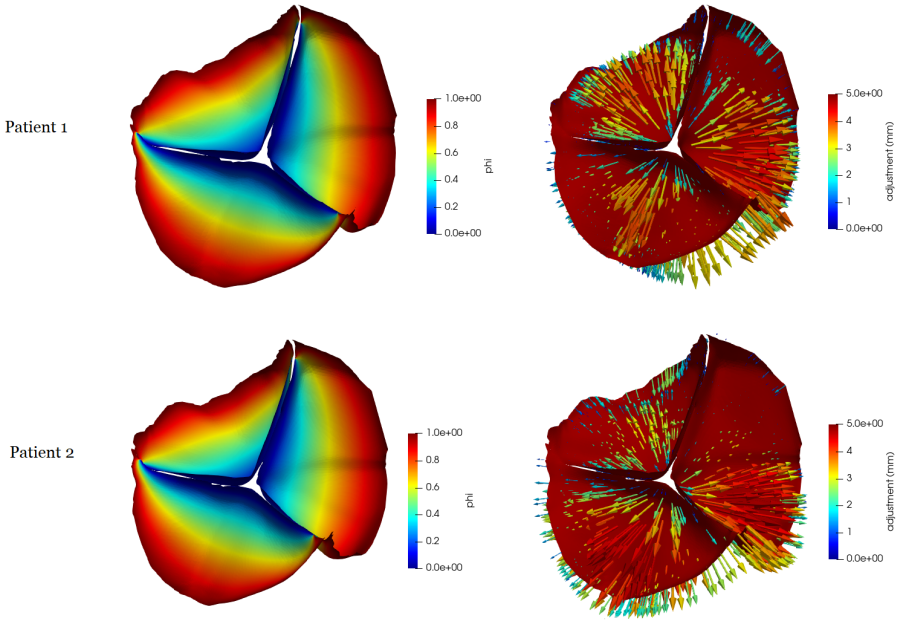

Figure 3.5: The representation of *phi* on the leaflets surface (right) and the adjustment imposed to the leaflets surface during the process (left).

Then, with the VMTK command *vmtksurfacedistance* the distance between the cylinder and the valve was stored in another array for all the points of the valve. Finally, using the functionality *warp by vector* in Paraview the valve was modified using as input a vector given by the multiplication of the function phi by the distance calculated previously. In this way the valve shape was adapted mostly moving the outer surface of the leaflets while the centre was kept in position (Figure 3.5, right). Using this process, the geometry of the valve in the closed configuration was obtained.

To find the open configuration of the valve a similar procedure was followed. In particular, a value going from 1 in the centre to 0 in the outer portion of the valve surface was defined; these values were stored in the array called *alpha*.

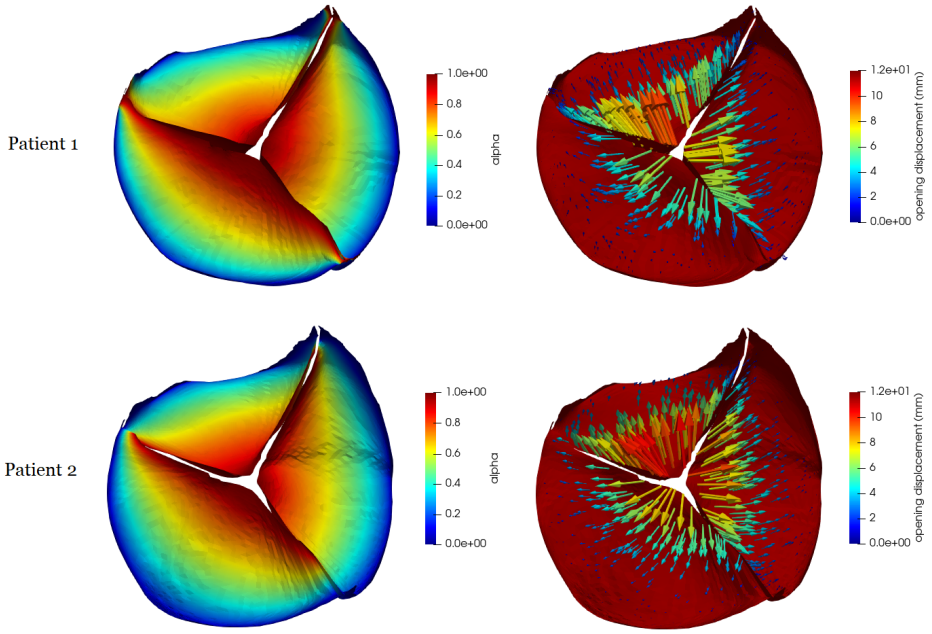

Figure 3.6: The array *alpha* displayed on the leaflets surface (right) and the displacement imposed to the leaflets surface to approximate the physiological behaviour of the valve in the open configuration (left).

Then, each leaflet was modified individually using the Paraview command *warp by vector* and giving as input vector the result of the multiplication between the array *alpha* and the distance from the arterial wall (calculated as described previously). This method implied the application of a null transformation to the outer part of the leaflets, allowing to keep them correctly positioned, while in the internal part the leaflets was modified in order to mimick as much as possible the physiological opening of the valve (Figure 3.6). The results of this process for all the three leaflets were then stored in a single file and the

array governing the opening of the leaflets was stored; indeed, this array will represent the prescribed motion of the leaflets given as input to the simulations.

The final result of the valve preprocessing is shown in Figure 3.7.

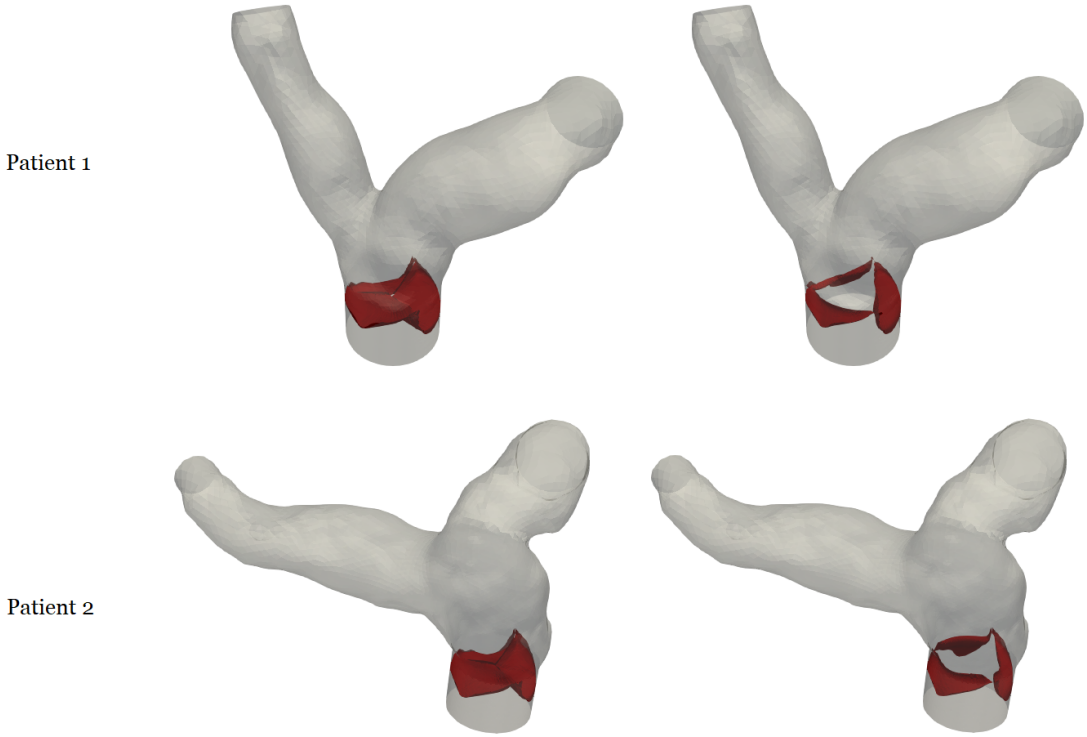

Figure 3.7: Closed (left) and open (right) configurations for the pulmonary valve geometry of both Patient 1 and Patient 2.

3.5. Mesh generation of the pulmonary artery geometries

The final step to obtain the computational domain is the mesh generation, this process was carried out in the same way for the pre-operative, post-operative and follow-up geometries for Patient 1 and Patient 2. Specifically, it was decided to use a non uniform mesh characterised by a smaller cell diameter in the region of the inlet and the valve, where a higher accuracy was necessary since it is the region in which greater velocities and wall shear stresses will be expected.

Firstly, using the command *vmtksurfaceharmonicsolver*, the points of the geometry surface were assigned a value going from 0 at the inlet and 1 at the outlets by solving an equation

based on the Laplace-Beltrami operator on a given surface (in this case the pulmonary artery geometry). The solution of this process was collected in the array *phi* (Figure 3.8). Then, employing the command *polyfit* in Matlab, a second degree-polynomial, the function *edgelength*, was interpolated as a function of *phi* by defining some values chosen as the desired length of the cells throughout the geometry (Figure 3.8, centre in yellow). The function edgelength, indeed, was then used to define the length of the cells edges which is imposed when the surface mesh of the geometry is created.

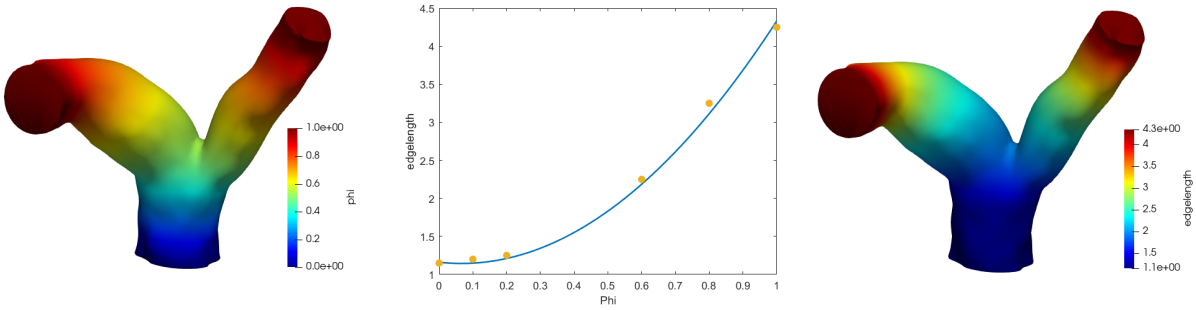

Figure 3.8: On the left the representation of the relation between *phi* and *edgelength* used both for Patient 1 and Patient 2 in pre-operative and post-operative/follow-up cases. On the right the function *edgelength* applied to Patient 1's geometry.

Finally, the using the VMTK command *vmtksurfaceremeshing* a triangular surface mesh was generated using the edgelength array as input. Then the surface mesh was converted into a volumetric tetrahedral mesh applying the command *vmtkmeshgenerator*. Ultimately, using the command *vmtkmeshwriter* the final meshed were obtained (Figure 3.9).

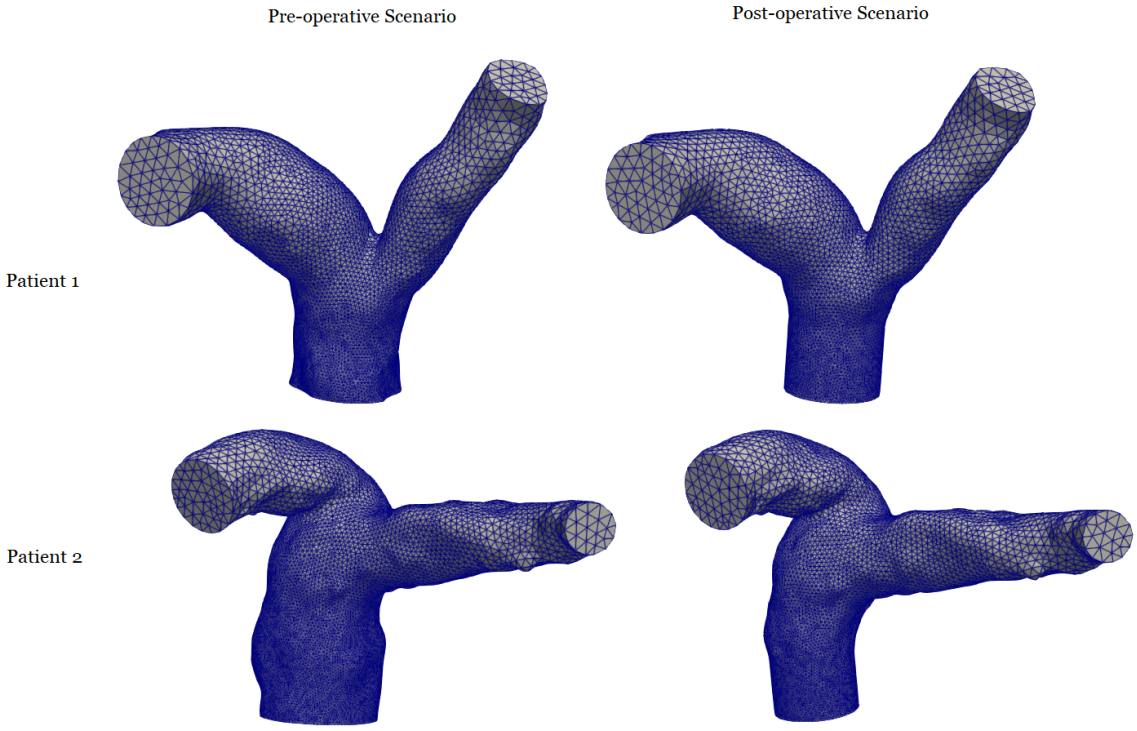

Figure 3.9: Meshes obatined both for the pre-operative and post-operative/follow-up geometries of Patient's 1 and Patient's 2 pulmonary arteries

The details concerning the meshes are summed in Table 3.1, for the pre-operative case, and Table 3.2, for the post-operative case.

Pre-operative	**Patient 1**	**Patient 2**
Number of active cells	300145	591223
Number of degrees of freedom	207744	400620
Maximum cell diameter	6.1 mm	6.0 mm
Average cell diameter	1.7 mm	1.6 mm
Minimum cell diameter	0.6 mm	0.6 mm

Table 3.1: Mesh characteristics for Patient 1 and Patient 2 pre-operative case.

Post-operative/Follow-up	Patient 1	Patient 2
Number of active cells	223969	307462
Number of degrees of freedom	156588	213512
Maximum cell diameter	5.9 mm	6.1 mm
Average cell diameter	1.8 mm	1.8 mm
Minimum cell diameter	0.7 mm	0.7 mm

Table 3.2: Mesh characteristics for Patient 1 and Patient 2 post-operative/follow-up case.

4 | Mathematical models and numerical methods

In this chapter, the mathematical models used to describe the pre-operative, post-operative and follow-up scenarios will be introduced.

Specifically, following the pipeline showed in Figure 4.1, in Section 4.1 the lumped parameters model of the whole cardiovascular system, used to apply suitable boundary conditions to the 3D models of the pulmonary arteries, will be described. Indeed, the lumped parameters model allows to generate three different pressure sets, one for each scenario, which will be then applied to the artificial boundaries. In particular, as already mentioned in Section 2.2, the pre-operative scenario is characterised by the absence of the valve, instead, in the post-operative and follow-up scenarios, we reproduced the fluid dynamics of the patients after pulmonary valve replacement and more specifically after 6 months and 9 years from the surgery, respectively.

Then, in Section 4.2 the fluid problem is described for the three cases; notice that different models are used to describe the pre-operative scenario and the post-operative/follow-up scenarios, in order to account for the absence or presence of the valve, respectively. Indeed, in the pre-operative scenario the absence of the valve, which implies also the absence of an interaction with the structure, leads to the adoption of a 3D Computational Fluid Dynamics model. Instead, in the case of the post-operative and follow-up scenarios, the presence of the valve implies the need for the use of a reduced Fluid-Structure Interaction model.

In Section 4.2.4, the reduced structural model, used to reproduce the valve dynamics, is introduced. As it will be explained more specifically in the next sections, the use of a 0D model for the valve modelling is linked to the reduced FSI approach adopted to describe the problem.

Finally, in Section 4.3, the numerical approximation of the models mentioned above will be described.

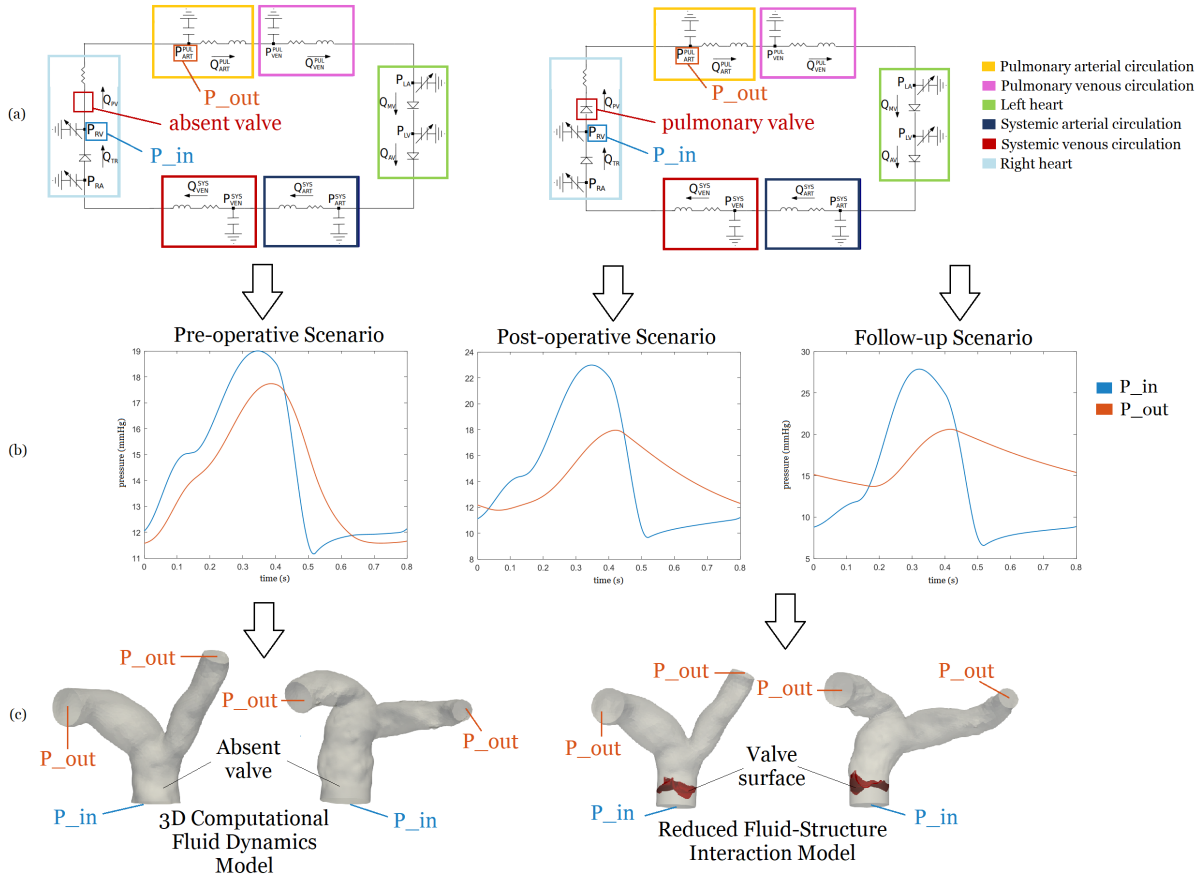

Figure 4.1: A brief pipeline explaining the use of the mathematical models in this thesis. A lumped parameters model of the whole circulation (a) is used to extract the pressure boundary conditions (b), these are then applied to the artificial boundaries of the 3D geometries related to the 3D CFD and reduced FSI models (c) used to model, respectively, the pre-operative and post-operative/follow-up scenarios.

4.1. Mathematical models: Lumped-parameters model of the whole cardiovascular system

The model of the circulatory system, which will be detailed in this section, describes both the systemic and pulmonary circulations in a simplified way with respect to the local fluid dynamics, however it can provide reliable measures of fluid dynamic quantities at a systemic level.

In this particular application, the lumped parameters model has been used in order to extract the pressure dynamics at the right ventricle and at the pulmonary artery level to be prescribed as input data to the 3D model. Indeed, the first point corresponds with the

inlet of the 3D geometry considered to carry out the study of haemodynamics and the second location corresponds to the two outlets of the same geometry.

Specifically we can distinguish two lumped parameters models used to reproduce the scenarios previously mentioned:

- Pre-0D model: used for the pre-operative scenario, its aim is to reproduce the haemodynamics of the whole circulation when the pulmonary valve is absent, this will be carried out by modifying the resistances modelling the valve dynamics;
- Valve-0D model: in this case, the model aims at reproducing the haemodynamics after pulmonary valve replacement so the resistances related to the pulmonary valve dynamics are changed accordingly; this model will be used both for the post-operative and follow-up scenarios. Notice, however, that these two scenarios will be further differentiated by the calibrated parameters for the rest of the compartments.

The cardiovascular system is divided into compartments; loosing the space dependence, these compartments are described using only time-dependent variables through a set of ordinary differential equations and are often represented by an electrical network. The model used for this thesis was previously described in [73]; the circulation is divided in pulmonary arterial and venous circulation, systemic arterial and venous circulation, which are resistance-inductance-capacitance (RLC) networks, right heart and left heart, which are described by time-varying elastance elements while the valves are modelled by non-ideal diodes (Figure 4.2).

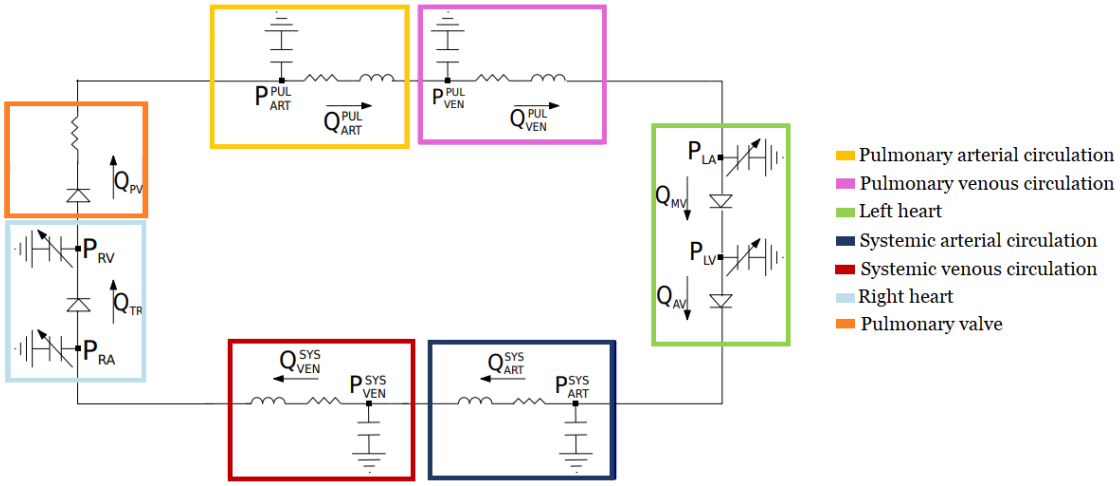

Figure 4.2: A schematic representation of the lumped parameters model.

In order to describe the mathematical model of the whole circulation, the following nota-

tion is introduced:

- The flow rate is referred to as Q, the pressure as P and the volume as V.
- The left and right atrium are represented by the abbreviations, respectively, LA and RA.
- The left and right ventricle are represented by the abbreviations, respectively, LV and RV.
- The mitral, aortic, tricuspid and pulmonary valve are identified by the abbreviations, respectively, MV, AV, TV and PV.
- The pulmonary and system arterial and venous systems are identified respectively by the combinations AR-PUL, AR-SYS, VEN-PUL, VEN-SYS.

The mathematical model is defined by the following equations:

- For the pulmonary arterial circulation:

$$\begin{aligned} C_{AR}^{PUL}\ \frac{dP_{AR}^{PUL}(t)}{dt} &= Q_{PV}(t) - Q_{AR}^{PUL}(t), \\ L_{AR}^{PUL}\ \frac{dQ_{AR}^{PUL}(t)}{dt} &= -R_{AR}^{PUL}Q_{AR}^{PUL}(t) - P_{VEN}^{PUL}(t) + P_{AR}^{PUL}(t). \end{aligned}$$

- For the pulmonary venous circulation:

$$\begin{aligned} C_{VEN}^{PUL}\ \frac{dP_{VEN}^{PUL}(t)}{dt} &= Q_{AR}^{PUL}(t) - Q_{VEN}^{PUL}(t), \\ L_{VEN}^{PUL}\ \frac{dQ_{VEN}^{PUL}(t)}{dt} &= -R_{VEN}^{PUL}Q_{VEN}^{PUL}(t) - P_{LA}(t) + P_{VEN}^{PUL}(t). \end{aligned}$$

- For the systemic arterial circulation:

$$\begin{aligned} C_{AR}^{SYS}\ \frac{dP_{AR}^{SYS}(t)}{dt} &= Q_{AV}(t) - Q_{AR}^{SYS}(t), \\ L_{AR}^{SYS}\ \frac{dQ_{AR}^{SYS}(t)}{dt} &= -R_{AR}^{SYS}Q_{AR}^{SYS}(t) - P_{VEN}^{SYS}(t) + P_{AR}^{SYS}(t). \end{aligned}$$

- For the systemic venous circulation:

$$\begin{aligned} C_{VEN}^{SYS}\ \frac{dP_{VEN}^{SYS}(t)}{dt} &= Q_{AR}^{S}YS(t) - Q_{VEN}^{SYS}(t), \\ L_{VEN}^{SYS}\ \frac{dQ_{VEN}^{SYS}(t)}{dt} &= -R_{VEN}^{SYS}Q_{VEN}^{SYS}(t) - P_{RA}(t) + P_{VEN}^{SYS}(t). \end{aligned}$$

- For the right heart:

$$\begin{aligned}
P_{RA}(t) &= P_{EX}(t) + E_{RA}(t)(V_{RA}(t) - V_{0,RA}),\\
P_{RV}(t) &= P_{EX}(t) + E_{RV}(t)(V_{RV}(t) - V_{0,RV}),\\
\frac{V_{RA}(t)}{dt} &= Q_{VEN}^{SYS}(t) - Q_{TV}(t),\\
\frac{V_{RV}(t)}{dt} &= Q_{TV}(t) - Q_{PV}(t),\\
L_{TV}\frac{dQ_{TV}(t)}{dt} &= P_{RA}(t) - \Delta P_{TV}(Q_{TV}(t)) - P_{RV}(t),\\
L_{PV}\frac{dQ_{PV}(t)}{dt} &= P_{RV}(t) - \Delta P_{PV}(Q_{PV}(t)) - P_{AR}^{PUL}(t).
\end{aligned}$$

- For the left heart:

$$\begin{aligned}
P_{LA}(t) &= P_{EX}(t) + E_{LA}(t)(V_{LA}(t) - V_{0,LA}),\\
P_{LV}(t) &= P_{EX}(t) + E_{LV}(t)(V_{LV}(t) - V_{0,LV}),\\
\frac{V_{LA}(t)}{dt} &= Q_{VEN}^{PUL}(t) - Q_{MV}(t),\\
\frac{V_{LV}(t)}{dt} &= Q_{MV}(t) - Q_{AV}(t),\\
L_{MV}\frac{dQ_{MV}(t)}{dt} &= P_{LA}(t) - \Delta P_{MV}(Q_{MV}(t)) - P_{LV}(t),\\
L_{AV}\frac{dQ_{AV}(t)}{dt} &= P_{LV}(t) - \Delta P_{AV}(Q_{AV}(t)) - P_{AR}^{SYS}(t).
\end{aligned}$$

The equations describing the model can be summed up in the following compact form:

$$\begin{cases}
\dfrac{d}{dt}\boldsymbol{y}(t) = f_1(t, \boldsymbol{y}(t), \boldsymbol{z}(t))\\
\boldsymbol{z}(t) = f_2(t, \boldsymbol{y}(t))\\
\boldsymbol{y}(0) = y_0
\end{cases} \tag{4.1}$$

where

$$\boldsymbol{y} = (V_{LA}(t), V_{LV}(t), V_{RA}(t), V_{RV}(t), P_{AR}^{SYS}(t), P_{AR}^{PUL}(t), P_{VEN}^{SYS}(t), P_{VEN}^{PUL}(t))^T$$

and

$$\boldsymbol{z} = (P_{LV}(t), P_{LA}(t), P_{RV}(t), P_{RA}(t), Q_{MV}(t), Q_{AV}(t), Q_{TV}(t), Q_{PV}(t))^T.$$

Focusing on the pulmonary valve, the model chosen for this component of the circulation

is a non ideal diode, which can be also interpreted as a diode with a resistance in series as in Figure 4.2. The analytical expression of the overall valve resistance, is $R = 10^c$ where c is defined as:

$$c = \log_{10} R_{min} \; + \; (\log_{10} R_{max} - \log_{10} R_{min}) \cdot \left[\frac{1}{2} + \frac{1}{\pi} \arctan\left(\frac{k\pi}{2}(P_2 - P_1) \right) \right],$$

R_{max} is the resistance when the valve is closed and R_{min} is the resistance when the valve is open.

In the Pre-0D model, the absence of the valve was modelled by imposing $R_{max} \simeq R_{min}$; indeed this implies that the resistance when the valve is closed is approximately the resistance when the valve is open, so the model simulates a situation in which the valve is virtually always open, i.e. is absent. Whereas, in the Valve-0D model, the condition applied is $R_{max} \gg R_{min}$, so in this case the valve model actually simulates the behaviour of a healthy valve. Moreover, the lumped parameters model was further tuned in order to differentiate the post-operative scenario from the follow-up scenario, by trying to adhere as much as possible to specific values of the patients' available clinical data. The values used in the model calibration will be better detailed in Section 5.1.

Finally, it has to be noted that we have adopted the *One-Way* approach, this means that the lumped parameters model of the circulation does not receive a feedback from the three-dimensional model but it is solved independently.

4.2. Mathematical models: Pre-operative, post-operative scenario and follow-up scenarios

The aim of this section is to describe the modelling choices made for the fluid problem, in the pre-operative, post-operative and follow-up scenarios.

First, the modelling of the blood will be presented and afterwards two fluid models will be discussed. The first represents the pre-operative scenario and it is a model which does not include the interaction between the blood and the valve leaflets, since the patients were characterised by the absence of the valve before the pulmonary valve replacement. The second fluid model, instead, describes both the post-operative and the follow-up scenario; indeed, in both cases the presence of the valve must be considered, and so the fluid-structure interaction between the blood and the stented valve leaflets is modeled.

Moreover, in both models, the compliance of the wall is disregarded; indeed, the pulmonary artery is characterised by a lower pressure and its wall undergoes smaller de-

formations than vessels like the aorta, which, being characterised by higher pressures, undergoes large deformations. This assumption has been proven to lead to a slight overestimation of wall-related haemodynamics quantities like wall shear stress, however the flow distribution patterns have demonstrated to be comparable with the cases in which wall compliance is included in the model [17].

4.2.1. Blood modelling

Blood is constituted by a suspension of cells in an aqueous substance called *plasma* which represents, in average, the 55% of the total volume of blood and it is composed by 93% of water. The cells contained in blood are *erythrocytes* or *red blood cells*, *leukocytes* or *white blood cells* and *platelets*; the percentage of volume occupied by the cells is called *hematocrit (Ht)* and it is, in average, the 45% of the blood volume.

When the dimension of the cells suspended in blood is significantly smaller than the vessel dimension, blood can be modelled as a homogeneous Newtonian fluid with density ρ and viscosity μ. This is the case of the pulmonary artery because the cells contained in blood have a diameter in the order of 10 μm while the artery has a diameter in the order of mm [29].

Specifically, the density of blood takes into account the coexistence of a corpuscular and aqueous part, so it is found using the relation:

$$\rho = (1 - Ht)\rho_p + Ht\rho_c$$

where ρ_p is the volumic mass of the plasma while ρ_c is the volumic mass of the cellular component of blood. Being the hematocrit 45% in average, the density of blood is $\rho = 1.06 \cdot 10^3\, kg/m^3$. Moreover, considering blood as a Newtonian fluid means that it is characterised by a linear relation between the shear stress and the velocity gradient (shear rate), the proportionality coefficient of this relationship is the dynamic viscosity that for blood is $\mu = 3.5{\cdot}10^{-3}\, Pa{\cdot}s$ [29]. Finally, the blood is commonly modelled as incompressible if haemodynamics in the arteries are considered [13].

4.2.2. Pre-operative scenario: Computational Fluid Dynamics model

As already mentioned, in the pre-operative scenario there is not modelling of fluid-structure interaction, both because of the valve absence and because the wall compliance is disregarded. Due to these considerations, for the pre-operative scenario, a computa-

tional fluid dynamics (CFD) model based on Navier-Stokes equations for a homogeneous, incompressible and Newtonian fluid in a fixed domain has been adopted.

Therefore, a domain $\Omega_{pre} \in \mathbb{R}^3$ (Figure 4.3), which represents the pulmonary artery before the pulmonary valve replacement, is considered. The boundary of the domain Ω_{pre} consists in Γ_{in} representing the inlet, Γ_{outj} with $j = 1, 2$ representing the two outlets and Γ_{wall} which is the wall of the blood vessel.

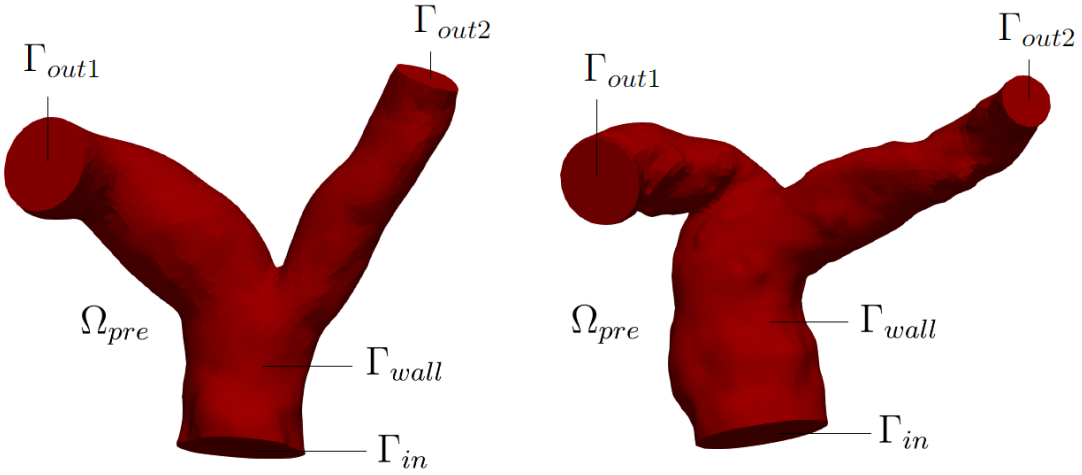

Figure 4.3: Patient's 1 (left) and Patient's 2 (right) computational domain in the pre-operative scenario.

The velocity $\mathbf{u}(t, \mathbf{x}) : \mathbb{R}^+ \times \Omega_{pre} \to \mathbb{R}^3$ and the pressure $p(t, \mathbf{x}) : \mathbb{R}^+ \times \Omega_{pre} \to \mathbb{R}$ satisfy the following formulation of Navier-Stokes equation for each $t \in (0, T)$:

$$\begin{cases} \rho \dfrac{\partial \mathbf{u}}{\partial t} + \rho(\mathbf{u} \cdot \nabla)\mathbf{u} + \nabla p - \mu \nabla \cdot (\nabla \mathbf{u} + \nabla \mathbf{u}^T) = 0 & in\ \Omega_{pre}, \\ \nabla \cdot \mathbf{u} = \mathbf{0} & in\ \Omega_{pre}, \\ \mathbf{u}(t, \mathbf{x}) = 0 & on\ \Gamma_{wall}, \\ \boldsymbol{\sigma}(\mathbf{u}, p)\mathbf{n} = p_{in}\mathbf{n} & on\ \Gamma_{in}, \\ \boldsymbol{\sigma}(\mathbf{u}, p)\mathbf{n} = p_{outj}\mathbf{n} & on\ \Gamma_{out_j},\ j = 1, 2 \\ \mathbf{u}(0, \mathbf{x}) = 0 & in\ \Omega_{pre} \end{cases} \tag{4.2}$$

The first equation of the system (4.2) represents the conservation of the momentum, in which the first term explicits the time-dependency of the problem. The density ρ and viscosity μ of the blood are considered constant. Moreover, the forcing term is null since, in the artery haemodynamics, the effects of gravity can be disregarded.

The conservation of mass, in the second equation, expresses the incompressibility of the fluid while the third equation is used to impose a no-slip condition at the wall of the artery.

The boundary conditions described by the fourth and fifth equation, allow to solve the system; in particular, through these equations a prescribed pressure is applied both to the inlet and the two outlets. The pressures p_{in} and p_{out} are obtained by means of the lumped parameters model of the circulation described in Section 4.1. Notice that, as previously mentioned, the pressure sets used as boundary condition are different depending on the scenario considered; this differentiation is carried out to reproduce the different conditions of the patients' in the three scenarios.

Since blood is modelled as an incompressible, homogeneous Newtonian fluid; the Cauchy stress tensor $\sigma(\mathbf{u}, p)$ for a fluid with these characteristics is:

$$\boldsymbol{\sigma}(\mathbf{u}, p) = -p\mathbf{I} + 2\mu\mathbf{D}(\mathbf{u}) = -p\mathbf{I} + \mu(\nabla\mathbf{u} + (\nabla\mathbf{u})^T) \tag{4.3}$$

where $\mathbf{D}(\mathbf{u})$ is the strain rate tensor while p and $\boldsymbol{u}$ are, respectively, the pressure and the velocity of the fluid.

Finally, the sixth equation is the initial condition, which imposes null velocity in the first instant of the simulation; thus, at the beginning of the simulation the blood velocity is zero.

4.2.3. Post-operative/follow-up scenarios: Fluid model and Resistive Immersed Implicit Surface method

In the post-operative and follow-up scenarios the presence of the valve is taken into account. For this reason, we employed a reduced Fluid-Structure Interaction (FSI) model in which the effects of the valve presence are accounted for by using the Resistive Immersed Implicit Surface (RIIS) method while, as already explained, the compliance of the wall is neglected.

This method consists in introducing an additional penalty term in the equation describing the conservation of the momentum, in this way it is weakly imposed the kinematic condition linked to the valve presence, i.e. the adherence of blood to the moving leaflets. This approach was already described in [35] and in [60] as it was applied, respectively, in the study of the mitral and pulmonary valve. Notice that the term *reduced* refers to the geometrical reduction of the structural model; indeed, for the structural model of the

valve, the use of a reduced 0D model is chosen, as it is better detailed in Sections 4.2.4 and 4.2.5.

The problem in the two scenarios will be characterised by a domain Ω_{pvr} (Figure 4.4) derived from the patients' geometries after the pulmonary valve replacement. The boundary of the domain is still divided in Γ_{in} representing the inlet, Γ_{outj} with $j = 1, 2$ representing the two outlets and Γ_{wall} which is the wall of the blood vessel. However, in this case the valve is present and its geometry is represented as a surface Γ_t immersed in the fluid domain Ω_{pvr}. The valve surface Γ_t is described at each time t by a level-set function $\varphi_t : \Omega_{pvr} \to \mathbb{R}$, such that:

$$\Gamma_t = \{\mathbf{x} \in \Omega_{pvr} : \varphi_t(\mathbf{x}) = 0\}.$$

The function φ_t is a signed distance function, such function is chosen to fulfill the condition: $|\nabla \varphi_t| = 1$, for any t.

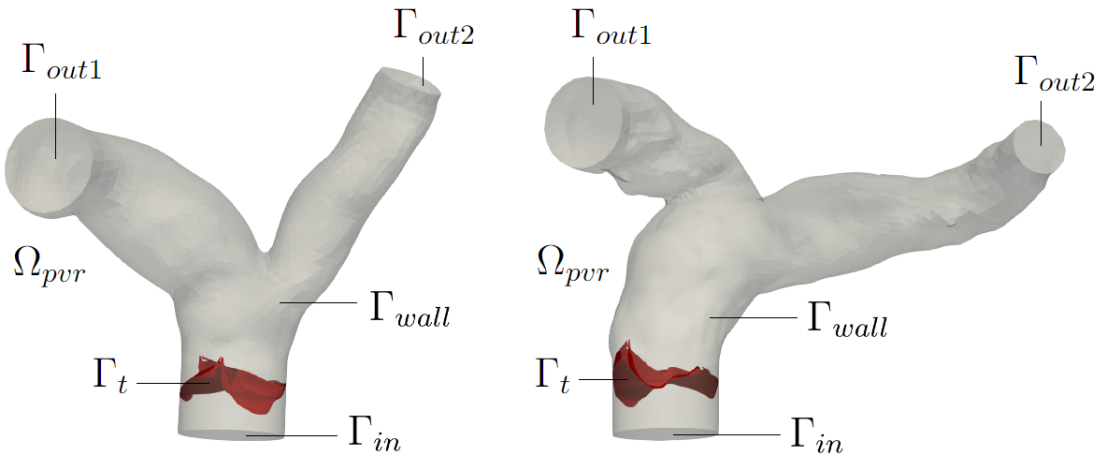

Figure 4.4: Patient's 1 (left) and Patient's 2 (right) computational domain in the post-operative scenario.

Accordingly, the velocity $\mathbf{u}(t, \mathbf{x}) : \mathbb{R}^+ \times \Omega_{pvr} \to \mathbb{R}^3$ and the pressure $p(t, \mathbf{x})) : \mathbb{R}^+ \times \Omega_{pvr} \to \mathbb{R}$ satisfy the following formulation of Navier-Stokes equation for each $t \in (0, T)$:

$$\begin{cases} \rho\dfrac{\partial \mathbf{u}}{\partial t} + \rho(\mathbf{u}\cdot\nabla)\mathbf{u} + \nabla p - \mu\nabla\cdot(\nabla\mathbf{u} + \nabla\mathbf{u}^T) \\ \quad +\frac{R}{\varepsilon}(\mathbf{u}-\mathbf{u}_\Gamma)\delta_{t,\varepsilon} = \mathbf{0} & in\ \Omega_{pvr}, \\ \nabla\cdot\mathbf{u} = 0 & in\ \Omega_{pvr}, \\ \mathbf{u}(t,\mathbf{x})) = 0 & on\ \Gamma_{wall}, \\ \boldsymbol{\sigma}(\mathbf{u},p)\mathbf{n} = p_{in}\mathbf{n} & on\ \Gamma_{in}, \\ \boldsymbol{\sigma}(\mathbf{u},p)\mathbf{n} = p_{outj}\mathbf{n} & on\ \Gamma_{out_j},\ j=1,2 \\ \mathbf{u}(0,\mathbf{x})) = 0 & in\ \Omega_{pvr} \end{cases} \tag{4.4}$$

The first equation still represents the conservation of the momentum, however, if compared to the conservation of momentum featured in the pre-operative model, it can be noticed that the term $\frac{R}{\varepsilon}(\mathbf{u}-\mathbf{u}_\Gamma)\delta_{t,\varepsilon}$ has been added. This is the resistive penalty term and includes a multiplicative factor given by the ratio between the resistance coefficient R and the half-thickness of the leaflets ε. This ratio is consistent with the condition that the terms aims to enforce; which is $\mathbf{u} = \mathbf{u}_\Gamma$ as $\varepsilon \to 0$ meaning that as the fluid touches the leaflets its velocity $\boldsymbol{u}_\Gamma$ corresponds to the leaflets velocity $\boldsymbol{u}$. Indeed, when $\varepsilon \to 0$ the ratio $\frac{R}{\varepsilon} \to \infty$, which weakly enforces the condition $\boldsymbol{u} = \boldsymbol{u}_\Gamma$.

The resistive penalty term has support in a narrow layer around the surface Γ_t which is represented by a smeared Dirac delta function $\delta_{t,\varepsilon} : \Omega_{pvr} \to [0, +\infty)$, this function approximates the Dirac distribution as follows:

$$\delta_{t,\varepsilon}(\mathbf{x}) = \begin{cases} \dfrac{1+\cos(\pi\varphi_t(\mathbf{x})/\varepsilon)}{2\varepsilon} & \text{if } |\varphi_t(\mathbf{x})| \le \varepsilon, \\ 0 & \text{if } |\varphi_t(\mathbf{x})| > \varepsilon \end{cases} \tag{4.5}$$

Notice that both the velocity of the leaflets $\boldsymbol{u}_\Gamma$ and the function $\varphi_{t,\epsilon}$, describing the configuration of the leaflets, and so $\delta_{t,\varepsilon}$, are unknowns of the problem, which will be obtained using a reduced structural model of the valve, as better detailed in Section 4.2.4.

As for the rest of the equations, the considerations made for the pre-operative scenario are valid also in this case. However, the boundary conditions p_{in} and p_{out} applied, respectively, at the inlet and at the two outlets will be different according to the different scenario considered, as previously explained. The modelling of blood does not change with respect to the pre-operative model, so the Cauchy stress tensor $\sigma(\mathbf{u}, p)$ is still described by the same expression (4.3).

As for the initial condition, the initial velocity of the fluid is set null so, accordingly ,the

simulations will be set such that in the initial instant the heart cycle will be in diastolic phase and the pulmonary valve will be closed.

4.2.4. Post-operative/follow-up scenarios: Reduced mechanical model of the pulmonary valve

As already mentioned, a structural model for the deformation of the surface Γ_t is required in order to provide the configuration of the valve, represented by $\varphi_{t,\varepsilon}$, and its velocity, represented by $\mathbf{u}_\Gamma$, in the fluid problem. The model chosen to do this was proposed in [34] and it consists in a reduced structural model which aims at realistically describing the main characteristics of cardiac valve dynamics.

Let $\mathbf{d}_\Gamma : [0,T] \times \widehat{\Gamma} \to \mathbb{R}^3$ denote the displacement of the leaflet with respect to its reference configuration $\Gamma_0 = \widehat{\Gamma}$ (Figure 4.5, left), so we can represent the current configuration of the leaflet surface as:

$$\Gamma_t = \{\mathbf{x} \in \mathbb{R}^3 \ : \ \mathbf{x} = \mathbf{T}_t(\widehat{\mathbf{x}}) = \widehat{\mathbf{x}} + \mathbf{d}_\Gamma(t, \widehat{\mathbf{x}})\}.$$

We assume that, at each time t, every point $\mathbf{x} \in \Gamma_t$ of the leaflet is subject to an external force $\mathbf{f}(t, \mathbf{x})$ determined by the effects of the surrounding fluid and to an elastic force associated to the leaflet curvature $H(\mathbf{x})$ (Figure 4.5, right), moreover the leaflets motion can be affected by some damping effect. Furthermore, we hypothesise that the curvature-induced elastic force acts only in normal direction with respect to the surface, in a similar way as surface tension. Finally, since commonly the resting state of the valve is considered to be the closed configuration, the elastic force is imposed to vanish on $\widehat{\Gamma}$.

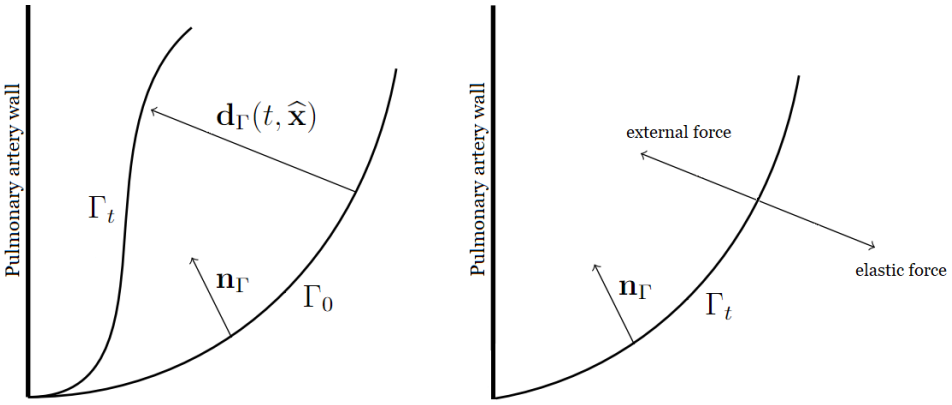

Figure 4.5: A schematic representation of the leaflets displacement $\boldsymbol{d}_\Gamma$ (left) and the forces acting on the leaflets (right).

According to the assumptions made, the local force balance is characterised by the following formulation:

$$\rho_\Gamma \ddot{\mathbf{x}} + \beta\rho_\Gamma \dot{\mathbf{x}} = \mathbf{f}(t,\mathbf{x}) - \gamma[H(\mathbf{x}) - \widehat{H}(\widehat{\mathbf{x}})]\mathbf{n}_\Gamma(\mathbf{x}) \tag{4.6}$$

where ρ_Γ is the surface density of the valve, β is a damping coefficient, γ is a stiffness coefficient and $\mathbf{n}_\Gamma$ is the normal to the surface Γ_t. The function $\widehat{H}(\widehat{\mathbf{x}})$ represents the total curvature of the surface $\widehat{\Gamma}$ in the position $\widehat{\mathbf{x}} = \mathbf{T}_t^{-1}(\mathbf{x})$

To simplify the model and according to common practice on biological tissues, the valve leaflet density is considered the same as blood. Therefore, $\rho_\Gamma = 2\varepsilon\rho$ where ε is the semi-thickness of the leaflet. Following RIIS representation, the consistency formula

$$\int_{\Gamma_t} \rho_\Gamma \, d\Gamma \simeq \int_{\Omega_{pvr}} 2\varepsilon\rho\delta_{t,\varepsilon} \, d\Omega = \rho 2\varepsilon|\Gamma_t|$$

is obtained.

The parameter ρ_Γ can be tuned to different values with the aim of accounting for different inertial properties of the leaflets without loss of generality, this can be useful, for example, in the case of patient-specific setting in which the inertial properties of the valve may be unknown.

Now that the mechanical model for the valve has been defined, it is necessary to perform some few steps more in order to reduce Equation (4.6) to a 0D model. Thus, we assume that $\mathbf{d}_\Gamma$ can be decomposed as:

$$\mathbf{d}_\Gamma(t,\widehat{\mathbf{x}}) = c(t)\mathbf{g}(\widehat{\mathbf{x}}), \tag{4.7}$$

where $\mathbf{g} : \widehat{\Gamma} \to \mathbb{R}^3$ is known and $c : [0,T] \to \mathbb{R}$ has to be modelled.

Specifically, the function $\boldsymbol{g}$ is known and describes the valve opening field (reconstructed in Section 3.4), so it characterises the displacement of the valve between the closed and open configurations. On the other hand, c is an unknown of the problem and it represents the opening coefficient of the valve, so it indicates the fraction of the valve opening; thus, in the model adopted, c is defined as $c : [0,T] \to [0,1]$, with $c = 0$ corresponding to the closed position and $c = 1$ to the open position.

Taking into account all these considerations, the force balance in (4.6) can be re-written as:

$$[\ddot{c}(t) + \beta\dot{c}(t)]\rho_\Gamma \mathbf{g}(\mathbf{T}_t^{-1}(\mathbf{x})) = \mathbf{f}(t,\mathbf{x}) - \gamma[H(\mathbf{x}) - \widehat{H}(\widehat{\mathbf{x}})]\mathbf{n}_\Gamma(\mathbf{x}). \tag{4.8}$$

Integrating over Γ_t the component along $\mathbf{n}_\Gamma(\mathbf{x})$ of forces in (4.8), the following ordinary differential equation in c is obtained:

$$\ddot{c} + \beta\dot{c} = \frac{\int_{\Gamma_t} \mathbf{f}(t,\mathbf{x}) \cdot \mathbf{n}_\Gamma(\mathbf{x})\, d\mathbf{x} - \gamma \int_{\Gamma_t} [H(\mathbf{x}) - \widehat{H}(\widehat{\mathbf{x}})]\, d\mathbf{x}}{\int_{\Gamma_t} \rho_\Gamma \mathbf{g}(\mathbf{T}_t^{-1}(\mathbf{x})) \cdot \mathbf{n}_\Gamma(\mathbf{x})\, d\mathbf{x}}. \tag{4.9}$$

This equation can be completed with suitable initial conditions on $c(0)$ and $\dot{c}(0)$ depending on the applications. In the current configuration, the valve is initially closed so the initial conditions will be: $c(0) = 0$ and $\dot{c}(0) = 0$.

4.2.5. Post-operative/follow-up scenarios: Coupling of fluid and structure models

The 3D fluid model described in Section 4.2.3 and the lumped parameter structure model presented in Section 4.2.4 can be coupled in a *reduced FSI model*. To do this, the fluid-to-valve stress distribution $\mathbf{f}$ in Equation (4.8) needs to be provided in terms of $\mathbf{u}$, p and RIIS-related quantities; moreover, the RIIS signed distance φ_t, in (4.5), and the leaflets velocity $\mathbf{u}_\Gamma$ in (4.4) have to be reinterpreted as functions of c and $\boldsymbol{g}$.

Therefore, some additional notation, linked to the representation of the immersed surface Γ_t is introduced. Being φ_t a signed distance function, the domain Ω_{pvr} can be divided in two regions:

$$\Omega_t^+ = \{\mathbf{x} \in \Omega_{pvr} \ : \ \varphi_t \geq 0\}, \quad \Omega_t^- = \{\mathbf{x} \in \Omega_{pvr} \ : \ \varphi_t \leq 0\};$$

the intersection of these two regions is Γ_t (Figure 4.6).

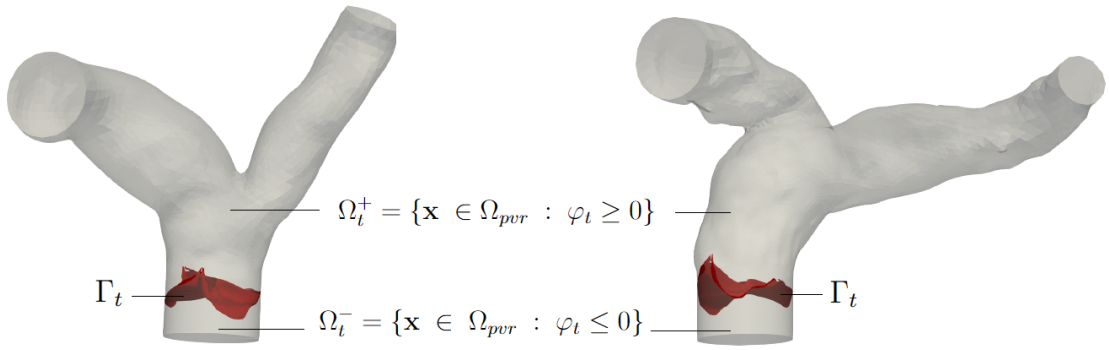

Figure 4.6: A schematic representation of the domain division in Patient's 1 and Patient's 2 geometries

Accordingly, any function f defined over Ω_{pvr} can be decomposed so that $f = f^+ + f^-$, where $f^\pm = f|_{\Omega^\pm}$. Moreover, the function φ_t allows to define $\tilde{\mathbf{n}}_\Gamma$ and $\tilde{H}$: the extension on the whole domain Ω_{pvr} of the surface normal $\mathbf{n}_\Gamma$ and its curvature H. These extensions are defined as follows:

$$\tilde{\mathbf{n}}_\Gamma = \frac{\nabla\varphi_t}{|\nabla\varphi_t|}, \quad \tilde{H} = -\mathrm{div}\,\tilde{\mathbf{n}}_\Gamma = -\frac{\Delta\varphi_t}{|\nabla\varphi_t|} + \frac{\nabla^2\varphi_t - \nabla\varphi_t \otimes \nabla\varphi_t}{|\nabla\varphi_t|^3}. \tag{4.10}$$

These quantities are the actual extensions of the normal vector and curvature as $\tilde{\mathbf{n}}_\Gamma|_\Gamma = \mathbf{n}_\Gamma$ and $\tilde{H}|_\Gamma = H$. Moreover, notice that $\tilde{\mathbf{n}}_\Gamma$ is defined in a way that it does not change its verse when passing through Γ_t. Finally, it is important to point out that, in the definitions (4.10), the assumption that $|\nabla\varphi_t| \equiv 1$ was not made. Although such assumption holds true in the neighborhood of the internal points of Γ_t, its validity is broken near $\partial\Gamma_t$, where φ_t is not continuous. In addition, this definition of $\tilde{\mathbf{n}}_\Gamma$ ensures that the normal has unit magnitude also at the discrete level.

Moving on to function $\mathbf{g}$, which is defined only on $\widehat{\Gamma}$, its extension to any location $\mathbf{y} \in \Omega_{pvr}$ can be defined using the value assumed by $\mathbf{g}$ at the projection $\widehat{\mathbf{y}} \in \widehat{\Gamma}$ of $\mathbf{y}$ onto $\widehat{\Gamma}$. A similar extension can be defined for $\widehat{H}$.

The quantities defined until now describe the geometry of the valve leaflets, from now on its kinematics and dynamics will be presented.

As for the kinematic description of the surface represented in the RIIS approach, a definition of the surface velocity $\mathbf{u}_\Gamma$ is required. Exploiting the level-set properties of the function φ_t, the leaflets velocity can be defined as:

$$\mathbf{u}_\Gamma = -\partial_t\varphi_t \, \frac{\nabla\varphi_t}{|\nabla\varphi_t|}.$$

However, given the definition (4.7), a more concrete definition of the leaflets velocity is:

$$\mathbf{u}_\Gamma(t, \mathbf{x}) = \dot{c}(t)\tilde{\boldsymbol{g}}(\mathbf{x}), \tag{4.11}$$

where $\tilde{\boldsymbol{g}}(\mathbf{x}) : \Omega_{pvr} \to \mathbb{R}^3$ is the closest-point extension of $g : \widehat{\Gamma} \to \mathbb{R}^3$; from now on this expression will be used.

For what concerns the dynamics, we refer to Equation (4.9). The forces $\mathbf{f}$ exerted by the fluid on the valve are related to the stress jump across the surface Γ_t, therefore the

following equality holds true:

$$\mathbf{f} = [\boldsymbol{\sigma}\mathbf{n}_\Gamma]|_{\Gamma_t} = \boldsymbol{\sigma}^+|_{\Gamma_t}\mathbf{n}_\Gamma - \boldsymbol{\sigma}^-|_{\Gamma_t}\mathbf{n}_\Gamma.$$

Moreover, considering the surface smearing introduced by the smooth Dirac delta $\delta_{\Gamma,\varepsilon}$ and the definitions (4.10), the integral term related to $\mathbf{f}$ in Equation (4.9) can be approximated as follows:

$$\int_{\Gamma_t} \mathbf{f}\cdot\mathbf{n}_\Gamma \simeq \int_{\Omega_{pvr}} (\boldsymbol{\sigma}\tilde{\mathbf{n}}_\Gamma\cdot\tilde{\mathbf{n}}_\Gamma\delta^+_{\Gamma,\varepsilon} - \boldsymbol{\sigma}\tilde{\mathbf{n}}_\Gamma\cdot\tilde{\mathbf{n}}_\Gamma\delta^-_{\Gamma,\varepsilon}). \tag{4.12}$$

The other integral terms in Equation (4.9) can be approximated analogously:

$$\begin{aligned} \int_{\Gamma_t} \rho_\Gamma(\mathbf{g}\circ\mathbf{T}_t^{-1})\cdot\mathbf{n}_\Gamma &\simeq \int_{\Omega_{pvr}} \rho_\Gamma(\mathbf{g}\circ\mathbf{T}_t^{-1})\cdot\mathbf{n}_\Gamma\,\delta_{\Gamma,\varepsilon}, \\ -\gamma\int_{\Gamma_t}(H-\widehat{H}\circ\mathbf{T}_t^{-1}) &\simeq -\gamma\int_{\Omega_{pvr}}(\tilde{H}-\widehat{\tilde{H}})\,\delta_{\Gamma,\varepsilon}, \end{aligned} \tag{4.13}$$

where $\widehat{\tilde{H}}$ denotes the RIIS representation of the pulled-back curvature $\widehat{H}\circ\mathbf{T}_t^-1$.

It can be noted that, since $|\tilde{\mathbf{n}}| \equiv 1$, if the strain component of the normal stress is assumed to be negligible with respect to the pressure term, the integral force in (4.12) can be expressed as:

$$\int_{\Gamma_t} \mathbf{f}\cdot\mathbf{n}_\Gamma \simeq \int_{\Omega_{pvr}} (p\,\delta^+_{\Gamma,\varepsilon} - p\,\delta^-_{\Gamma,\varepsilon}).$$

This assumption is in accordance with other models based on the pressure jump across the valve [34, 49].

All in all, the coupled reduced FSI problem can be summed up as follows:

Given p_{in}, p_{out}, $\mathbf{g}$, $\tilde{\mathbf{g}}$; find, for each $t \in (0, T]$ $\mathbf{u}$, p, c such that:

$$
\begin{aligned}
&\text{fluid problem} \begin{cases}
\rho\dfrac{\partial \mathbf{u}}{\partial t} + \rho(\mathbf{u}\cdot\nabla)\mathbf{u} + \nabla p - \mu\nabla\cdot(\nabla\mathbf{u} + \nabla\mathbf{u}^T) & \\
\quad + \frac{R}{\varepsilon}(\mathbf{u} - \mathbf{u}_\Gamma)\delta_{t,\varepsilon} = 0 & in\ \Omega_{pvr}, \\
\nabla\cdot\mathbf{u} = 0 & in\ \Omega_{pvr}, \\
\mathbf{u}(t,\mathbf{x})) = 0 & on\ \Gamma_{wall}, \\
\boldsymbol{\sigma}(\mathbf{u},p)\mathbf{n} = p_{in}\mathbf{n} & on\ \Gamma_{in}, \\
\boldsymbol{\sigma}(\mathbf{u},p)\mathbf{n} = p_{out_j}\mathbf{n} & on\ \Gamma_{out_j}\ ,\ j = 1,2\ , \\
\mathbf{u}(0,\mathbf{x})) = 0 & in\ \Omega_{pvr}
\end{cases} \\
&\text{structure problem} \begin{cases}
[\ddot{c}(t) + \beta\dot{c}(t)]\rho_\Gamma\mathbf{g}(\mathbf{T}_t^{-1}(\mathbf{x})) = \mathbf{f}(t,\mathbf{x}) - \gamma[H(\mathbf{x}) - \widehat{H}(\widehat{\mathbf{x}})]\mathbf{n}_\Gamma(\mathbf{x}), \\
c(0) = 0, \quad \dot{c}(0) = 0,
\end{cases} \\
&\text{coupling} \begin{cases}
\Gamma_t = \widehat{\mathbf{x}} + c\,\mathbf{g}, \quad \delta_{\Gamma,\varepsilon} = F(\Gamma_t), \\
\mathbf{u}_\Gamma = \dot{c}\,\tilde{\mathbf{g}}, \\
\mathbf{f} = [\boldsymbol{\sigma}(\boldsymbol{u},p)\boldsymbol{n}_\Gamma]|_{\Gamma_t} = \boldsymbol{\sigma}^+(\boldsymbol{u},p)|_{\Gamma_t}\boldsymbol{n}_\Gamma - \boldsymbol{\sigma}^-(\boldsymbol{u},p)|_{\Gamma_t}\boldsymbol{n}_\Gamma.
\end{cases}
\end{aligned}
$$

4.3. Numerical approximation

In this section the numerical approximation of the mathematical models presented in the previous sections will be discussed. These models include the lumped parameters model of the whole circulation (Section 4.1), the 3D CFD model for the pre-operative scenario (Section 4.2.2) and the coupled 3D-0D FSI model for the post-operative/follow-up scenarios (Section 4.2.5).

The lumped parameters model is discretised in time using an explicit scheme while both the 3D models are discretised in time by using an implicit method of order 1 and adopting a semi-implicit treatment for the non-linear term (Section 4.3.1). Moreover, the three dimensional models of the pre-operative and post-operative/follow-up scenarios are discretised in space by means of the stabilised Finite Element (FE) method, in which the velocity and pressure are expressed using Lagrangian polynomial basis functions of equal degree (Section 4.3.2).

Finally, in the post-operative and follow-up scenarios, the reduced structure model of the valve (Equation (4.9)) is discretised using an explicit scheme (Section 4.3.3); whereas the the coupled reduced FSI (Section 4.2.5) is managed by means of a loosely coupled strategy (Section 4.3.4).

4.3.1. Time discretisation of the models

Lumped parameters model of the circulation. This model was discretised in time by meand of a *4th order Runge-Kutta scheme*. This is a one-step method which requires the evaluation of the right-hand side term multiple times at each time step, so that an accurate approximation is achieved [72].

To perform the time discretisation the time interval considered, e.g. [0,T], is divided with uniform step size obtaining the nodes $\{t^n\}_{n=0}^N$, where $\Delta t = T/N$ is the step size.

Considering the formulation in (4.1), the formulation resulting from this method application is:

$$\begin{cases} \boldsymbol{y}^{n+1} = f_1(t^n, \boldsymbol{y}^n, \boldsymbol{z}^{n+1}) \\ \boldsymbol{z}^{n+1} = f_2(t, \boldsymbol{y}^n) \\ y^0 = \boldsymbol{y}_0 \end{cases}$$

where the superscript $\cdot^n$ identifies the quantities evaluated at time t^n.

Fluid Models. The time discretisation of the three dimensional fluid models is carried out in the same way for all scenarios considered. As previously done for the lumped parameters model, we introduce a uniform partition of the interval [0,T] with step-size Δt and nodes $\{t^n\}_{n=0}^N$, where $\Delta t = T/N$. Accordingly, the time discrete counterparts of all quantities evaluated at time t^n will be denoted by the superscript $\cdot^n$.

The time discretisation is carried out by means of the Backwards Differentiation Formula (BDF) of order 1 and adopting a semi-implicit treatment for the non-linear term $\rho(\mathbf{u}\cdot\nabla)\mathbf{u}$ in (4.2) and (4.4).

Indeed, an explicit treatment of the non-linear term would allow the resolution by a linear system, reducing the computational cost; however, the resulting stability condition: $\Delta t \lesssim h^2$, where h is the mesh discretisation step, could be very restrictive since, in fluid dynamics, very refined grids, with a small h, are commonly adopted. Alternatively the fully implicit treatment could be used, but, even if it allows having an unconditionally stable method, it also implies the solution of an expensive non-linear system at each time step, so it was not chosen. All in all, the semi-implicit treatment allows to avoid, on one hand, the solving of a non-linear system as in the fully implicit treatment, and, on the other hand, to avoid the restrictive stability condition imposed by an explicit treatment.

Using the semi-implicit approach, the linearisation of a non-linear term implies a stability

condition of the following type:

$$\Delta t \ \leq \ C\frac{h}{||\boldsymbol{u}^{n-1}||_{L^\infty}}$$

where C is a real constant. This condition, in haemodynamics, is usually already satisfied for accuracy purposes.

In the end the time dependent term and the non-linear term will be expressed, respectively, in the following way:

$$\begin{aligned}\rho\frac{\partial \boldsymbol{u}}{\partial t} &\simeq \rho\ \frac{\boldsymbol{u}^n - \boldsymbol{u}^{n-1}}{\Delta t}\\ \rho(\boldsymbol{u}(t^n)\cdot\nabla)\boldsymbol{u}(t^n) \ &\simeq \ \rho(\boldsymbol{u}^{n-1}\cdot\nabla)\boldsymbol{u}^n.\end{aligned}$$

Therefore, the time discretised fluid problem for the pre-operative scenario will be:

$$\begin{cases}\rho\dfrac{\mathbf{u}^n - \mathbf{u}^{n-1}}{\Delta t} + \rho(\mathbf{u}^{n-1}\cdot\nabla)\mathbf{u}^n + \nabla p^n & \\ \quad -\mu\nabla\cdot(\nabla\mathbf{u}^n + (\nabla\mathbf{u}^n)^T) = 0 & in\ \Omega_{pvr},\\ \nabla\cdot\mathbf{u}^n = 0 & in\ \Omega_{pvr},\\ \mathbf{u}^n = 0 & on\ \Gamma_{wall},\\ \boldsymbol{\sigma}(\mathbf{u}^n, p^n)\mathbf{n} = p_{in}\mathbf{n} & on\ \Gamma_{in},\\ \boldsymbol{\sigma}(\mathbf{u}^n, p^n)\mathbf{n} = p_{outj}\mathbf{n} & on\ \Gamma_{out_j},\ j = 1, 2\,,\\ \mathbf{u}^0 = 0 & in\ \Omega_{pvr}\end{cases} \tag{4.14}$$

While, for the post-operative/follow-up scenarios, the time discretisation allows to re-write the problem as:

$$\begin{cases}\rho\dfrac{\mathbf{u}^n - \mathbf{u}^{n-1}}{\Delta t} + \rho(\mathbf{u}^{n-1}\cdot\nabla)\mathbf{u}^n + \nabla p^n & \\ \quad -\mu\nabla\cdot(\nabla\mathbf{u}^n + (\nabla\mathbf{u}^n)^T) + \dfrac{R}{\varepsilon}(\mathbf{u}^n - \mathbf{u}^n_\Gamma)\delta^n_{t,\varepsilon} = 0 & in\ \Omega_{pvr},\\ \nabla\cdot\mathbf{u}^n = 0 & in\ \Omega_{pvr},\\ \mathbf{u}^n = 0 & on\ \Gamma_{wall},\\ \boldsymbol{\sigma}(\mathbf{u}^n, p^n)\mathbf{n} = p_{in}\mathbf{n} & on\ \Gamma_{in},\\ \boldsymbol{\sigma}(\mathbf{u}^n, p^n)\mathbf{n} = p_{outj}\mathbf{n} & on\ \Gamma_{out_j},\ j = 1, 2\,,\\ \mathbf{u}^0 = 0 & in\ \Omega_{pvr}\end{cases} \tag{4.15}$$

Notice that the velocity $\boldsymbol{u}^{\boldsymbol{n}}_{\boldsymbol{\Gamma},\boldsymbol{h}}$ and the Dirac delta $\delta^n_{\varepsilon,h}$ will be provided by the solution of the valve model, as better detailed in Section 4.3.4.

4.3.2. Finite Element discretisation of the fluid model

The space discretisation of the problem will be carried out using the Finite Element method starting from the strong formulation of the problem: (4.2) for the pre-operative scenario and (4.4) for the post-operative/follow-up scenarios. Notice that these two formulations differ only because of the resistive penalty term, so in the following section the FE approximation for the pre-operative scenario will be presented, whereas the numerical approximation of the post-operative/follow-up cases can be derived by adding the approximation of the resistive penalty term.

Galerkin approximation. First, a tetrahedral mesh $\mathcal{T}_h$ for the domain Ω is introduced, then the following Finite Element space is defined:

$$X^r_h = \{x_h \ \in \ C^0(\overline{\Omega}) \ : \ x_h|_T \in \mathbb{Q}^r(T), \forall T \in \mathcal{T}_h\}$$

where $\mathbb{Q}^r$ denotes the space of polynomials with degree r with respect to each coordinate. Therefore, the velocity and pressure spaces are defined respectively as:

$$V^r_h = \{\boldsymbol{v}_h \ \in \ [X^r_h]^3 \ : \ \boldsymbol{v}_h = 0 \ on \ \Gamma_{wall}\}, \quad dim(V_h) = N_h < \infty \ \forall h > 0;$$
$$Q^r_h = X^r_h, \quad dim(Q_h) = M_h < \infty \ \forall h > 0.$$

Notice that $V^r_h \subset V = \{\boldsymbol{v} \in [H^1(\Omega)]^3 : \boldsymbol{v}|_{\Gamma_{wall}} = 0\}$ and $Q^r_h \subset Q = L^2(\Omega)$. Moreover, the discrete space V^r_h and Q^r_h are selected of the same order, first order, to reduce the computational error, so from now on the notation used will be V_h and Q_h. Finally, the functions $\boldsymbol{v}_h$ and q_h, belonging to the two correspondent functional spaces V_h and Q_h, are assumed as test functions.

The test functions are then multiplied, respectively, to the terms in the equations of momentum and mass conservation in the strong formulation of the problem and the resulting equations are integrated over the computational domain. Finally, the Neumann boundary conditions, already defined, are applied in the formulation.

Galerkin approximation of pre-operative scenario. Taking into account the steps mentioned above, and referring to the domain in Figure 4.3, in the pre-operative scenario

the conservation of the momentum equation becomes:

$$\int_{\Omega_{pre}} \rho \frac{\mathbf{u}^n - \mathbf{u}^{n-1}}{\Delta t} \cdot v_h \, d\Omega + \int_{\Omega_{pre}} \rho(\mathbf{u}_h^{n-1} \cdot \nabla)\mathbf{u}_h^n \cdot v_h \, d\Omega - \int_{\Omega_{pre}} \nabla \cdot \boldsymbol{\sigma}^n \cdot v_h \, d\Omega = 0 \quad (4.16)$$

where $\boldsymbol{\sigma}^n = p_h^n - \mu(\nabla \mathbf{u}_h^n + \nabla(\mathbf{u}_h^n)^T)$.

Considering the Cauchy stress tensor divergence integral in (4.16) and exploiting this definition of $\boldsymbol{\sigma}$, an integration by parts can be performed:

$$\begin{aligned}\int_{\Omega_{pre}} \nabla \cdot \boldsymbol{\sigma}^n \cdot \boldsymbol{v}_h \, d\Omega &= \int_{\Omega_{pre}} -\nabla p^n \cdot \boldsymbol{v}_h \, d\Omega + \int_{\Omega_{pre}} \mu \nabla \cdot (\nabla \mathbf{u}_h^n + \nabla(\mathbf{u}_h^n)^T) \cdot \boldsymbol{v}_h \, d\Omega \\ &= \int_{\Omega_{pre}} p^n \nabla \cdot \boldsymbol{v}_h \, d\Omega - \int_{\partial\Omega_{pre}} p^n \boldsymbol{n} \cdot \boldsymbol{v}_h d\gamma - \int_{\Omega_{pre}} \mu(\nabla \mathbf{u}_h^n + \nabla(\mathbf{u}_h^n)^T) : \nabla \boldsymbol{v}_h \, d\Omega \\ &\quad + \int_{\partial\Omega_{pre}} \mu \frac{\partial \boldsymbol{u}_h^n}{\partial \boldsymbol{n}} \cdot \boldsymbol{v}_h d\gamma \quad \forall \boldsymbol{v_h} \in V_h\end{aligned} \quad (4.17)$$

Exploiting the Neumann boundary conditions defined in (4.2) and the formulation of the Cauchy stress tensor divergence integral in (4.17) , the integral form of the momentum equation can be expressed in the following way:

$$\begin{aligned}&\int_{\Omega_{pre}} \rho \frac{\mathbf{u}^n - \mathbf{u}^{n-1}}{\Delta t} \cdot v_h \, d\Omega + \int_{\Omega_{pre}} \rho(\mathbf{u}_h^{n-1} \cdot \nabla)\mathbf{u}_h^n \cdot \boldsymbol{v}_h \, d\Omega - \int_{\Omega_{pre}} p^n \nabla \cdot \boldsymbol{v}_h \, d\Omega \\ &+ \int_{\Omega_{pre}} \mu(\nabla \mathbf{u}_h^n + \nabla(\mathbf{u}_h^n)^T) : \nabla \boldsymbol{v}_h \, d\Omega + \int_{\Gamma_{in}} p_{in}^n \boldsymbol{n} \cdot \boldsymbol{v}_h d\gamma \\ &+ \sum_{j=1,2} \int_{\Gamma_{outj}} p_{outj}^n \boldsymbol{n} \cdot \boldsymbol{v}_h d\gamma = 0 \quad \forall \boldsymbol{v}_h \in V_h\end{aligned}$$

As for the mass conservation equation, it is multiplied by the test function $q_h \in Q_h$:

$$\int_{\Omega_{pre}} \nabla \cdot \boldsymbol{u}_h^n \, q_h \, d\Omega \quad \forall q_h \in Q_h$$

The Galerkin approximation can also be re-written by introducing the following bilinear

and trilinear forms:

$$\begin{aligned} a(\boldsymbol{u},\boldsymbol{v}) &= \int_{\Omega_{pre}} \mu(\nabla \mathbf{u} + \nabla(\mathbf{u})^T) : \nabla \boldsymbol{v}\ d\Omega \\ b(\boldsymbol{v},q) &= -\int_{\Omega_{pre}} \nabla \cdot \boldsymbol{v}\ q\ d\Omega \\ c(\boldsymbol{w},\boldsymbol{u},\boldsymbol{v}) &= \int_{\Omega_{pre}} \rho(\mathbf{w}\cdot\nabla)\mathbf{u}\cdot\boldsymbol{v}\ d\Omega \\ F(\boldsymbol{v}) &= \int_{\Gamma_{in}} p_{in}\boldsymbol{n}\cdot\boldsymbol{v} d\gamma + \sum_{j=1,2}\int_{\Gamma_{outj}} p_{outj}\ \boldsymbol{n}\cdot\boldsymbol{v} d\gamma \end{aligned} \tag{4.18}$$

So that the Galerkin approximation of the pre-operative fluid model reads:

Find $\boldsymbol{u}_h^n \in V_h$ and $p \in Q_h$ for each $t \in (0,T]$ such that $\forall\ \boldsymbol{v}_h \in V_h$ and $\forall\ q_h \in Q_h$:

$$\begin{cases} \rho(\partial_t \boldsymbol{u}_h^n, \boldsymbol{v}_h) + a(\boldsymbol{u}_h^n, \boldsymbol{v}_h) + c(\boldsymbol{u}_h^n, \boldsymbol{u}_h^n, \boldsymbol{v}_h) + b(\boldsymbol{v}_h, p) = F(\boldsymbol{v}_h) \\ b(\boldsymbol{u}_h^n, q_h) = 0 \end{cases}$$

where the first term in the momentum conservation equation identifies the L^2 inner product:

$$(\boldsymbol{u}_h^n, \boldsymbol{v}_h) = \int_{\Omega_{pre}} \boldsymbol{u}_h^n \cdot \boldsymbol{v}_h d\Omega$$

Galerkin approximation of post-operative scenario. The models of the pre-operative and post-operative/follow-up scenarios differ only for the presence of the resistive penalty term in the latter. Thus, the post-operative model can be discretised in the same way as the pre-operative case, but taking into account the strong formulation in (4.4), so the additional term, and the domain in Figure 4.4. Therefore, the approximated momentum conservation equation is:

$$\begin{aligned} &\int_{\Omega_{pvr}} \rho\frac{\mathbf{u}^n - \mathbf{u}^{n-1}}{\Delta t}\cdot\boldsymbol{v}_h\ d\Omega + \int_{\Omega_{pvr}} \rho(\mathbf{u}_h^{n-1}\cdot\nabla)\mathbf{u}_h^n \cdot v_h\ d\Omega - \int_{\Omega_{pvr}} p^n \nabla\cdot\boldsymbol{v}_h\ d\Omega \\ &+ \int_{\Omega_{pvr}} \mu(\nabla\mathbf{u}_h^n + \nabla(\mathbf{u}_h^n)^T) : \nabla\boldsymbol{v}_h\ d\Omega + \int_{\Gamma_{in}} p_{in}^n \boldsymbol{n}\cdot\boldsymbol{v}_h d\gamma \\ &+ \sum_{j=1,2}\int_{\Gamma_{outj}} p_{outj}^n \boldsymbol{n}\cdot\boldsymbol{v}_h d\gamma + \int_{\Omega_{pvr}} \frac{R}{\varepsilon}(\boldsymbol{u}_h^n - \boldsymbol{u}_{h\Gamma}^n)\delta_{\Gamma,\varepsilon}\cdot\boldsymbol{v}_h\ d\Omega = 0 \quad \forall \boldsymbol{v}_h \in V_h; \end{aligned}$$

and the continuity equation is:

$$\int_{\Omega_{pvr}} \nabla \cdot \boldsymbol{u}_h^n \, q_h \, d\Omega \; = 0 \quad \forall q_h \in Q_h$$

Also in this scenario is possible to re-write the Galerkin approximation using bilinear and trilinear forms. Indeed, the forms already defined in (4.18), can be modified in order to take into account the presence of the resistive penalty term, in particular the $a(\boldsymbol{u}_h^n, \boldsymbol{v_h})$ and $F(\boldsymbol{v_h})$ are exploited to define the following forms:

$$\begin{aligned}
\tilde{a}(\boldsymbol{u}_h^n, \boldsymbol{v}_h) &= a(\boldsymbol{u}_h^n, \boldsymbol{v}_h) + r(\boldsymbol{u}_h^n, \boldsymbol{v}_h) \\
&= \int_{\Omega_{pvr}} \mu(\nabla \mathbf{u}_h + \nabla \mathbf{u}_h^T) : \nabla \boldsymbol{v}_h \, d\Omega + \int_{\Omega_{pvr}} \frac{R}{\varepsilon} \boldsymbol{u}_h^n \delta_{\Gamma,\varepsilon}^n \cdot \boldsymbol{v}_h \, d\Omega \\
\tilde{F}(\boldsymbol{v}) &= F(\boldsymbol{v}_h) + R(\boldsymbol{v}_h) \\
&= -\int_{\Gamma_{in}} p_{in}^n \boldsymbol{n} \cdot \boldsymbol{v}_h d\gamma - \sum_{j=1,2} \int_{\Gamma_{outj}} p_{outj}^n \boldsymbol{n} \cdot \boldsymbol{v}_h d\gamma + \int_{\Omega_{pvr}} \frac{R}{\varepsilon} \boldsymbol{u}_{h\Gamma}^n \delta_{\Gamma,\varepsilon}^n \cdot \boldsymbol{v}_h \, d\Omega
\end{aligned}$$

So the approximated formulation of the post-operative fluid model is:

Find $\boldsymbol{u}_h^n \in V_h$ and $p^n \in Q_h$ for each $t \in (0, T]$ such that $\forall \, \boldsymbol{v}_h \in V_h$ and $\forall \, q_h \in Q_h$:

$$\begin{cases} \rho(\partial_t \boldsymbol{u}_h^n, \boldsymbol{v}_h) + \tilde{a}(\boldsymbol{u}_h^n, \boldsymbol{v}_h) + c(\boldsymbol{u}_h^n, \boldsymbol{u}_h^n, \boldsymbol{v}_h) + b(\boldsymbol{v}_h, p^n) = \tilde{F}(\boldsymbol{v}_h) \\ b(\boldsymbol{u}_h^n, q_h) = 0 \end{cases}$$

where the first term in the momentum conservation equation identifies the following integral:

$$(\boldsymbol{u}_h^n, \boldsymbol{v}_h) = \int_{\Omega_{pvr}} \boldsymbol{u}_h^n \cdot \boldsymbol{v}_h d\Omega$$

Fully discretised models. Finally, if considering both the discretisations in time and space, the fully discretised fluid problem reads:

Given $u_h^0 = 0$, find $u_h^n \in V_h$ and $p_h^n \in Q_h$ for each $n = 1, \ldots, N$ such that $\forall \, \boldsymbol{v}_h \in V_h$ and $\forall \, q_h \in Q_h$:

- In the pre-operative scenario:

$$\left(\rho\frac{\boldsymbol{u}_h^n-\boldsymbol{u}_h^{n-1}}{\Delta t},\boldsymbol{v}_h\right)+a(\boldsymbol{u}_h^n,\boldsymbol{v}_h)+c(\boldsymbol{u}_h^{n-1},\boldsymbol{u}_h^n,\boldsymbol{v}_h)+b(\boldsymbol{v}_h,p^n)-b(\boldsymbol{u}_h^n,q_h)=F^n(\boldsymbol{v}_h); \tag{4.19}$$

- In the post-operative/follow-up scenarios:

$$\left(\rho\frac{\boldsymbol{u}_h^n-\boldsymbol{u}_h^{n-1}}{\Delta t},\boldsymbol{v}_h\right)+\tilde{a}(\boldsymbol{u}_h^n,\boldsymbol{v}_h)+c(\boldsymbol{u}_h^{n-1},\boldsymbol{u}_h^n,\boldsymbol{v}_h)+b(\boldsymbol{v}_h,p^n)-b(\boldsymbol{u}_h^n,q_h)=\tilde{F}^n(\boldsymbol{v}_h). \tag{4.20}$$

Stabilisation. Choosing the same order for the discrete spaces V_h^r and Q_h^r allows reducing the computational effort linked to the problem solving; however, this implies the choice of a suitable stabilisation method.

Indeed, the *inf-sup condition*, which guarantees solvability of the discretised fluid problem and reads:

$$\exists\,\beta>0\ :\ \forall q_h\in Q_h,\exists\,v_h\in V_h\ :\ b(q_h,\boldsymbol{h}_h)\geq\beta||\boldsymbol{v}_h||_V||q_h||_Q \tag{4.21}$$

is violated when the finite elements used for pressure and velocity have the same order. This implies that :

$$\exists\,\tilde{q_h}\in Q_h\ :\ \forall\boldsymbol{v}_h\in V_h\quad b(\tilde{q_h},\boldsymbol{v}_h)=0,$$

meanining that the solution loses its unicity.

In addition to the instability caused by the violation of the inf-sup condition, the instability connected to the flow regime has to be considered. Indeed, especially in the region of the valve, the regime can be described as highly advective; when a problem is dominated by advection, numerical oscillations could generate and impair the reliablity of the solution found.

To prevent this situation, a possible solution would be to reduce the mesh size; however, the constraint imposed on the mesh size could become too restrictive and the computational cost could significantly increase. To avoid this increase in the computational effort, stabilisation methods are commonly used. In this work, for the stabilization, the *Streamline Upwind Petrov-Galerkin - Pressure-Stabilising Petrov-Galerkin (SUPG-PSPG)* approach was adopted.

The PSPG method is responsible for the stabilisation connected to the violation of the inf-sup condition while the SUPG method is linked to the stabilization related to the advective nature of the problem. All in all the approach consists in adding the term $S(\boldsymbol{u}_h^n, \boldsymbol{u}_h^{n-1}, p_h^n; \boldsymbol{v}_h, q_h)$, to the discretised formulation of the Navier-Stokes equation in (4.19) and (4.20) [9, 32].

A second type of stabilisation used was *backflow stabilisation*, employed in all three scenarios considered. Indeed, typically, simulations of the haemodynamics can be characterised by instability at the artificial boundaries if Neumann boundary conditions are applied. This is related to the advective term of the momentum conservation equation which influences the energy balance, making it unstable when the velocity and the normal of the boundary are characterised by opposite verse. Consequently, large oscillations of the velocity near the outlet could take place [12]. This happens mainly during the diastole, when a backflow could be established. Without the stabilisation, the velocity vectors would assume different directions instead of adhering to one, i.e. the normal to the artery cross section area.

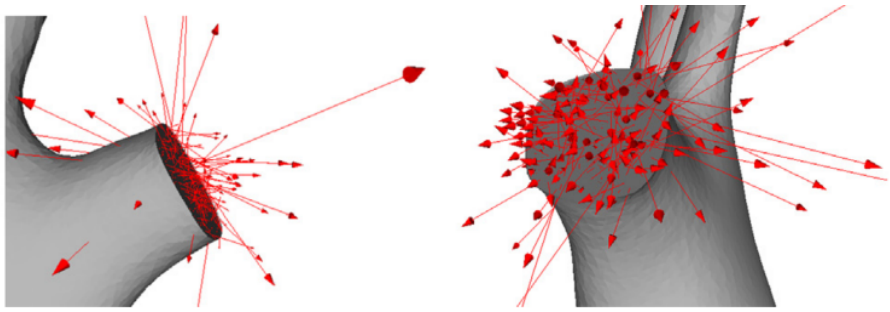

Figure 4.7: An example of the instabilities which can occur when Neumann boundary conditions are applied at the artificial boundaries and a backflow is established, in red the velocity vectors at the outlet [12].

The stabilisation consists in the addition of a term to the momentum conservation equation, in the form:

$$S = \tilde{\beta}\frac{\rho}{2}(\boldsymbol{u}\cdot\boldsymbol{n})_{-}\boldsymbol{u} \tag{4.22}$$

where $\tilde{\beta}$ is a constant and $(\boldsymbol{u}\cdot\boldsymbol{n})_{-}$ is defined as :

$$(\boldsymbol{u}\cdot\boldsymbol{n})_{-} = \begin{cases} -\boldsymbol{u}\cdot\boldsymbol{n} & if\ \boldsymbol{u}\cdot\boldsymbol{n} < 0 \\ 0 & if\ \boldsymbol{u}\cdot\boldsymbol{n} \geq 0. \end{cases}$$

Guaranteeing that the flow follows the direction of the normal to the pulmonary artery

cross section area is particularly relevant in the case of the two outlets; this would allow to simulate the physiological condition in which the flow would continue also after the artificial boundary following the same direction. For this reason the backflow stabilisation was applied at the two outlets of the patients' geometries.

So, considering the term introduced, the outlets boundary conditions read:

$$\sigma(\boldsymbol{u}, p)\boldsymbol{n} = p_{out}\boldsymbol{n} + S,$$

where S was defined in (4.22).

The stabilisation term in (4.22) has to be properly discretised in time by using a method coherent with the one used for the rest of the 3D fluid models. In particular this term is discretised analogously to the advective term in the momentum equation of the formulations (4.14) and (4.15):

$$-\tilde{\beta}\frac{\rho}{2}(\boldsymbol{u}^{n-1}\cdot\boldsymbol{n})\_\boldsymbol{u}^n$$

Finally, taking into account also the space discretisation carried out for the rest of the model, the backflow stabilisation term can be expressed analogously using the form $e(\boldsymbol{u}_h^n, \boldsymbol{u}_h^{n-1}, \boldsymbol{v}_h)$ and will be added to the fully discretised formulations (4.19) and (4.20).

A third addition to the formulation is linked to the use of a turbulence model. Indeed, taking into consideration the highly advective nature of the phenomena studied, we chose to model also the effect of the possible turbulence presence.

This was carried out by modifying the diffusion term in the formulation of all three scenarios. In particular, the *sigma-LES* model was adopted [63], meaning that the viscosity μ is substituted by the viscosity $\tilde{\mu} = \mu + \mu_{sgs}$ where μ_{sgs} is the turbolent viscosity defined as:

$$\mu_{sgs} = \rho(C\,h)^2\frac{\sigma_3(\sigma_1-\sigma_2)(\sigma_2-\sigma_3)}{\sigma_1^2};$$

C is a suitable constant, h is the average element size and $\sigma_1(\boldsymbol{x},t) \geq \sigma_2(\boldsymbol{x},t) \geq \sigma_3(\boldsymbol{x},t)$ are the singular values of $\nabla\boldsymbol{u}^{n-1}$, in the advection term of the formulations (4.19) and (4.19).

With all these modifications, the formulations (4.19) and (4.20) can be re-written as:

- In the pre-operative scenario:

$$\begin{aligned}&\left(\rho\frac{\boldsymbol{u}_h^n-\boldsymbol{u}_h^{n-1}}{\Delta t},\boldsymbol{v}_h\right) + a(\boldsymbol{u}_h^n,\boldsymbol{v}_h) + c(\boldsymbol{u}_h^{n-1},\boldsymbol{u}_h^n,\boldsymbol{v}_h) + b(\boldsymbol{v}_h,p^n) - b(\boldsymbol{u}_h^n,q_h) + \\ &S(\boldsymbol{u}_h^n,\boldsymbol{u}_h^{n-1},p_h^n;\boldsymbol{v}_h,q_h) + e(\boldsymbol{u}_h^n,\boldsymbol{u}_h^{n-1},\boldsymbol{v}_h) = F^n(\boldsymbol{v}_h);\end{aligned} \tag{4.23}$$

- In the post-operative/follow-up scenarios:

$$\left(\rho\frac{\boldsymbol{u}_h^n-\boldsymbol{u}_h^{n-1}}{\Delta t},\boldsymbol{v}_h\right)+\tilde{a}(\boldsymbol{u}_h^n,\boldsymbol{v}_h)+c(\boldsymbol{u}_h^{n-1},\boldsymbol{u}_h^n,\boldsymbol{v}_h)+b(\boldsymbol{v}_h,p^n)-b(\boldsymbol{u}_h^n,q_h)+ \\ S(\boldsymbol{u}_h^n,\boldsymbol{u}_h^{n-1},p_h^n;\boldsymbol{v}_h,q_h)+e(\boldsymbol{u}_h^n,\boldsymbol{u}_h^{n-1},\boldsymbol{v}_h)=\tilde{F}^n(\boldsymbol{v}_h). \tag{4.24}$$

Algebraic formulation. The problem defined until now can be re-written as an algebraic linear system, this is performed by expressing every term of the formulation in an algebraic form.

To carry this out, we introduce the scalar basis function $\{\Phi_j(\boldsymbol{x})\}_{j=1}^{N_h}$ for the discrete space V_h and the vectorial basis function $\{\Psi_k(\boldsymbol{x})\}_{k=1}^{M_h}$ for the discrete space Q_h. We define also the vectorial basis function for the space X_h^r: $\{\Phi_j(\boldsymbol{x})\}_{j=1}^{K_h}$, where $3K_h=N_h$, such that the basis function of V_h can be constructed as:

$$\left\{\begin{bmatrix}\Phi_1\\0\\0\end{bmatrix},\begin{bmatrix}\Phi_2\\0\\0\end{bmatrix},\ldots,\begin{bmatrix}\Phi_{K_h}\\0\\0\end{bmatrix},\begin{bmatrix}0\\\Phi_1\\0\end{bmatrix},\begin{bmatrix}0\\\Phi_2\\0\end{bmatrix},\ldots,\begin{bmatrix}0\\\Phi_{K_h}\\0\end{bmatrix},\begin{bmatrix}0\\0\\\Phi_1\end{bmatrix},\begin{bmatrix}0\\0\\\Phi_2\end{bmatrix},\ldots,\begin{bmatrix}0\\0\\\Phi_{K_h}\end{bmatrix}\right\}$$

In this formulation, the total number of degrees of freedom is: $N=N_h+M_h=3K_h+M_h$.

The solution of the discrete problem can be defined as a linear combination of the basis functions

$$\begin{aligned}\boldsymbol{u}_h^n(\boldsymbol{x})&=\sum_{j=1}^{N_h}u_j^n\Phi_j(\boldsymbol{x})= \\ &=\sum_{j=1}^{K_h}u_j^n\begin{bmatrix}\Phi_j(\boldsymbol{x})\\0\\0\end{bmatrix}+\sum_{j=1}^{K_h}u_{K_h+j}^n\begin{bmatrix}0\\\Phi_j(\boldsymbol{x})\\0\end{bmatrix}+\sum_{j=1}^{K_h}u_{2K_h+j}^n\begin{bmatrix}0\\0\\\Phi_j(\boldsymbol{x})\end{bmatrix}, \\ p_h^n(\boldsymbol{x})&=\sum_{k=1}^{M_h}p_k^n\Psi_k(\boldsymbol{x}),\end{aligned}$$

where $\{u_j^n\}_{j=1}^{3K_h}$ and $\{p_k^n\}_{k=1}^{M_h}$, for $n=1,\ldots,N$ are coefficients.

To describe the current problem, considering all three scenarios, we introduce $\boldsymbol{v}_h=\Phi_i$ and $q_h=\Psi_l$, $\forall i=1,\ldots,N_h$ and $\forall l=1,\ldots,M_h$, which can be substituted in (4.19) and (4.20).

Secondly, we introduce the vectors:

- $\boldsymbol{U}^n=[u_1^n,\ldots,u_{N_h}^n]^T$

- $\boldsymbol{P}^n = [p_1^n, \dots, u_{M_h}^n]^T$
- $\boldsymbol{F}^n = [F^n(\Phi_1(\boldsymbol{x})), \dots, F^n(\Phi_{N_h}(\boldsymbol{x}))]^T$

Lastly, we define the following matrices in order to re-write the problem in algebraic form:

- The mass matrix: $M \in \mathbb{R}^{N_h \times N_h} \ : \ M_{ij} = \int_\Omega \Phi_j \cdot \Phi_i$,
- The stiffness matrix $A \in \mathbb{R}^{N_h \times N_h} \ : \ A_{ij} = a(\Phi_j, \Phi_i)$,
- The resistive matrix $R^n \in \mathbb{R}^{N_h \times N_h} \ : \ R_{ij}^n = r^n(\Phi_j, \Phi_i)$, (present only in the post-operative/follow-up scenarios)
- The advective matrix $N \in \mathbb{R}^{N_h \times N_h} \ : \ [N(\boldsymbol{U}^{n-1})]_{ij} = c(\boldsymbol{u}_h^{n-1}, \Phi_j, \Phi_i)$,
- the matrix $B \in \mathbb{R}^{M_h \times M_h} \ : \ B_{ij} = b(\Phi_j, \Psi_i)$
- the matrix $E \in \mathbb{R}^{N_h \times N_h} \ : \ [E(\boldsymbol{U}^{n-1})]_{ij} = \tilde{\beta}(\frac{\rho}{2}(\boldsymbol{u}_h^{n-1} \cdot \boldsymbol{n})\_\Phi_j, \Phi_i)_{\Gamma_{out}}$ (accounting for the backflow stabilisation)

For the pre-operative scenario the following terms are defined:

- $(\boldsymbol{F}^n)_i = \left(\rho \frac{M}{\Delta t} \boldsymbol{U}^{n-1}\right)_i - \int_{\Gamma_{in}} p_{in}^n \boldsymbol{n} \cdot \Phi_i d\gamma - \int_{\Gamma_{outj}} p_{outj}^n \boldsymbol{n} \cdot \Phi_i d\gamma$
- $K = \rho \frac{M}{\Delta t} + A + N(\boldsymbol{U}^{n-1}) + E(\boldsymbol{U}^{n-1}) + \Sigma_{11}$,
- $\tilde{\boldsymbol{F}}^n = \boldsymbol{F}^n + \boldsymbol{F}_u^n$,

where Σ_{11} and F_u^n are terms introduced by the SUPG-PSPG stabilisation.

Instead, for the post-operative/follow-up scenarios the terms defined are:

- $(\boldsymbol{F}^n)_i = \left(\rho \frac{M}{\Delta t} \boldsymbol{U}^{n-1}\right)_i - \int_{\Gamma_{in}} p_{in}^n \boldsymbol{n} \cdot \Phi_i d\gamma - \int_{\Gamma_{outj}} p_{outj}^n \boldsymbol{n} \cdot \Phi_i d\gamma + \left(\frac{R}{\varepsilon} \boldsymbol{u}_{\Gamma,h}^n \delta_{\Gamma,\varepsilon,h}^n, \Phi_i\right)$,
- $K = \rho \frac{M}{\Delta t} + A + R^n + N(\boldsymbol{U}^{n-1}) + E(\boldsymbol{U}^{n-1}) + \Sigma_{11}$,
- $\tilde{\boldsymbol{F}}^n = \boldsymbol{F}^n + \boldsymbol{F}_u^n$

in this case the resistive penalty term is accounted for.

The following algebraic system is obtained:

$$\begin{bmatrix} K(\boldsymbol{U}^{n-1}) & B^T + \Sigma_{12} \\ B + \Sigma_{21} & \Sigma_{22} \end{bmatrix} \begin{bmatrix} \boldsymbol{U}^n \\ \boldsymbol{P}^n \end{bmatrix} = \begin{bmatrix} \tilde{\boldsymbol{F}}^n \\ \boldsymbol{F}_p^n \end{bmatrix},$$

where the matrices Σ_{12} , Σ_{21} , Σ_{22} and F_p^n are accounting for the use of SUPG-PSPG stabilisation. Moreover, notice that K and $(\boldsymbol{F}^n)_i$ change with respect to the scenario considered.

4.3.3. Numerical approximation of the structure model of the valve

The geometric quantities characterising the valve in the reduced structural model are described using a Finite Elements description; however, since some of these quantities only appear inside of integrals, not all of them have to actually belong to a FE space.

Specifically, the distance function is approximated by $\varphi_h^n \in X_h^s$ at each time t^n with a polinomial degree $s \geq 2$ which is in general different from the degree adopted for the fluid finite elements; then $\delta_{\varepsilon,h}^n$ is defined accordingly. Notice that the half-thickness ε must be at least 1.5 times larger than h in order for $\delta_{\varepsilon,h}^n$ to be solved correctly by the mesh [26].

We can introduce a basis function of $X_h^s : \{\psi_k\}_{k=1}^{N_h^s}$, so that the distance function can be re-written as: $\varphi_h^n = \Sigma_{k=1}^{N_h^s} \varphi_k^n \psi_k$. Moreover, also the leaflets extended normal and curvature can be defined analogously as functions of φ_k^n and ψ_k so that we have $\tilde{\boldsymbol{n}_{\Gamma,h}}^n(\varphi_k^n, \psi_k)$ and $\tilde{H}_{\Gamma,h}^n(\varphi_k^n, \psi_k)$.

Since both these quantities appear only inside integrals, see (4.12) and (4.13) in the valve model, the expressions of $\tilde{\boldsymbol{n}}_{\Gamma,h}^n(\varphi_k^n, \psi_k)$ and $\tilde{H}_{\Gamma,h}^n(\varphi_k^n, \psi_k)$ can be used directly without performing their projection onto a finite element space.

Finally, the valve velocity must be described at the discrete level, to do this we exploit its dependency on $c(t)$, see (4.11). Thus, using a first order approximation, we obtain that:

$$\boldsymbol{u}_{\Gamma,h}^n = \frac{c^n - c^{n-1}}{\Delta t} \tilde{\boldsymbol{n}}_{\Gamma,h}^n. \tag{4.25}$$

All in all, the ODE in (4.9), is solved using an explicit method, namely the 4th order Runge-Kutta method.

4.3.4. Numerical approximation of the reduced 3D-0D FSI model

This section has the aim to sum up the steps leading to the solution of the reduced 3D-0D FSI model adopted for the post-operative and follow-up scenarios. Indeed, unlike the pre-operative case, in which the absence of the valve allows to solve only the fluid problem using the CFD approach, in these cases the coupling with the reduced structure model of the valve must be considered.

Given the discretisation carried out in Sections 4.3.2 and 4.3.3, the fluid and structure models are weakly coupled at each time step, meaning that the fluid model and the structure model exchange informations at each time step.

After the reduced structural model expressed by (4.9) is solved by means of a 4th order Runge-Kutta method, the opening coefficient c^n at the current time step t^n is found. This variable allow to compute the displacement $\boldsymbol{d}_\Gamma^n$ of the leaflets surface from the previous configuration to the current one.

Finding the new configuration of the leaflets surface also allows to compute the distance function φ_h^n, and consequently the surface smearing introduced by the Dirac delta $\delta_{\Gamma,\varepsilon}^n$, the leaflets normal extension $\tilde{\boldsymbol{n}}$ and the leaflets curvature extension $\tilde{H}$.

At this point, using the equation (4.25), it is possible to find the valve velocity $\boldsymbol{u}_{\Gamma,h}^n$. The valve velocity $\boldsymbol{u}_{\Gamma,h}^n$ and the function $\delta_{\Gamma,\varepsilon}^n$ are, then, passed to the 3D fluid model, in particular Equation (4.24) is solved.

Finally, using the expression in (4.12), the fluid problem solution $(\boldsymbol{u}_h^n, p_h^n)$ allow to compute the stress on the valve $\boldsymbol{f}$ at the step t^n which will be then used to solve the reduced structure problem at time step t^{n+1}.

Summing up, the fluid exchanges with the valve the stress $\boldsymbol{f}^{n-1}(\boldsymbol{u}_h^{n-1}, p_h^{n-1})$, while the valve model provides to the fluid problem the position φ_h^n and the velocity $\boldsymbol{u}_{\Gamma,h}^n$ of the leaflets.

Therefore, the following scheme can be defined [34, 60]:

Algorithm 4.1 Scheme for the solution of the reduced FSI model

Given $\boldsymbol{u_h^n}, p_h^n, c^n$ for $n = 0$, and computed the functions $\varphi^n, \tilde{\boldsymbol{n}}_\Gamma^n, \tilde{H}^n$ corresponding to the surface Γ^n for n=0

for $n = 1$ to N **do**

1. Compute the integrals that make up (4.9), in terms of $\boldsymbol{u}_h^{n-1}, p_h^{n-1}, \Gamma^{n-1}, \varphi^{n-1}$ through (4.12) and (4.13);
2. Find c^n by advancing the 0D equation (4.9) with a step of an explicit 4th order Runge-Kutta method;
3. Create the immersed surface Γ^n moving the previous configuration Γ^{n-1} by $\boldsymbol{d_\Gamma^n} = (c^n - c^{n-1})\boldsymbol{g}$
4. Compute the new signed distance function φ^n with respect to Γ^n and assemble the normal and curvature fields $\tilde{\boldsymbol{n}}_\Gamma^n$ and $\tilde{H}^n$;
5. Compute the leaflets velocity $\boldsymbol{u}_\Gamma^n = \dfrac{c^n - c^{n-1}}{\Delta t}\tilde{\boldsymbol{n}}_{\Gamma,h}^n$;
6. Find $(\boldsymbol{u}_h^n, p_h^n) \in V_h \times Q_h$ by solving the problem (4.24)

end for

5 | Numerical simulations: Results and discussion

The numerical simulations were performed exploiting the computational domains of the two patients, see Chapter 3, and the mathematical models described in Section 4.1 and 4.2.

In particular, we performed three simulations for each patient:

- *Pre*: for the pre-operative scenario, the geometries lacking the pulmonary valve were employed, see Figures 3.9 and 4.3. For this simulation we refer to the mathematical model in (4.2), so a Computational Fluid Dynamics model is used. The boundary conditions for these simulations were provided using the Pre-0D model of the circulation described in Section 4.1.
- *Post*: for the post-operative scenario, the computational domain used included the presence of the cylinder which models the prosthetic valve pericardial sleeve virtually inserted. Moreover the presence of the valve was considered, see Figures 3.9 and 4.4. In this case we refer to the fluid mathematical model in (4.4) and the reduced structure model described in Section 4.2.4, these two are coupled as discussed in Section 4.2.5 and constitute a reduced Fluid-Structure Interaction model. Also in this case the boundary conditions were obtained by means of the lumped parameter model of the whole circulation, however the Valve-0D model was used (Section 4.1).
- *Follow-up*: in the follow-up scenario, we used again the computational domain which includes the presence of the stented valve (see Figures 3.9 and 4.4). The mathematical model describing this scenario is still given by the coupling between the fluid model in (4.4) and the reduced structure model in Section 4.2.4, as detailed in Section 4.2.5. What changes with respect to the post-operative scenario is the calibration of the Valve-0D model (Section 4.1) to account for the restoration of the cardiac function, which provided different boundary conditions.

The numerical problem is solved through life^{x} [2, 53], a high-performance Finite Element

library, written in C++ and based on the deal.II Finite Element core [4, 5, 22]. life^x is developed by the MOX Laboratory of Politecnico di Milano, in the context of the iHEART project and it can solve multiphysics problems pertaining to the function of the heart and cardiovascular system [14, 15, 23, 27, 77].

The numerical simulations have been performed on the clustered computational resources of Politecnico di Milano, in the queue gigatlong on a processor relying on 5 nodes with 280 cores 2x Xeon Gold 6238R (2.20GHz) 2.5TB RAM. The simulations have been performed with 56 cores selected. The simulations are set using a parameters file, a script in the .prm format, which contains the needed information related to the physical parameters, the addressed tags of the domain boundary to which impose boundary conditions, and also to the path of the computational mesh and the valve surface, if used.

In the next sections, will be described the setting of the simulations and the results will be discussed. In particular, in Section 5.1 we describe the calibration of the lumped parameters model which allowed to differentiate the three scenarios in terms of boundary conditions. In Section 5.2, the settings used to perform the CFD and reduced FSI simulations will be presented, specifically, the settings of the valve model will be discussed. In Sections 5.3 and 5.4, the results of the simulations carried out using the discussed models will be introduced and analysed.

5.1. Calibration of the Lumped Parameters model of the circulation

As previously mentioned, the lumped parameters model for the whole circulation was used to obtain three pressure sets which are the boundary conditions applied to the artificial boundaries of the 3D models of each scenario considered.

Wanting to reproduce boundary conditions coherent with the clinical condition of the patients in all three scenarios, we analysed the patients' available clinical data and we tried to exploit the lumped parameters model of the circulation in order to reproduce them.

Specifically, the clinical data at our disposal belonged to Patient 1 and described the patient's condition 6 months and 9 years after the pulmonary valve replacement (PVR). Indeed, we used this data as a reference for the post-operative and follow-up scenarios, respectively.

The clinical condition of the patient was described in terms of End-Systolic Volume (ESV),

i.e. the residual volume present in the ventricle after the ejection of blood in the systolic phase, End-Diastolic Volume (EDV), i.e. the volume present in the ventricle at the end of the diastole phase, and Ejection Fraction (EF), calculated as $\frac{EDV-ESV}{EDV}$, (see also Section 1.1). In Table 5.1, the clinical data concerning Patient's 1 right heart is summed up and complemented by reference values for a healthy adult.

	Patient 1	**Patient 1**	**Healthy adult** [91]
	6 months after PVR	9 years after PVR	no PVR
ESV (ml)	105	58	39 -49
EDV (ml)	165	110	91-111
EF%	35	47	54-57

Table 5.1: Values of the clinical measurements about SV, ESV, EDV and EF for Patient 1 right heart and for the average healthy adult right heart [91].

In particular, the calibration of the lumped parameters model was carried out by fitting the Ejection Fraction values, since it allows having an indicator of the proper functioning of the heart.

For the pre-operative scenario, there was not available data which described the patient's condition before the surgery. We overcame this problem by making some assumptions.

First, we considered that the right ventricle tends to reacquire its normal functionality years after the pulmonary valve replacement. This can be observed directly from Table 5.1, in which the reference values for the healthy adult are more comparable to the data measured 9 years after the surgery than 6 months after. Then, we hypothesise that, since 6 months after the surgery the heart has not fully recovered its functions, the patient's clinical data before the surgery and 6 months after will be comparable. This assumption is supported not only by the data shown in Table 5.1, but also by [38]. In this study, indeed, it is shown that the Ejection Fraction values have a negligible change if the data from the pre-operative condition and 6 months after the surgery is compared.

Therefore, when performing the lumped parameters model calibration, we assumed that the clinical data describing the post-operative scenario could be used as a reference also for the pre-operative scenario.

Since patient's 2 clinical data were not available, the calibration procedure was carried out entirely for Patient 1. Then we hypothesised that, due to the similar clinical history of the two patients, the pressure sets extracted from the numerical simulation of the circulation,

carried out for the three scenarios using the calibrated parameters, were suitable also to be used as boundary conditions on Patient's 2 geometry artificial boundaries.

In the lumped parameters model, the parameters governing the right circulation can be summed up in:

- The elastance of the right heart: this is governed by two parameters, E_a and E_b;
- The RLC circuit describing the pulmonary arterial circulation: this is controlled by the resistance R_{art}, the capacitance C_{art} and the inductance i_{art};
- The non-ideal diode representing the pulmonary valve: in particular, this model is governed by two resistances R_{max} and R_{min} which allow to the describe the behaviour of the pulmonary valve, and an inductance I_v;
- The volume of the right atrium and right ventricle at the initial instant of the simulation, indicated with V_{RA} and V_{RV}.

In the process of calibration, these parameters were iteratively changed until finding an optimal value of Ejection Fraction, namely a value which was equal or at least characterised by a negligible difference with respect to the value measured on Patient 1 (in Table 5.1).

Notice that, as already discussed in Section 4.1, for the pre-operative scenario the Pre-0D model was used, taking into account the absence of the pulmonary valve also in the lumped parameters model of the circulation. In the case of the post-operative and follow-up scenarios instead, the model used was the Valve-0D model, characterised by the presence of the valve modelled through a non-ideal diode.

The values of the calibrated parameters used to obtain the boundary conditions in all three scenarios and the corresponding Ejection Fraction values found are summed up in Table 5.2. The values found for the ejection fraction using the lumped parameters model were very close to the Patient's 1 values in Table 5.1; indeed in the post-operative scenario they differ by 10% and in the follow-up scenario by 12.5%. Moreover in the pre-operative case, even if we do not have a reference value, the Ejection Fraction value is close to the post-operative one, coherently with the assumptions made previously.

	Pre-operative	**Post-operative**	**Follow-up**
	before PVR	6 months after PVR	9 years after PVR
Right ventricle			
$E_a(mmHg \cdot ml^{-1})$	0.07	0.1	0.24
$E_b(mmHg \cdot ml^{-1})$	0.09	0.08	0.08
Right arterial system			
$R_{art}(mmHg \cdot s \cdot ml^{-1})$	0.05	0.05	0.07
$C_{art}(ml \cdot mmHg^{-1})$	7.0	7.0	8.0
$I_{art}(mmHg \cdot s^2 \cdot ml^{-1})$	5e-3	5e-3	5e-3
Pulmonary valve			
$R_{max}(mmHg \cdot s \cdot ml^{-1})$	0.0225	75006.2	75006.2
$R_{min}(mmHg \cdot s \cdot ml^{-1})$	0.0075	0.0225	0.0225
$I_v(mmHg \cdot s^2 \cdot ml^{-1})$	0	0	0
$V_{RA}(ml)$	45	45	45
$V_{RV}(ml)$	165	165	110
EF%	35.1	38.8	52.9

Table 5.2: The calibrated parameters used in the lumped parameters model to obtain the pressure sets applied as boundary conditions of the 3D models, the initial volumes used for right ventricle V_{RV} and right atrium V_{RA}, and the Ejection Fraction value found by the numerical simulations of the circulation with the calibrated parameters for each scenario.

Regarding the setting of the right ventricle volume, the values chosen coincide with Patient's 1 EDV in Table 5.1; the simulations of the whole circulation indeed were started at the end of the diastole. As for the right atrium, a value coherent with respect to the literature analysed was chosen since there was not available Patient's 1 data. All of the other parameters in the model of the circulation were set as to reproduce physiological values for the systemic circulation and are listed in Table 5.3. Finally, the left ventricle EDV was extracted from Patient's 1 available measurements.

Parameters	**Values set**
Right Atrium	
$E_a(mmHg \cdot ml^{-1})$	0.06
$E_b(mmHg \cdot ml^{-1})$	0.07
Pulmonary venous system	
$R_{ven}(mmHg \cdot s \cdot ml^{-1})$	0.035684
$C_{ven}(ml \cdot mmHg^{-1})$	16.0
$I_{ven}(mmHg \cdot s^2 \cdot ml^{-1})$	5e-4
Left Atrium	
$E_a(mmHg \cdot ml^{-1})$	0.07
$E_b(mmHg \cdot ml^{-1})$	0.09
$V_{LA}(ml)$	52.0
Left Ventricle	
$E_a(mmHg \cdot ml^{-1})$	2.75
$E_b(mmHg \cdot ml^{-1})$	0.08
$V_{LV}(ml)$	110
Systemic arterial system	
$R_{art}(mmHg \cdot s \cdot ml^{-1})$	0.64
$C_{art}(ml \cdot mmHg^{-1})$	1.2
$I_{art}(mmHg \cdot s^2 \cdot ml^{-1})$	5e-3
Systemic venous system	
$R_{ven}(mmHg \cdot s \cdot ml^{-1})$	0.26
$C_{ven}(ml \cdot mmHg^{-1})$	60.0
$I_{ven}(mmHg \cdot s^2 \cdot ml^{-1})$	5e-4
Mitral valve	
$R_{max}(mmHg \cdot s \cdot ml^{-1})$	75006.2
$R_{min}(mmHg \cdot s \cdot ml^{-1})$	0.0075
$I_v(mmHg \cdot s^2 \cdot ml^{-1})$	0
Tricuspid valve	
$R_{max}(mmHg \cdot s \cdot ml^{-1})$	75006.2
$R_{min}(mmHg \cdot s \cdot ml^{-1})$	0.0075
$I_v(mmHg \cdot s^2 \cdot ml^{-1})$	0
Aortic valve	
$R_{max}(mmHg \cdot s \cdot ml^{-1})$	75006.2
$R_{min}(mmHg \cdot s \cdot ml^{-1})$	0.0075
$I_v(mmHg \cdot s^2 \cdot ml^{-1})$	0

Table 5.3: The main parameters used for all compartments of the lumped parameters model of the whole circulation in the three scenarios considered (R=resistance, C=capacitance, I=inductance, V=volume, E=elastance).

Six whole cycles are simulated to allow the solution to reach the steady state and only the last one was analysed and used to extract the pressure sets for the three scenarios. The time step used to solve the lumped parameters model is $\Delta t = 5 \cdot 10^{-4}$, the same used also for the CFD and reduced FSI simulations, as better detailed in the next section.

The numerical simulations carried out with the circulation lumped parameters model, using the calibrated parameters, allowed to find the three pressure sets used as boundary conditions at the inlets and outlets of the 3D geometry in the numerical simulations of the pulmonary artery haemodynamics. Specifically the right ventricle pressure was extracted and applied at the inlet of the 3D computational domain, while the pressure in the pulmonary artery was extracted and applied at the two outlets. As it will be shown in Figures 5.1 and 5.9, the extracted pressures display firstly the atrial systole, corresponding to the last phase of diastole, then the systolic phase and the beginning of diastole.

Finally, as it will better detailed in Section 5.3 and 5.4, the valve calibration and then the pressure sets applied at the artificial boundaries of the 3D pulmonary artery geometry, allow to obtain physiological values in the 3D numerical simulations of the three scenarios.

5.2. Simulation settings

The linear systems corresponding to the discretisations of the CFD problem for the pre-operative scenario and the reduced FSI problem for the post-operative and follow-up scenarios were solved using the Generalised Minimum Residual (GMRES) algorithm, with a Semi-Implicit Method for Pressure Linked Equations (SIMPLE) preconditioner. The maximum number of iterations was fixed at 1000 and the tolerance was 10^{-10}. As already mentioned, the SUPG-PSPG stabilisation method was used, since the Finite Elements of pressure and velocity were both of the first order. In addition, a backflow stabilisation was applied at the two outlets of the 3D geometry. The numerical time step used was $\Delta t = 5\ 10^{-4}$, with a heartbeat period $T = 0.8\ s$. Two heartbeats were simulated, then the first one was discarded in order to analyse the heartbeat nearer to the steady state, thus the results showed from now on refer to the second heartbeat simulated.

In Table 5.4, the configuration of each scenario, used both for Patient 1 and Patient 2, is synthesised:

	Pre-operative	**Post-operative**	**Follow-up**
Geometry	absent valve	pericardial sleeve virtually inserted, valve included	pericardial sleeve virtually inserted, valve included
3D model	CFD model	reduced FSI model	reduced FSI model
Data used for circulation LPM calibration	6 months after PV replacement	6 months after PV replacement	9 years after PV replacement
BC from	Pre-0D model (absent valve)	Valve-0D model (valve included)	Valve-0D model (valve included)

Table 5.4: Synthesis of both Patient's 1 and Patient's 2 configuration of three scenarios considered for the numerical simulations of the pulmonary artery haemodynamics (LPM=lumped parameters model, PV=pulmonary valve, BC=boundary conditions).

5.3. Results: Pre-operative Scenario

We recall that the boundary conditions are obtained by means of a lumped parameters model of the circulation. In particular, the pressure obtained for the right ventricle is applied at the inlet of the 3D geometry, while the pressure obtained for the pulmonary artery is applied at the two outlets.

Notice that, since the lumped parameters model of the circulation simulates the absence of the pulmonary valve, the pressure in the right ventricle and in the pulmonary artery are characterised by similar values during the cardiac cycle, as shown in Figure 5.1.

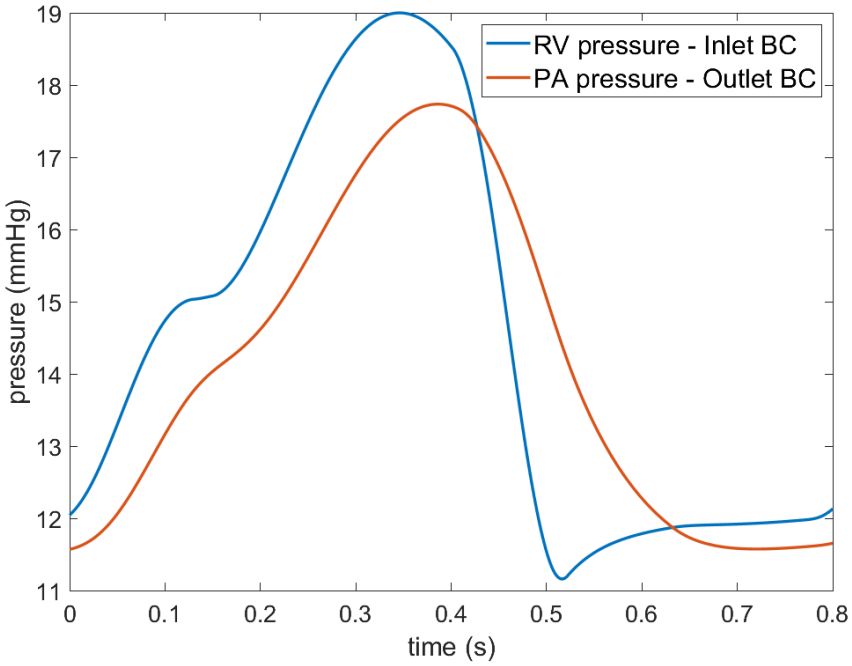

Figure 5.1: The pressures obtained from the numerical simulations with the lumped parameters model of the circulation in the pre-operative scenario (RV=right ventricle, PA=pulmonary artery).

A first quantity that we analyse to verify if the haemodynamics in the pulmonary artery are coherent with the condition of the patients is the flow rate through the inlet of the pulmonary artery. Since the pulmonary valve is absent, during the diastole we expect a backflow to be established. Indeed, as displayed by Figure 5.1, in the diastolic phase the pressure in pulmonary artery tends to be higher than the pressure in the right ventricle, leading to the inversion of the flow; however, in physiological conditions, the pulmonary valve would be closed and prevent the backflow to reach the ventricle. In the absence of the pulmonary valve, instead, we expect to measure a regurgitant volume.

This is clearly shown also by the plots of the flow rate at the inlet of the pulmonary artery; where negative values indicate the ejection and positive values the regurgitation, see Figure 5.2. Indeed, for both patients, it is clear that after the pressure inversion at the time t=0.43 s also a flow rate inversion verifies, specifically from time t=0.5 s.

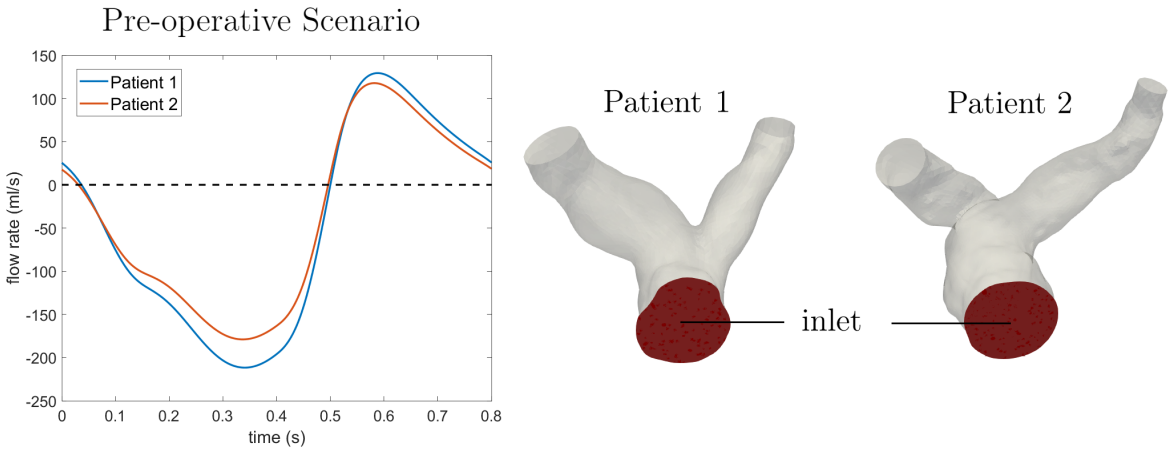

Figure 5.2: The flow rate computed at the inlet of the pulmonary artery in Patient's 1 and Patient's 2 3D simulations of the pre-operatory scenario.

In Table 5.5 we summed up the values of the total ejected volume, the regurgitant volume, which is the volume that returns to the ventricle when the backflow is established, the stroke volume, which is the net volume ejected by the right ventricle and the regurgitant fraction, calculated as $(regurgitant\ volume/total\ volume\ ejected) \cdot 100$.

	Patient 1	**Patient 2**
Total volume ejected (ml)	63.9	54.3
Regurgitant volume (ml)	25.2	22.5
Stroke volume (ml)	38.7	31.8
Regurgitant Fraction	39.4%	41.4%

Table 5.5: Values of total ejected volume, stroke volume and regurgitant volume computed in the 3D simulations of the the pre-operative scenario both for Patient 1 and Patient 2.

From the data calculated in the numerical simulation of this scenario (Table 5.5), we can observe that the regurgitant fraction is approximately 40% both for Patient 1 and Patient 2, meaning that 40% of the blood ejected by the right ventricle during the cardiac cycle returns into the ventricle.

The values found are coherent with the literature review in Section 1.4.3. In particular, a regurgitant fraction of 40% coincides with the condition of pulmonary valve severe insufficiency. As discussed in [33], this value constitutes an indication for pulmonary valve replacement surgery, so we can confirm that the condition simulated is consistent with the patients' one, as they actually needed and received the valve replacement.

At this point we can analyse the three-dimensional haemodynamics in the pulmonary artery, in particular we look at the velocity profile.

The peak velocities in the phase of ejection are reached in the period of time corresponding to the maximum flow rate, so in Figure 5.3 the velocity profiles are shown at the time t=0.36 s, the moment of the maximum ejection, and t=0.58 s, as it is the peak of the regurgitation flow. Then at time t=0.50 s we can visualise the deceleration and an inversion of the fluid velocity direction because of the backflow generation.

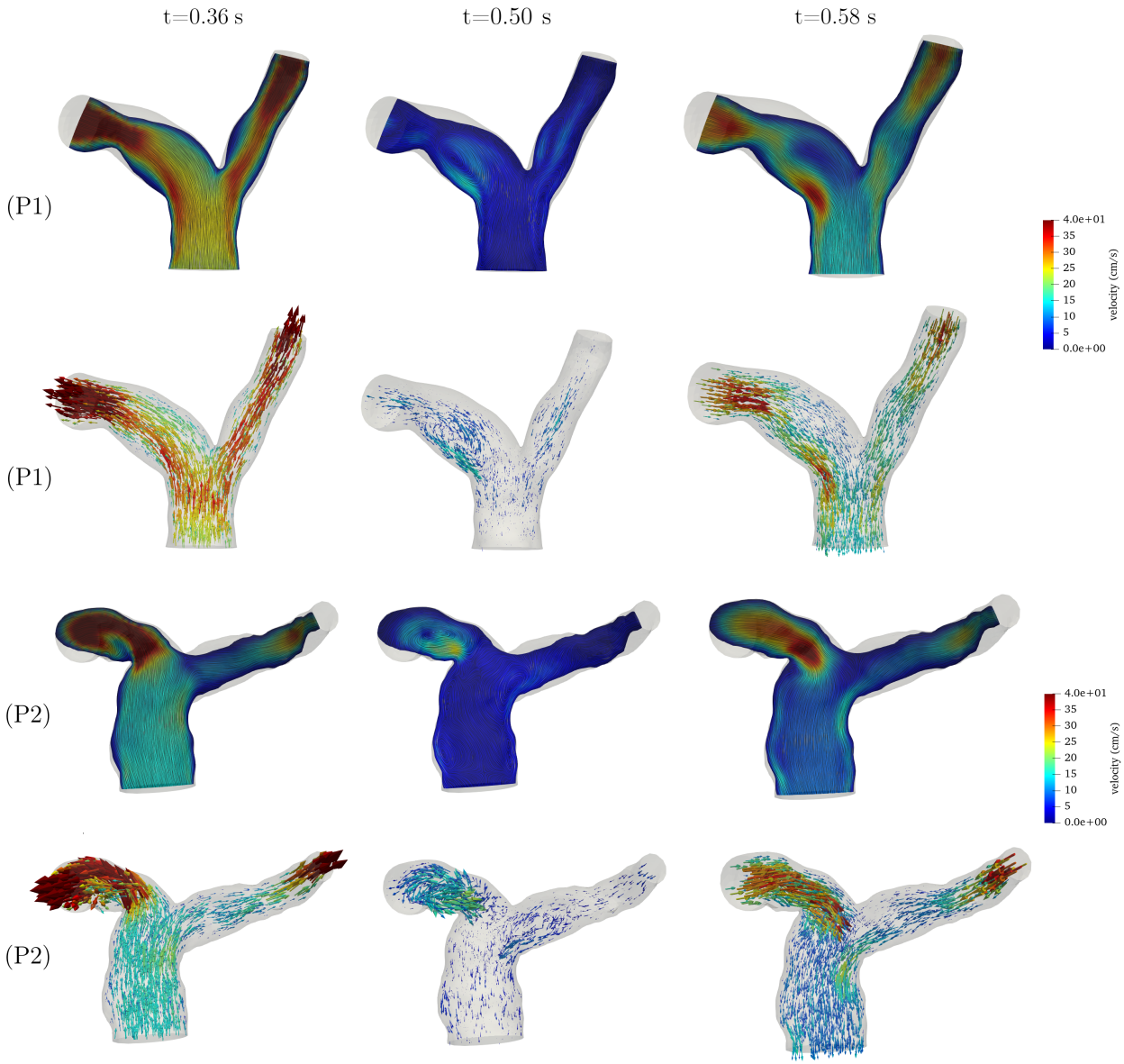

Figure 5.3: The velocity profiles and velocity directions computed by the 3D simulation of Patient's 1 (P1) and Patient's 2 (P2) pre-operative scenario.

From the visualisations of the flow direction (second and fourth row in Figure 5.3), we notice that the generation of a retrograde flow implies also the creation of fluid vortexes. A close-up of this vortexes is provided in Figure 5.4.

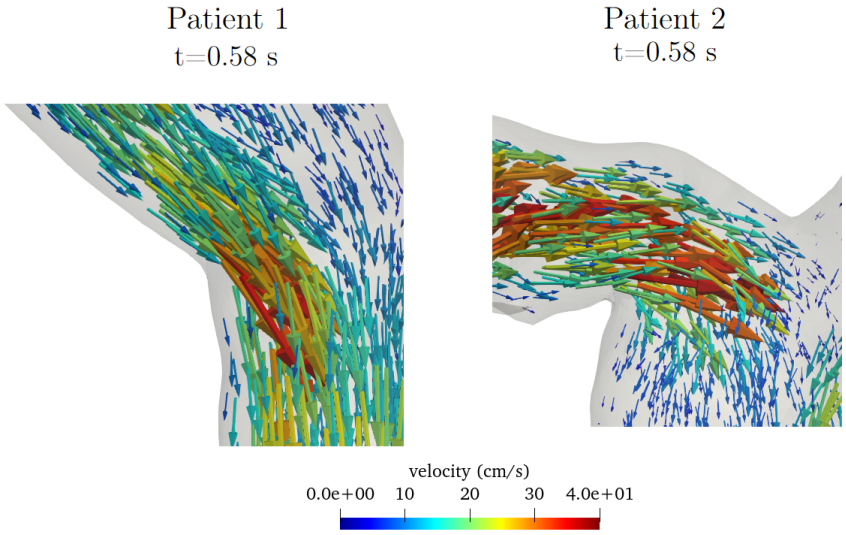

Figure 5.4: A close-up of the vortex formation during the valve closure at time t=0.58 s. The arrows indicate the direction of the velocity calculated in the 3D simulations of the pre-operative scenario

Since the creation of vortexes could lead to the presence of turbulence, the ratio of the turbulent viscosity μ_{sgs} with respect to the blood viscosity μ was analysed. Indeed, as detailed in Section 4.3.2, the Sigma LES turbulence model was used, and so it was added a contribution to the dynamic viscosity of the fluid, namely the turbulent viscosity μ_{sgs}, which allows to model the effects of the turbulence generation. This quantity takes on high values in the regions where there is a turbulent flow and its ratio with the blood viscosity allows to better quantify how much the blood flow is affected by turbulence.

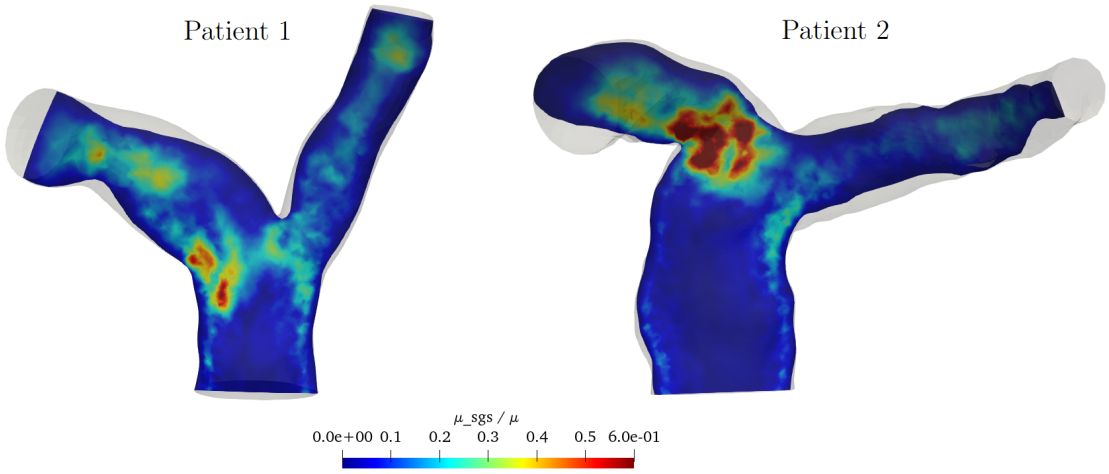

Figure 5.5: A representation of the turbulent viscosity ratio (μ_{sgs}/μ) for both patients at time t=0.58 s, computed in the 3D simulations.

In Figure 5.5, the ratio μ_{sgs}/μ at time t=0.58 s is shown for both patients, indeed this is the moment in which the vortexes are the most evident. Notice that the values of highest turbulent viscosity are the located in the areas in which the vortexes take place. Moreover, we point out that μ_{sgs} is characterised by values comparable with the viscosity of blood; however the ratio μ_{sgs}/μ never becomes equal to 1 during the whole cardiac cycle, giving an indication of the laminar regime conservation. Indeed, for example in [11], the ratio between the physical and turbulent viscosity could reach values of 8 when the scenario characterised by turbulent flow is considered.

Finally, we can analyse the WSS on the artery walls, defined as:

$$WSS = \mu \sqrt{\sum_{j=1}^{2} ((\nabla \boldsymbol{u}\boldsymbol{n}) \cdot \boldsymbol{\tau}_j)^2} \quad on\ \Gamma_{wall}$$

where $\boldsymbol{u}$ is the fluid velocity, $\boldsymbol{n}$ is the normal unit vector and $\boldsymbol{\tau}_j, j = 1, 2$ are the tangential unit vectors.

This is the tangential force per unit area that is applied by the blood flowing on the surface of the pulmonary wall (Γ_{wall}). The WSS magnitude is directly proportional to the velocity gradient near the artery wall, specifically to how fast the velocity increases when moving from a point on the wall to an adjacent one in the normal direction with respect to the wall ($\nabla \boldsymbol{u}\ \boldsymbol{n}$). By multiplying the velocity gradient in the normal direction by the tangential unit vectors ($\boldsymbol{\tau}^{(j)}, j = 1, 2$), with the WSS the tangential viscous forces on the artery wall are quantified [70].

The WSS, being correlated to velocity, is analysed in time t=0.36 s and t=0.58 s, since these are the moments of highest velocity in the artery.

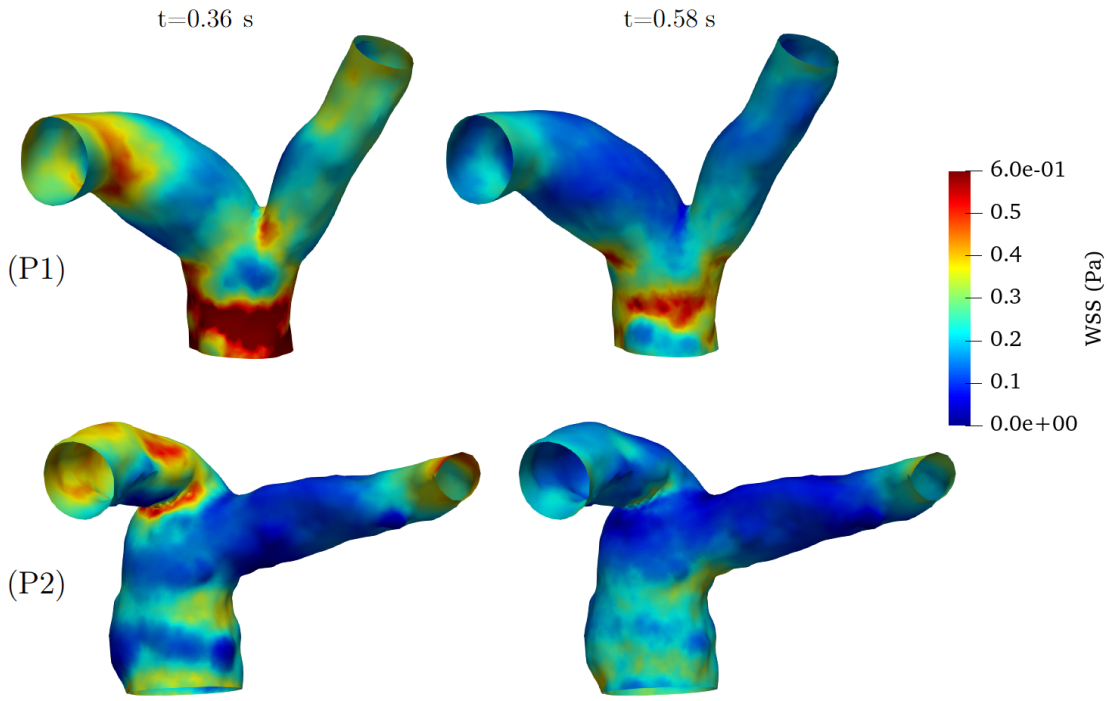

Figure 5.6: The WSS on Patient's 1 (P1) and Patient's 2 (P2) pulmonary artery wall at times t=0.36 s and t=0.58 s.

Figure 5.6 shows the WSS for both in Patient 1 and Patient 2, in particular the points of highest WSS. Notice that the WSS in Patient 1 features higher values than in Patient 2. Moreover, the values of WSS are higher at time t=0.36 s, in accordance with higher values of velocity as shown by Figure 5.3.

The WSS takes on high values especially at the inlet of the artery, meaning that the blood comes in strict contact with the artery walls during the period of ejection. In addition, we can observe also that Patient's 2 geometry tends to influence the pattern of WSS; indeed, the curved shape of one artery branch causes the blood to hit the wall when proceeding towards the outlet.

5.4. Results: Post-operative and Follow-up scenarios

In this section, the results for the post-operative and follow-up scenarios will be analysed. Firstly, the valve calibration is assessed, indeed the parameters governing the reduced

structural model of the valve had to be tuned in order to reproduce correctly the pulmonary valve dynamics. Then, in Section 5.4.2, the results of the 3D simulations in the two scenarios considered will be analysed and discussed.

5.4.1. Valve Calibration for Post-operative and Follow-up scenarios

In the post-operative and follow-up scenarios the presence of the valve was modelled by using the RIIS model. The aim of this section is to provide details about the setting of this model in order to reproduce the results showed in the following section.

Both in the post-operative and follow-up scenarios, the resistance R belonging to the RIIS term in equation (4.4) was set at $R = 10000\ kg/(m \cdot s)$; whereas the half-thickness of the leaflets was fixed at $\varepsilon = 1.8\ mm$. This value was chosen in order to satisfy the condition $\varepsilon > 1.5\ h$, where h is the mesh dimension at the valve level, necessary for the correct solving of $\delta^n_{\varepsilon,h}$, as explained also in Section 4.3.3.

The valve model calibration was carried out by changing mainly 5 parameters:

- Damping coefficient: it is present in Equation (4.9) and is associated with the velocity term of the reduced structural model formulation.
- Stiffness coefficient: it is present in Equation (4.9) and is associated with the elastic forces of the reduced structural model. It influences the opening and closure time since it is associated with the forces opposing to the fluid traction acting on the valve surface.
- Added Curvature: this is added to the term $\widehat{H}$ so that the elastic force acts always in the same verse as it should.
- Density scaling factor: it takes into account the inertial properties of the leaflets and represents the scaling between the leaflets surface density and blood density.
- Coefficient multiplying the surface velocity $\boldsymbol{u}_{\boldsymbol{\Gamma}}$: this coefficient was introduced in [60] as an alternative approach both to the enforcement of the no-slip condition $\boldsymbol{u} = \boldsymbol{u}_{\boldsymbol{\Gamma}}$ and to the quasi-static approximation $\boldsymbol{u}_\Gamma = 0$, which allows reproducing more physiological results by artificially enlarging the obstacle seen by the fluid when approaching the pulmonary valve.

The use of a coefficient multiplying the leaflets surface velocity $\boldsymbol{u}_{\boldsymbol{\Gamma}}$ was chosen since in [60] was observed that this approach led to valve closing a opening times which are closer to what is found in literature.

Indeed, the 5 parameters governing the valve model were tuned in order obtain timings of opening and closure of the pulmonary valve consistent with the values found in literature.

The calibration was performed by running various simulations both for the post-operative and follow-up scenarios using Patient's 1 computational domain. Then, making the assumption that the model describes the same valve implanted to both the patients, the values found for Patient 1 were applied also to Patient's 2 numerical simulations.

Finally, it was made the assumption that the valve does not change its properties from the post-operative to the follow-up scenario. The parameter values used for the numerical simulations of the post-operative and follow-up scenarios are summed up in Table 5.6.

Parameters	**Post-operative/Follow-up scenarios**
Damping coefficient (s^{-1})	0.28
Stiffness coefficient (s^{-2})	0.13
Added Curvature (m^{-1})	0.24
Density scaling factor	- 0.1
Coefficient multiplying the surface velocity $\boldsymbol{u_\Gamma}$	0.075

Table 5.6: Calibrated parameters for the reduced structural valve model in the post-operative and follow-up scenarios.

As already discussed in Section 4.2.4, the solution of the reduced structural problem allows to find the opening coefficient c. Its evolution in time (Figure 5.8) allows to quantify the rapid opening, opening and closing times both for the post-operative and follow-up scenarios. In particular, the value of 1 indicates that the valve is open and a value of 0 that it is closed. To better display the valve dynamics reproduced in this study, in figure 5.7, instead, the 3D valve is shown an example of the valve opening reproduced by the reduced FSI model in Patient's 2 follow-up scenario.

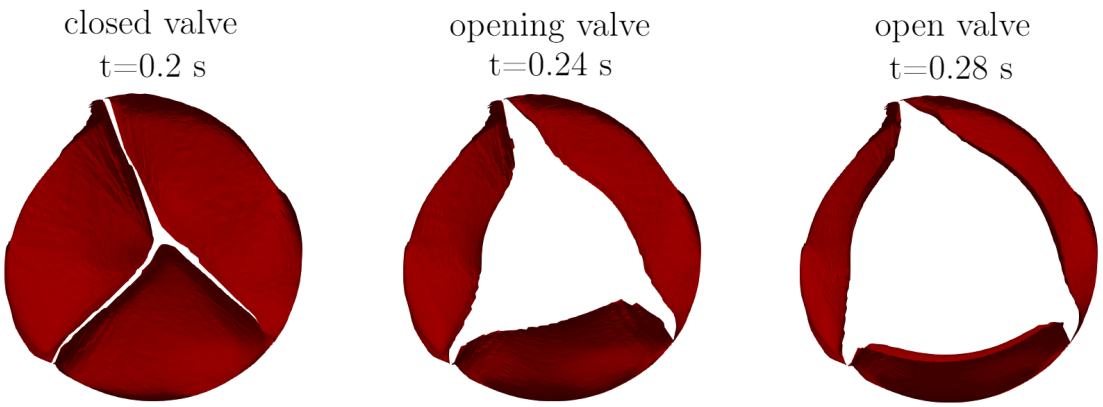

Figure 5.7: The opening dynamics of the pulmonary valve reproduced by the reduced FSI model in Patient's 2 follow-up scenario.

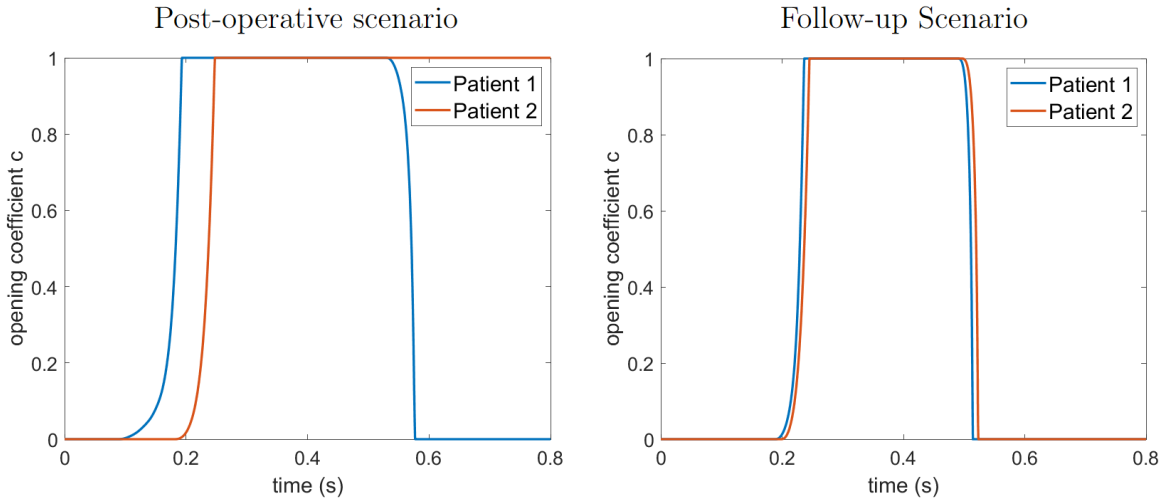

Figure 5.8: The evolution in time of the opening coefficient, solution of the reduced structural model of the valve, in the post-operative and follow-up scenarios found by the solution of the linear system describing the reduced FSI problem.

From the plot of Patient's 2 opening coefficient in the post-operative scenario (Figure 5.8, left), we can observe that the pulmonary valve dynamics are not reproduced correctly in this case. Indeed, we managed to reproduce only the opening of the valve, however, after the opening phase the valve remains open for the rest of the cardiac cycle.

This could be the consequence of the many factors; for example, we have to take into account that the boundary conditions, applied to the 3D model of Patient 2, were found using a lumped parameters model of the circulation tailored on the clinical data of Patient

1. The post-operative scenario is still characterised by pathological haemodynamics, as suggested by the ejection fraction of 35% in Patient's 1 clinical data, and on top of this we add the presence of the stented valve, which represents an element of disruption with respect to the already established blood flow patterns. The haemodynamics have not yet normalised after pulmonary valve replacement, so we could hypothesise that a correct reproduction of this condition requires the use of the patient's clinical data, in other words we were not able to generalise Patient's 1 data also to Patient's 2 geometry.

Another possible explanation resides in the way the valve was calibrated. The lack of a conclusive result for Patient's 2 post-operative scenario could be a hint to the fact that even if the valve implanted is the same, in this scenario it acts differently when different geometries are considered; thus it would be needed a different calibration carried out independently for Patient 2.

The results for the follow-up scenario are more convincing both in the case of Patient 1 and Patient 2, as the valve dynamics seem to be close to the physiological behaviour.

In Table 5.7 we make a comparison between the timings of opening and closing of the valve found using the calibrated parameters in the 3D simulations of the post-operative and follow-up scenarios and reference values for the timings of valve dynamics found in literature. We point out, however, that the reference values are extracted from studies characterising the behaviour of the aortic valve, since there is very few information about the pulmonary valve dynamics in literature. Finally, a distinction is made between *rapid opening time*, which is the period of time when the valve is opening, and *opening time*, identifying the period of time in which the valve remains open.

	Rapid Opening time (ms)	**Opening time** (ms)	**Closing time** (ms)
Post (P1)	104.5	336	47
Post (P2)	66	734	-
Follow-up (P1)	47	254	23
Follow-up (P2)	46.5	252	25.5
Stented valve [86]	31 ± 7	290 ± 25	30 ± 8
Natural Valve [86]	45 ± 7	235 ± 26	42 ± 9
Natural valve [43]	76 ± 30	-	42 ± 16

Table 5.7: Computed timings of opening and closing of the simulated pulmonary valve dynamics both for the Post-operative scenario (Post) and Follow-up scenario (Follow-up) for Patient 1 (P1) and Patient 2 (P2). In the last three rows the timings of aortic valve opening and closing found in literature are reported.

As expected, the values of opening and closing times pertaining to the follow-up scenario are the most close to the ones found in literature for the natural healthy aortic valve (Table 5.7). Indeed, in this scenario the haemodynamics are ideally close to physiological ones.

Considering the values found for Patient's 1 post-operative scenario, we immediately notice that the rapid opening time (104.5 ms) is longer with respect to the follow-up scenario (47 ms), however the valve behaviour in the opening phase remains within the range of the values indicated by the literature. Also in the case of the opening time we find that in the post-operative scenario the valve remain open approximately 80 ms more than in the follow-up scenario, getting more close to the behaviour of the stented valve than the natural valve.

As for Patient's 2 results, in the post-operative scenario, only the rapid opening time is taken into account for this analysis; indeed, the high value of opening time is explained by the fact that the closure of the valve was not modelled. Considering, however, the rapid opening time we can observe that the model actually simulated a value within the range considered physiological by [43].

All in all, the differences in the timings between the follow-up and the post-operative scenarios could be linked to the fact that, in this last scenario, we are trying to reproduce a condition of transition from a pathological state to a physiological one. The different behaviour of the valve could also be related to the valve calibration; indeed, we assumed that the valve characteristics were the same both in the post-operative and follow-up scenarios, however it is clear from the values analysed that the valve behaves differently in the two scenarios.

Finally, we have to take into account that we are referring, due to lack of available data, to values associated with the aortic valve dynamics. These however are defined by values of pressure and flow rate that are very distant from the ones that we find in pulmonary valve haemodynamics. So, more specific reference values, even measured on the patient analysed, would be needed to give a definitive judgement of the capabilities of the model to reproduce the actual valve dynamics. Given all these considerations, except for the Patient's 2 post-operative scenario, we look at the values found as acceptable.

5.4.2. Results and global discussion for Post-operative and Follow-up scenarios

In the post-operative and follow-up scenarios, the presence of the valve is taken into account, both thanks to the use of a reduced FSI approach in the 3D model and to the boundary conditions, since the Valve-0D model of the whole circulation (where the diode-like pulmonary valve is accounted for) was used to find them. The pressure sets applied as boundary conditions for these scenarios are shown in Figure 5.9. In particular, we can observe that the pressure jump between the right ventricle and pulmonary artery pressure is higher in the follow-up scenario; moreover in this case the pressures found are coherent with the physiological pressures of a healthy adult [47, 51].

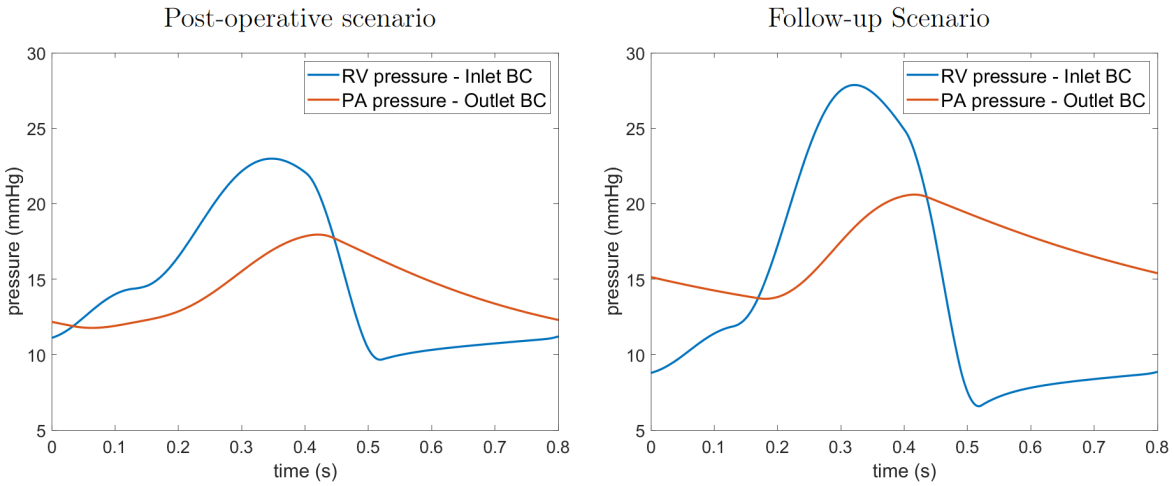

Figure 5.9: The pressures obtained from the numerical simulations with the lumped parameters model of the circulation in the post-operative and follow-up scenarios (RV=right ventricle, PA=pulmonary artery).

Accordingly to what we have done for the pre-operative scenario, also in the post-operative and follow-up scenarios we can analyse the blood flow rate at the inlet of the pulmonary artery, found from the solving of the reduced FSI problem. Indeed, we can verify that in these scenarios, the simulation of the pulmonary valve implantation actually reduces the regurgitant fraction.

The plot of the blood flow rate calculated at the inlet of the computational domain is shown in Figure 5.10; we can immediately notice that in Patient's 2 post-operative scenario, even if the flow dynamics are initially mimicked appropriately, the failed closure of the valve allows the establishment of a consistent regurgitation (positive values of the plot in Figure 5.10, left) which is clearly higher than the one registered for Patient 1. Whereas

in the follow-up scenario, the 3D simulation of the pulmonary artery haemodynamics provides convincing results for both the patients considered.

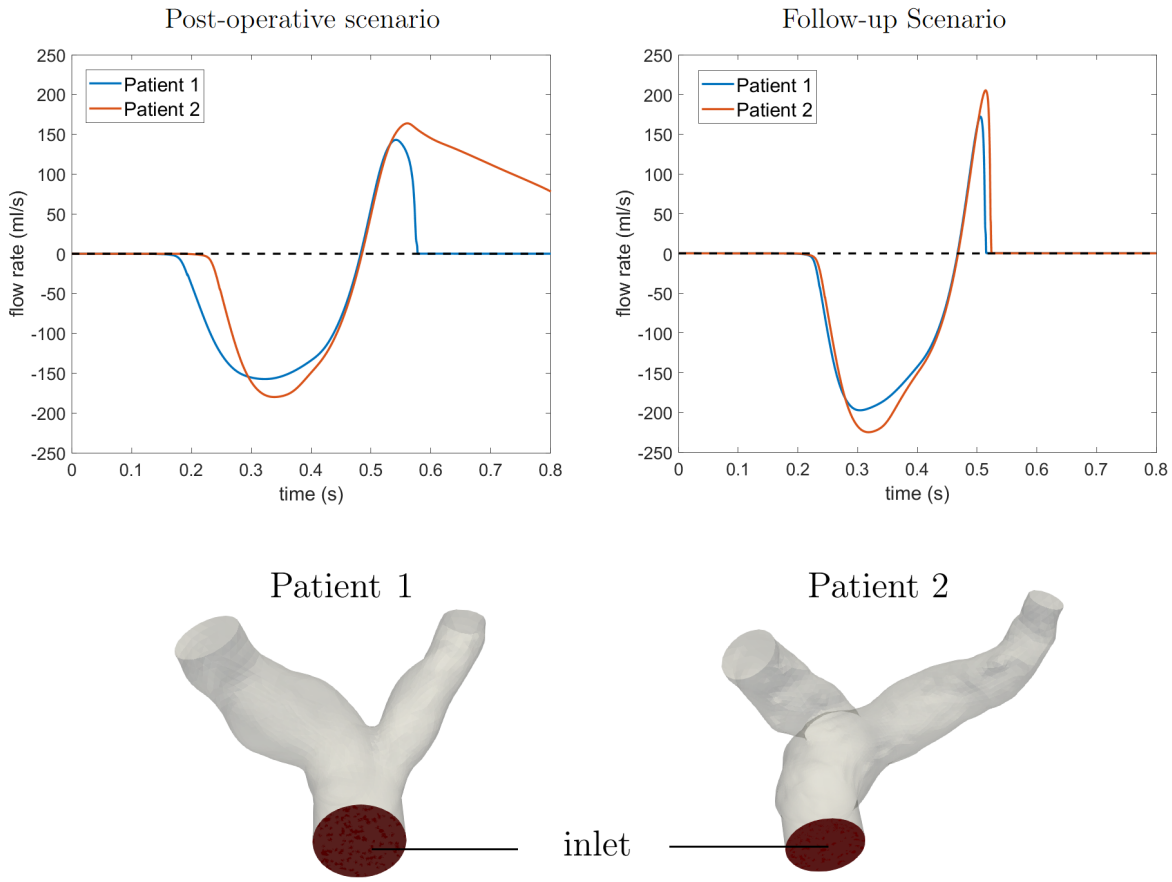

Figure 5.10: The flow rate computed at the inlet of Patient's 1 and Patient's 2 3D simulations of both the post-operative and follow-up scenarios.

In Table 5.8 the values of total ejected volume, regurgitant volume and stroke volume computed by our 3D simulations are summarised.

	Post-operative	**Post-operative**	**Follow-up**	**Follow-up**
	Patient 1	Patient 2	Patient 1	Patient 2
Total volume ejected (ml)	34.1	31.2	33.3	35.3
Regurgitant volume (ml)	9.1	36.4	4.7	6.6
Stroke volume (ml)	25.0	- 5.2	28.6	28.7
Regurgitant Fraction (ml)	26.6 %	116%	14.1%	18.6%

Table 5.8: Values of total ejected volume, stroke volume and regurgitant volume both for Patient 1 and Patient 2 computed in the 3D simulations of the post-operative and follow-up scenarios.

The values in Table 5.8, confirm what previously observed about Patient's 2 results for the post operative scenario. Indeed, the results of this case are characterised by a regurgitant volume even higher than the total ejected volume, meaning that all the ejected volume plus the value indicated as stroke volume (-5.2 ml) return into the right ventricle during diastole. This is quantified also by the regurgitant fraction which is 116% for Patient's 2 post-operative scenario.

Furthermore, we can observe that the stroke volume in the post-operative and follow-up scenarios is lower than what found for the pre-operative scenario (Table 5.5). This is not what we would expect after the pulmonary valve replacement; we could hypothesise that in reality the pressure gradient between the right ventricle and the pulmonary valve is in fact higher than the one estimated by the lumped parameters model of the circulation. Indeed, the stroke volume found for the post-operative and follow-up scenarios, which would have to be close to the values of a healthy adult, are actually lower than what found in literature.

In particular, considering the follow-up scenario, we notice that the stroke volume is approximately 28 ml both for Patient 1 and Patient 2 (adult males) whereas in [56] the reported values for an adult male are approximately in a range between 89 ml and 123 ml. However, considering only Patient 1, whose clinical data was available, we observe that his right ventricle end-diastolic volume was 110 ml 9 years after the pulmonary valve replacement; this value is below the average for the healthy adult male which, as reported in the same study [56], is in a range between 138 ml and 188 ml. So we can conclude that, even if the stroke volume is surely underestimated, its value would still be below average and so possibly the value found with the simulations is not so far from the actual Patient's 1 stroke volume.

Further analysing the values of stroke volume, we can observe for Patient 1 that be-

tween the post-operative and follow-up scenario there is an improvement in the stroke volume, due to a reduced regurgitant volume; this can be interpreted as indication that the model actually reproduces an improvement in the haemodynamics after pulmonary valve replacement as the haemodynamics reach a steady state years after the surgery.

Finally, we can observe that the regurgitant fraction is highly improved with respect to the pre-operative scenario. Specifically, in the post-operative scenario Patient 1 shows a regurgitant fraction of 26.4% with respect to the 40% of the pre-operative scenario. In the follow-up scenario, the improvement is even more, indeed Patient's 1 and Patient's 2 regurgitant fraction is 14.1% and 18.7%, respectively. Moreover, the presence of a small residual regurgitation is consistent with the report of the surgeon after the pulmonary valve replacement.

Having critically assessed the validity of the results found using the numerical model, we can proceed to analyse the 3D hemodynamic quantities both for the post-operative and follow-up scenarios.

In the following section, we analyse more specifically the 3D hemodynamic quantities for the post-operative and follow-up scenarios, separately.

5.4.3. Results and specific analyses for Post-operative and Follow-up scenarios

Post-operative Scenario. For the Patient's 1 post-operative scenario we analyse the instants t=0.34 s, t=0.56 s and t=0.58 s (Figure 5.11), which allow to visualise the maximum ejection and regurgitation velocities and also the haemodynamics when the valve has just closed.

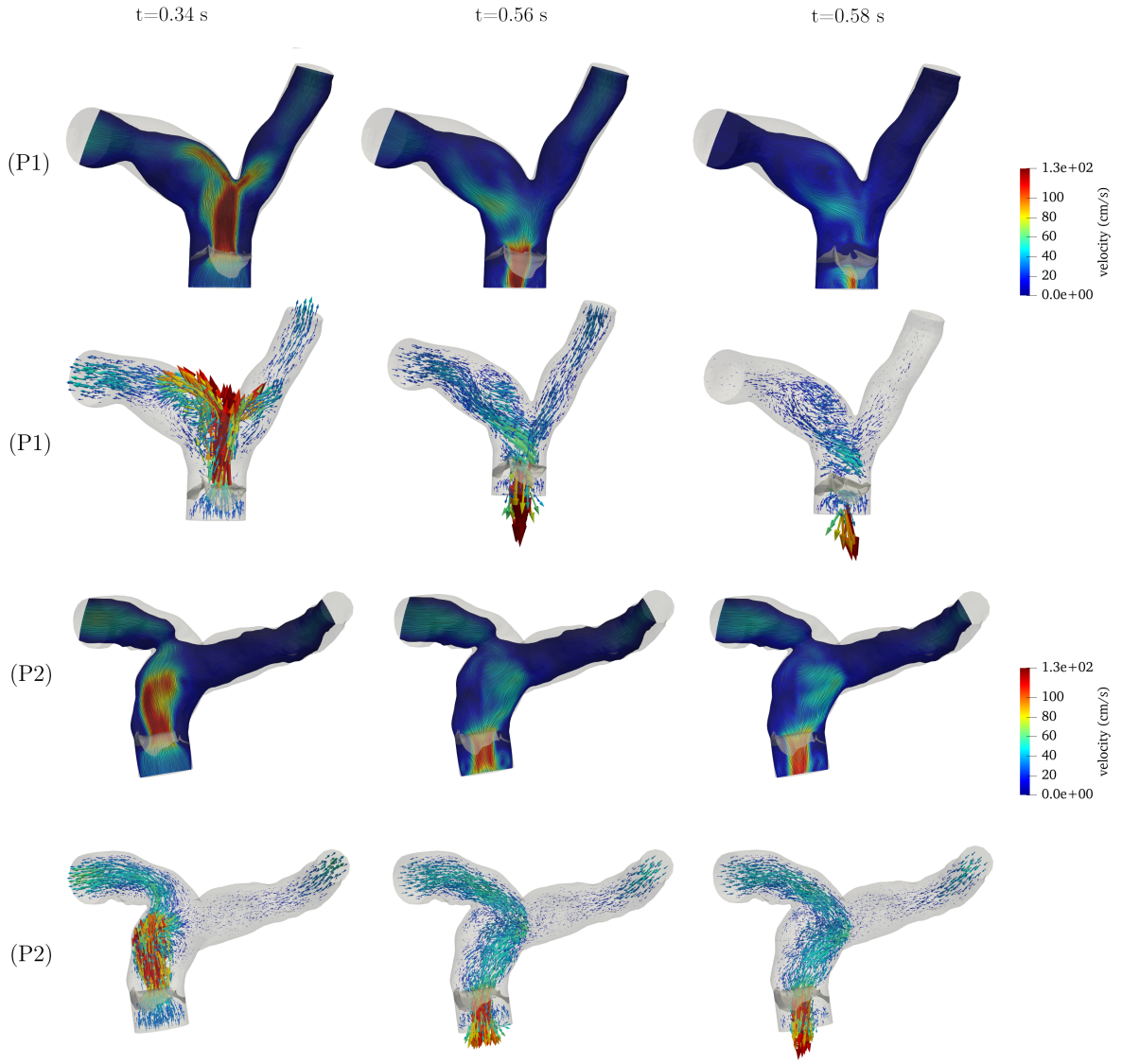

Figure 5.11: The velocity profiles computed in the 3D simulations of Patient's 1 (P1) and Patient's 2 (P2) post-operative scenario.

From the visualisation of the velocity profiles we can observe that as the valve opens (t=0.34 s) Patient 1 and Patient 2 are characterised by a similar velocity profile and values of velocity. However, in the instant t=0.58 s, we can appreciate the different behaviours in the two patients. Indeed, in Patient 1 the valve closes and so the regurgitant flow is limited by the obstacle imposed by the valve presence. Instead, in Patient's 2 results, the valve remains open allowing the fluid from the two branches of the pulmonary artery to return towards the inlet.

Moreover, we can observe that the presence of the valve determines the development of

higher velocities with respect to the pre-operative case (Figure 5.3); this can be explained by the higher pressure jump across the valve together with the fact that the valve presence implies a narrowing of the orifice with respect to the pre-operative geometry. Finally, we can notice that both during the ejection (i.e. t=0.34 s) and when the regurgitant flow is established (e.g. t=0.58 s), some vortexes are generated, as shown in Figure 5.12.

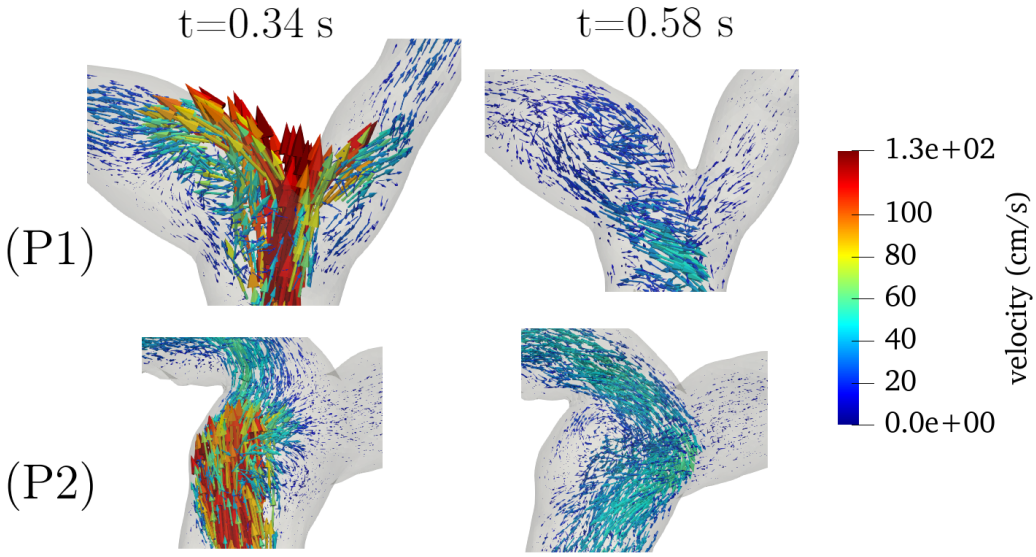

Figure 5.12: A close-up on the vortexes generated at times t=0.34 s and t=0.58 s both for Patient 1 (P1) and Patient 2 (P2) in the post-operative scenario. The arrows indicate the direction of the velocity calculated in the 3D simulations of this scenario

We can further investigate the creation of the vortexes by analysing the values of turbulent viscosity in proximity of the vortexes formation and in the points where we have the highest velocity, to verify if there is an indication of turbulence presence.

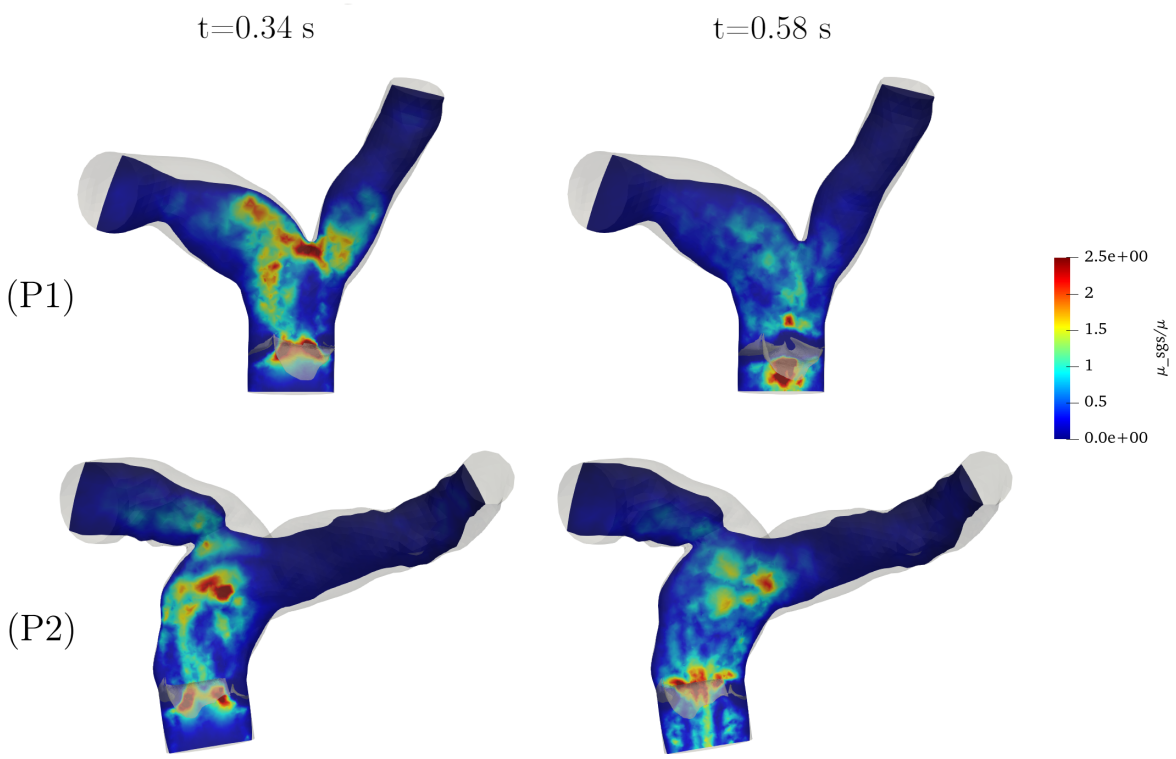

Figure 5.13: Values of viscosity μ_{sgs}/μ computed in the 3D simulations of Patient's 1 (P1) and Patient's 2 (P2) post-operative scenario at times t=0.34 s and t=0.58 s.

In Figure 5.13, the values of the ratio between the turbulent viscosity and the physical viscosity (μ_{sgs}/μ) at times t= 0.34 s and t= 0.58 s are shown. We can observe that in this case the value of turbulent viscosity is not only comparable to the value of physical blood viscosity ($\mu = 3.5 \cdot 10^{-3} Pa \cdot s$), but it gets also higher, especially in the two instants analysed. Specifically, the regions which are affected the most by turbulence are, as showed by Figure 5.13, the regions in which the jet of fluid impacts the artery wall at time t=0.34 s and the region of the valve at t=0.58, since the the fluid flows at high velocity towards the valve surface.

The ratio μ_{sgs}/μ, in the post-operative scenario gets equal to 2.5 both at time t=0.34 s and t=0.58 s, meaning that potentially we could have a transition to the turbulent regime. However, these values are not sustained over the whole cardiac cycle, but only in few instants; so we could say that the fluid has turbulent characteristics when the maximum blood flow velocity is reached but a turbulent regime is not established.

Finally, in Figure 5.11 we can observe that, due the positioning of the prosthetic pulmonary valve and the patients' geometry, in Patient 1 a jet of fluid at high velocity is

directed towards the artery wall at the bifurcation level, whereas in Patient 2 the jet of fluid impacts the artery wall on the main branch. The fluid, impacting on the artery, leads to high values of WSS, as shown in Figure 5.14 which displays the WSS in the instant of maximum velocity of the fluid (t=0.34 s).

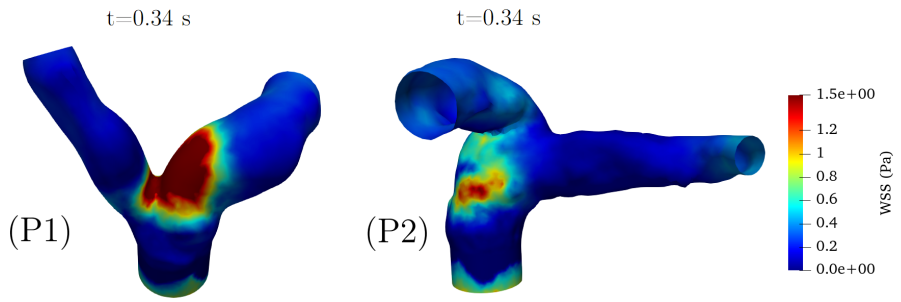

Figure 5.14: The wall shear stress computed in the 3D simulation of Patient's 1 (P1) and Patient's 2 (P2) post-operative scenario at time t=0.34 s.

Follow-up Scenario. Let us consider now the results of the Follow-up Scenario, available both for Patient 1 and Patient 2.

The velocities at the main instants of interest are summed up in Figure 5.15.

In particular, notice that during the opening of the valve (t=0.34 s), the jet of blood flow coming from the ventricle impacts the artery wall in a very evident way both in Patient 1 and Patient 2. Specifically, in Patient 1 the location corresponds to the one already observed in the post-operative scenario. In Patient 2, it is even more clear that the orientation of the stent influences the haemodynamics in the pulmonary artery by determining a higher flow rate towards the left branch in the image rather than the right one. Moreover, we expect that in the point of impact with the wall, high values of WSS are generated, as shown by Figure 5.16.

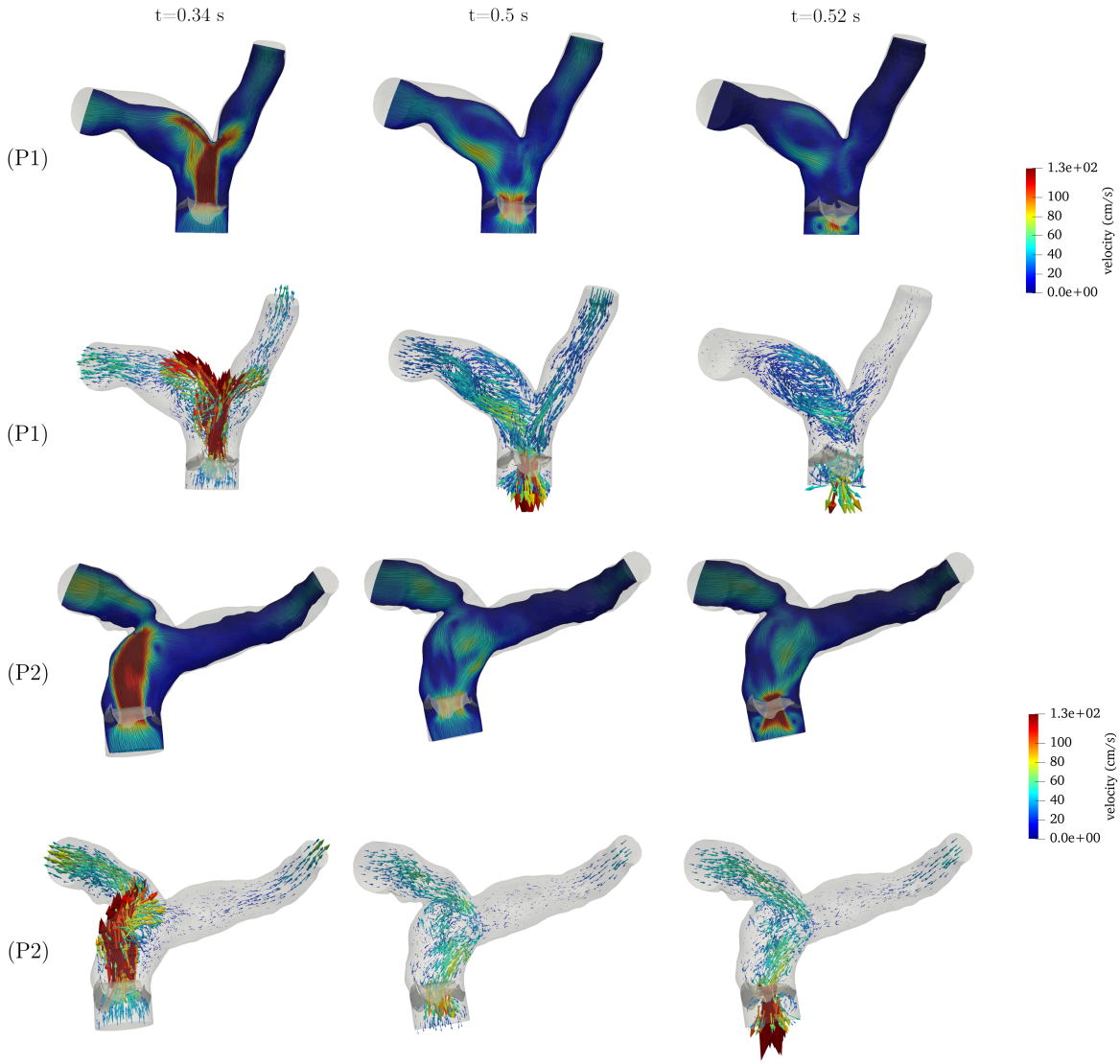

Figure 5.15: Velocity profiles computed in the 3D simulations of Patient's 1 (P1) and Patient's 2 (P2) follow-up scenarios.

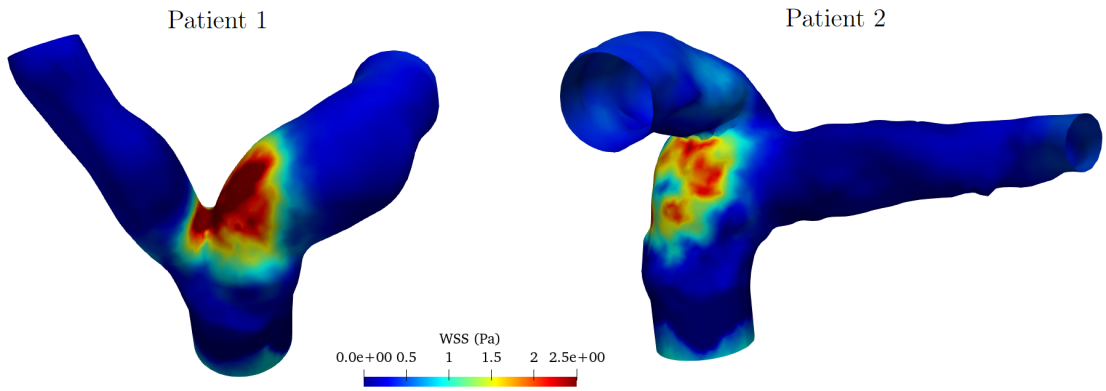

Figure 5.16: The WSS computed in the 3D simulations of Patient's 1 and Patient's 2 follow-up scenario at time t=0.34 s (instant of peak velocity).

Additionally, in Figure 5.11, during the closing of the valve, at times t=0.50 s and t=0.52 s, we can notice once again the generation of a backflow, which assumes high velocities due to the narrowing of the valve orifice in the closure phase. This is consistent with what was already observed from the flow rate plot in Figure 5.10. Moreover, also in this scenario, we have the generation of flow vortexes, specifically at time t=0.52 s, as shown also by figure 5.17.

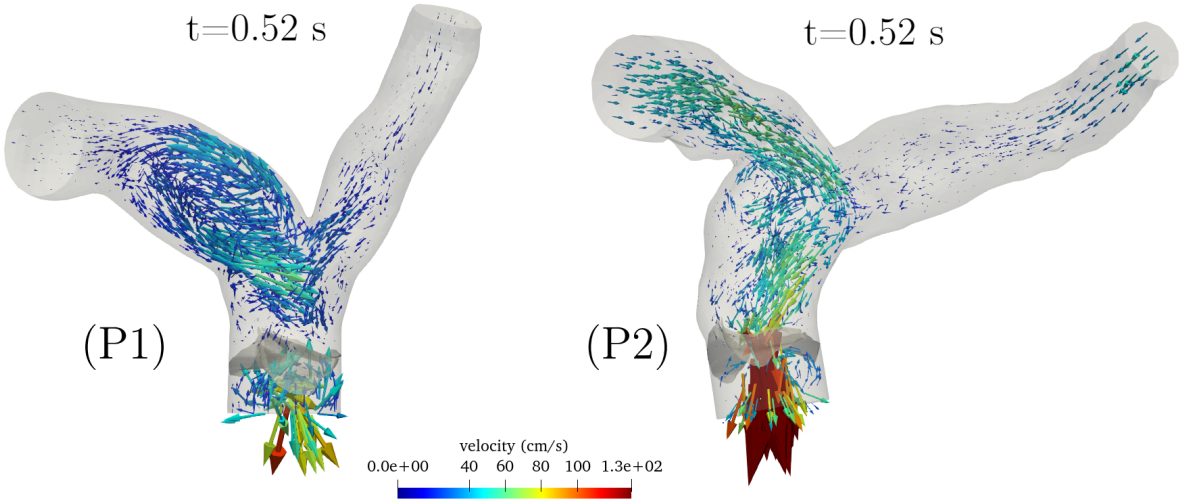

Figure 5.17: A close-up on the generation of vortexes at time t=0.52 s in Patient's 1 (P1) and Patient's 2 (P2) follow-up scenario. The arrows indicate the direction of the fluid velocity calculated in the 3D simulations.

Similarly to the previous scenarios, the characteristics of the flow in these instants can

be further analysed using the turbulent viscosity μ_{sgs} and the ratio μ_{sgs}/μ. In figure 5.18, the values of viscosity ratio found are even higher if compared to the post-operative scenario. This gives an indication of the presence of turbulence when as the valve is closing, especially if we consider that the ratio μ_{sgs}/μ even reaches the value of 4. However, we must consider also that this values are not present during all the cardiac cycles but only during the 20 ms in which the valve is closing, meaning that although turbulence is present, the presence of the valve does not alter excessively the laminar flow of blood.

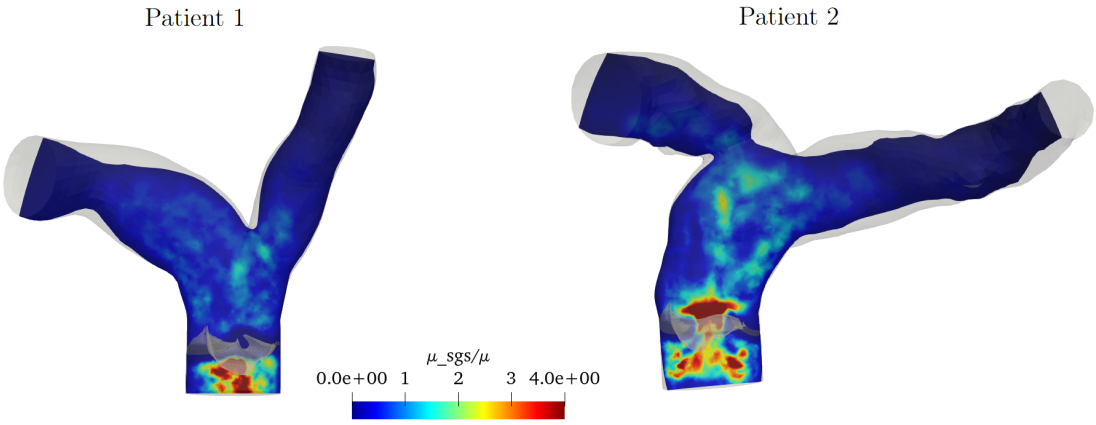

Figure 5.18: The values of the viscosity ratio μ_{sgs}/μ computed at time t=0.52 s in the 3D simulations of Patient's 1 and Patient's 2 follow-up scenario.

5.5. Comparison of the pre-operative, post-operative and follow-up scenarios

As already mentioned in the previous sections, the pre-opeative scenario, simulating the absence of the valve, is characterised by many differences if compared to the simulations of the prosthetic valve presence carried out in the post-operative and follow-up scenarios.

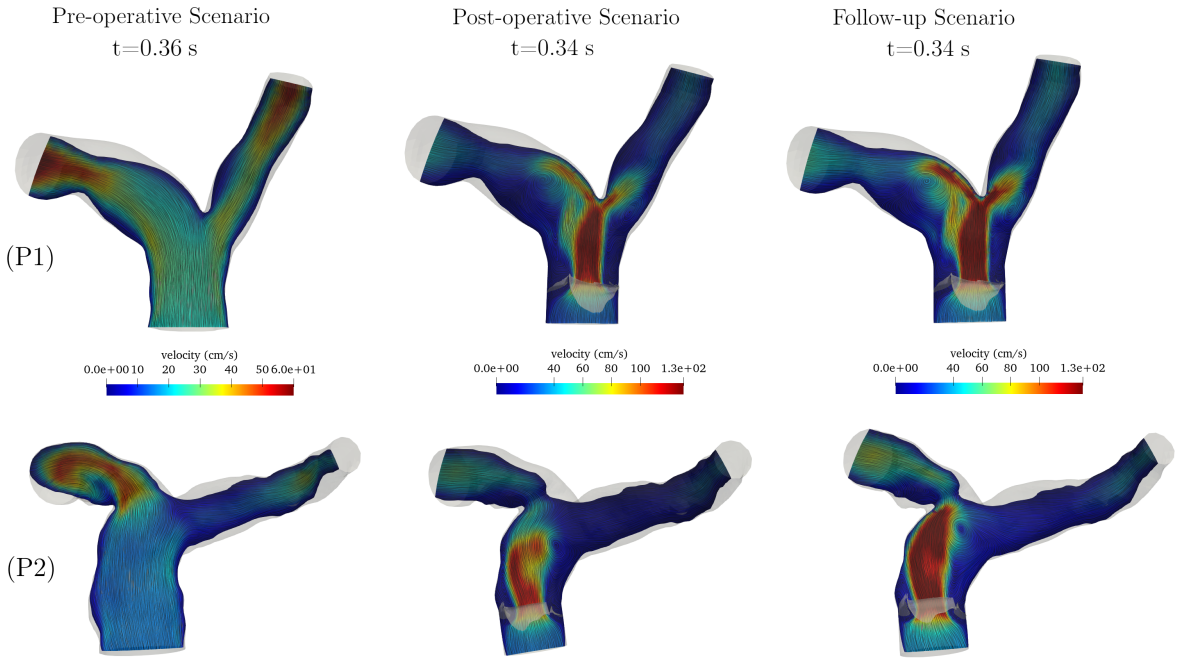

Figure 5.19: Patient's 1 (P1) and Patient's 2 (P2) velocity profiles found in the 3D simulations at the instant of maximum ejection in the pre-operative, post-operative and follow-up scenarios.

Firstly, we refer to the velocities developed during the cardiac cycles. As we can observe by analysing the three scenarios, the velocities reached in the post-operative and follow-up scenarios are much higher than the velocities in the pre-operative case. As an example, we report the velocities profile in the moment of maximum ejection for each scenario (Figure 5.19). This is consistent with the presence of the valve which causes a narrowing in the space available for the flow to pass, in addition to the higher pressures applied at the artificial boundaries.

The plot of the pressure over the 3D geometry (Figure 5.20), can be another efficient method to visualise the change brought by the valve presence, especially when the valve is closed. Indeed, in this moment we can observe that in the pre-operative case the pressure has almost the same values in all the geometry; while in the post-operative and follow up scenario, the pressure gradient develops mostly in the proximity of the leaflets surface, demonstrating the capacity of the model to simulate the valve as an obstacle to blood flow. Moreover, even if in Patient's 2 post-operative scenario the solution of the 3D simulation does not reproduce the valve closure, we can still appreciate the development of the pressure gradient mostly in the valve proximity. However, with respect to Patient's 1 post-operative scenario, the gradient displayed is lower.

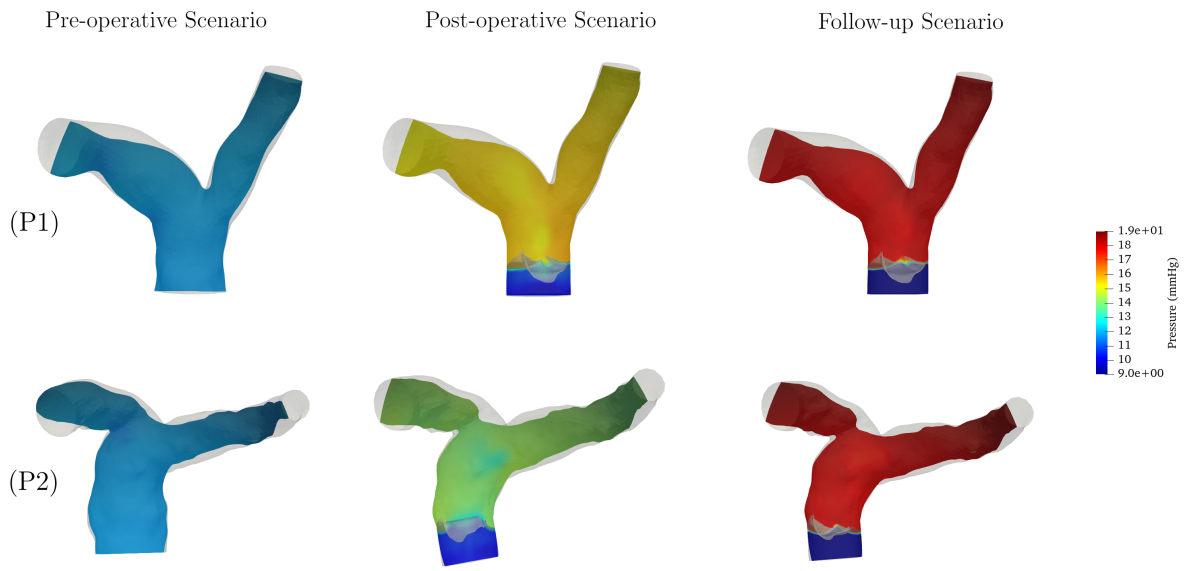

Figure 5.20: Patient's 1 (P1) and Patient's 2 (P2) pressure plots in the 3D simulated pre-operative, post-operative and follow-up scenarios at t=0.58 s.

Another parameter that allows visualising the effect of the valve insertion is the WSS at the instant of maximum blood velocity; in particular we can see how the insertion of the valve changes the pattern of WSS. In the pre-operative case we can see that the WSS is characterised by lower values and the same values are diffused throughout the geometry inlet. The presence of the valve, in the post-operative and follow-up scenarios, determines instead the generation of a jet of blood which hits the wall of the artery mainly at the level of the bifurcation in Patient 1 and the left branch of the artery in Patient 2 (Figure 5.21). Thus, the valve implantation prevents having a generalised presence of viscous fluid forces along the inlet and the walls of the pulmonary artery, differently from the pre-operative scenario.

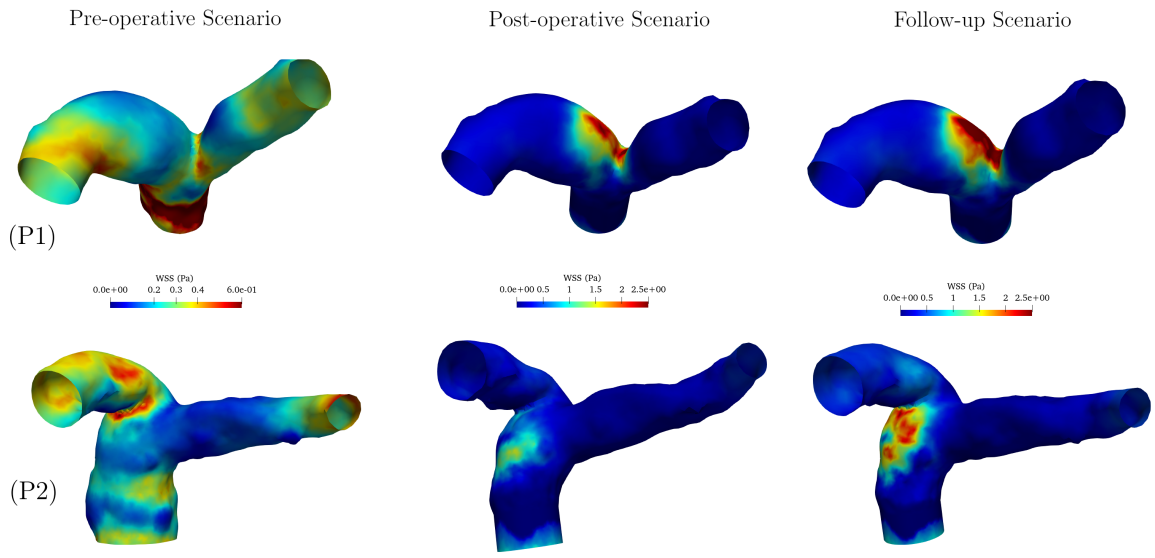

Figure 5.21: The WSS computed in Patient's 1 (P1) and Patient's 2 (P2) 3D simulations of the pre-operative, post-operative and follow-up scenarios at t=0.34 s.

Finally, a last analysis which can be performed is to verify if the presence of the valve changes the distribution of the volume of blood going into the two branches after the bifurcation.

This could be interesting particularly in the case of Patient 2. Indeed, the geometry in Patient's 2 post-operative and follow-up scenarios is characterised by the valve having a particular orientation towards the left branch of the pulmonary artery after the bifurcation.

In Table 5.9, the percentage derived by comparing the stroke volume ejected at each outlet with stroke volume at the inlet are summarised. As we can see from the values reported the presence of the valve does not change significantly the flow distribution between the two main branches of the pulmonary artery.

	Left Branch	Right Branch
Patient 1		
Pre-operative scenario	33.8 %	66.2 %
Post-operative scenario	30.4 %	69, 6 %
Follow-up scenario	27.2 %	72.8 %
Patient 2		
Pre-operative scenario	74.8 %	25.2%
Post-operative scenario	69.2 %	30.8 %
Follow-up scenario	77.3 %	22.7 %

Table 5.9: The percentages of the blood volume distribution between the two branches of the pulmonary artery after the bifurcation. The values are calculated starting from the quantities computed in the 3D simulations of Patient 1 and Patient 2 in all three scenarios considered.

6 | Final remarks, limitations and future developments

In this thesis, we were able to simulate the pulmonary artery haemodynamics before and after pulmonary valve replacement.

In particular, the main outcomes of this thesis are reviewed:

- It was demonstrated that, using the patient's clinical data, it is possible to obtain patient-specific boundary conditions for the numerical simulation of the pulmonary artery hemodynamics. Specifically, the patient's data was used in the calibration of a lumped parameters model of the whole circulation.
- The pre-operative scenario was successfully reproduced, this allowed having an approximated description of the patients' hemodynamics before the pulmonary valve replacement, giving also a reference to be compared with the post-operative hemodynamics.
- The reproduction of the pulmonary valve dynamics proved successful in two different scenarios, i.e. the post-operative and follow-up scenarios (6 months and 9 years after the pulmonary valve replacement, respectively). This allowed to demonstrate that there is a relevant change in the hemodynamics before and after pulmonary valve replacement. Specifically, we were able to provide an analysis of haemodynamic quantities such as velocity, pressure, WSS.
- The use of a patient-specific geometry in all three scenarios allowed to demonstrate the importance of using a patient-specific model. Above all, this can be noticed in the velocity profile plots and WSS plots, in which is clear that the insertion of the valve influences the direction of blood flow after the pulmonary valve replacement.

We can also identify some limitations of this work:

- The failed calibration of the valve model in Patient's 2 post-operative scenario, allows to point out the limitation represented by the lack of clinical data.The availabil-

ity of Patient's 2 clinical data would have allowed to carry out a separate calibration of the lumped parameters model of the circulation and so to extract patient-specific boundary condition also for Patient 2, instead of generalising to both patients the data obtained for Patient's 1 geometry.

- The absence of clinical measurements for the stroke volume, regurgitant volume and pulmonary valve opening and closing times, prevented from determining surely if the model is actually reproducing the behaviour of the valve implanted to the patients.
- The models used for the reproduction of pulmonary artery hemodynamics neglect the deformation of the pulmonary artery during the cardiac cycle limiting the completeness of the model.
- The valve and stent geometry used was not recontructed from the CT acquisitions of the patients analysed, meaning that the patient-specificity of the model is limited. Considering the reconstruction of the valve implanted to the patients would improve the replication of the patients' hemodynamics.

Future developments of this study could concern:

- A more extensive study on the calibration of the valve model, in order to reach optimal values of opening and closing both for Patient 1 and Patient 2 in all scenarios.
- The coupling of the 3D model of the pulmonary artery with the lumped parameters model of the circulation. The addition of the feedback between the 3D model of the pulmonary artery and the 0D model of the circulation would allow to apply more realistic boundary conditions to the artificial boundaries of the 3D geometry; although the pressure sets found using the one-way approach are already satisfying.
- The influence of the stented valve positioning on the flow patterns established after pulmonary valve replacement.
- A more extensive study, collecting more patient-specific models, in order to analyse the different outcome of the study with respect to the geometry of the pulmonary artery considered or to the different boundary conditions used. Indeed, to each patient will correspond different clinical data to be used in the calibration of the lumped parameters model of the circulation.

Bibliography

[1] Tetralogy of Fallot. URL `https://www.kidsheartshouston.com/answers/21865-tetralogy-of-fallot`.

[2] P. C. Africa. lifex: A flexible, high performance library for the numerical solution of complex finite element problems. *SoftwareX*, 20:101252, 2022.

[3] C. Apitz, G. D. Webb, and A. N. Redington. Tetralogy of Fallot. *The Lancet*, 374: 1462–1471. doi: 10.1016/S0140. URL `www.thelancet.com`.

[4] D. Arndt, W. Bangerth, B. Blais, M. Fehling, R. Gassmöller, T. Heister, L. Heltai, U. Köcher, M. Kronbichler, M. Maier, P. Munch, J.-P. Pelteret, S. Proell, K. Simon, B. Turcksin, D. Wells, and J. Zhang. The `deal.II` library, version 9.3. *Journal of Numerical Mathematics*, 29(3):171–186, 2021.

[5] D. Arndt, W. Bangerth, D. Davydov, T. Heister, L. Heltai, M. Kronbichler, M. Maier, J.-P. Pelteret, B. Turcksin, and D. Wells. The deal.II finite element library: Design, features, and insights. *Computers & Mathematics with Applications*, 81:407–422, 2021. ISSN 0898-1221.

[6] M. Astorino, J. Hamers, S. C. Shadden, and J. F. Gerbeau. A robust and efficient valve model based on resistive immersed surfaces. *International Journal for Numerical Methods in Biomedical Engineering*, 28:937–959, 2012. ISSN 20407947. doi: 10.1002/cnm.2474.

[7] F. Bailliard and R. H. Anderson. Tetralogy of Fallot. *Orphanet Journal of Rare Diseases*, 4, 2009. ISSN 17501172. doi: 10.1186/1750-1172-4-2.

[8] H. Baumgartner, P. Bonhoeffer, N. M. D. Groot, F. D. Haan, J. E. Deanfield, N. Galie, M. A. Gatzoulis, C. Gohlke-Baerwolf, H. Kaemmerer, P. Kilner, F. Meijboom, B. J. Mulder, E. Oechslin, J. M. Oliver, A. Serraf, A. Szatmari, E. Thaulow, P. R. Vouhe, E. Walma, A. Vahanian, A. Auricchio, J. Bax, C. Ceconi, V. Dean, G. Filippatos, C. Funck-Brentano, R. Hobbs, P. Kearney, T. McDonagh, B. A. Popescu, Z. Reiner, U. Sechtem, P. A. Sirnes, M. Tendera, P. Vardas, P. Widimsky, L. Swan, F. Andreotti, M. Beghetti, M. Borggrefe, A. Bozio, S. Brecker, W. Budts,

J. Hess, R. Hirsch, G. Jondeau, J. Kokkonen, M. Kozelj, S. Kucukoglu, M. Laan, C. Lionis, I. Metreveli, P. Moons, P. G. Pieper, V. Pilossoff, J. Popelova, S. Price, J. Roos-Hesselink, M. S. Uva, P. Tornos, P. T. Trindade, H. Ukkonen, H. Walker, G. D. Webb, and J. Westby. Esc guidelines for the management of grown-up congenital heart disease (new version 2010), 12 2010. ISSN 0195668X.

[9] Y. Bazilevs, V. Calo, J. Cottrell, T. Hughes, A. Reali, and G. Scovazzi. Variational multiscale residual-based turbulence modeling for large eddy simulation of incompressible flows. *Computer methods in applied mechanics and engineering*, 197(1-4): 173–201, 2007.

[10] B. Becsek, L. Pietrasanta, and D. Obrist. Turbulent systolic flow downstream of a bioprosthetic aortic valve: velocity spectra, wall shear stresses, and turbulent dissipation rates. *Frontiers in physiology*, 11, 2020.

[11] L. Bennati, C. Vergara, V. Giambruno, I. Fumagalli, A. F. Corno, A. Quarteroni, G. Puppini, and G. B. Luciani. An image-based computational fluid dynamics study of mitral regurgitation in presence of prolapse, 2022. URL `http://mox.polimi.it`.

[12] C. Bertoglio and A. Caiazzo. A tangential regularization method for backflow stabilization in hemodynamics. *Journal of Computational Physics*, 261:162–171, 2014.

[13] N. Bessonov, A. Sequeira, S. Simakov, Y. Vassilevskii, and V. Volpert. Methods of blood flow modelling. *Mathematical Modelling of Natural Phenomena*, 11:1–25, 2016. ISSN 17606101. doi: 10.1051/mmnp/201611101.

[14] M. Bucelli, L. Dede', A. Quarteroni, and C. Vergara. Partitioned and monolithic algorithms for the numerical solution of cardiac fluid-structure interaction. *Communications in Computational Physics*, 32(5):1217–1256, 2022.

[15] M. Bucelli, A. Zingaro, P. C. Africa, I. Fumagalli, L. Dede', and A. M. Quarteroni. A mathematical model that integrates cardiac electrophysiology, mechanics and fluid dynamics: application to the human left heart. *International Journal for Numerical Methods in Biomedical Engineering*, 39(3):e3678, 2023.

[16] E. R. V. Buechel, H. H. Dave, C. J. Kellenberger, A. Dodge-Khatami, R. Pretre, F. Berger, and U. Bauersfeld. Remodelling of the right ventricle after early pulmonary valve replacement in children with repaired tetralogy of Fallot: assessment by cardiovascular magnetic resonance. *European heart journal*, 26(24):2721–2727, 2005.

[17] F. Capuano, Y. H. Loke, and E. Balaras. Blood flow dynamics at the pulmonary artery bifurcation. *Fluids*, 4, 11 2019. ISSN 23115521. doi: 10.3390/fluids4040190.

[18] P. E. F. Cavalcanti, M. P. B. O. Sá, C. A. Santos, I. M. Esmeraldo, R. R. D. Escobar, A. M. D. Menezes, O. M. D. Azevedo, F. P. D. V. Silva, R. F. D. A. Lins, and R. D. C. Lima. Pulmonary valve replacement after operative repair of Tetralogy of Fallot: Meta-analysis and meta-regression of 3,118 patients from 48 studies, 12 2013. ISSN 15583597.

[19] F. Conti and A. Colantuoni. *Fisiologia Medica*, volume 2. second edition, 2010.

[20] G. Costa, E. Criscione, D. Todaro, C. Tamburino, and M. Barbanti. Long-term transcatheter aortic valve durability. *Interventional Cardiology Review*, 14(2):62, 2019.

[21] E. S. Dacatra. Computational study of the hemodynamics in healthy and diseased pulmonary arteries, 2022. Tesi di Laurea Magistrale in Mathematical Engineering-Ingegneria Matematica, Politecnico di Milano (advisors: C Vergara and Ivan Fumagalli and Stefano Maria Marianeschi.

[22] Deal.II. URL `https://www.dealii.org/`.

[23] S. Di Gregorio, C. Vergara, G. M. Pelagi, A. Baggiano, P. Zunino, M. Guglielmo, L. Fusini, G. Muscogiuri, A. Rossi, M. G. Rabbat, et al. Prediction of myocardial blood flow under stress conditions by means of a computational model. *European Journal of Nuclear Medicine and Molecular Imaging*, pages 1–12, 2022.

[24] M. Fathallah and R. A. Krasuski. Pulmonic valve disease: Review of pathology and current treatment options, 11 2017. ISSN 15343170.

[25] M. Fedele and A. Quarteroni. Polygonal surface processing and mesh generation tools for the numerical simulation of the cardiac function. *International Journal for Numerical Methods in Biomedical Engineering*, 37(4), 2021. doi: 10.1002/cnm.3435.

[26] M. Fedele, E. Faggiano, L. Dedè, and A. Quarteroni. A patient-specific aortic valve model based on moving resistive immersed implicit surfaces. *Biomechanics and Modeling in Mechanobiology*, 16:1779–1803, 10 2017. ISSN 16177940. doi: 10.1007/s10237-017-0919-1.

[27] M. Fedele, R. Piersanti, F. Regazzoni, M. Salvador, P. C. Africa, M. Bucelli, A. Zingaro, L. Dede', and A. Quarteroni. A comprehensive and biophysically detailed computational model of the whole human heart electromechanics. *Computer Methods in Applied Mechanics and Engineering (in press)*, 2022.

[28] M. A. Fernández, J. F. Gerbeau, and V. Martin. Numerical simulation of blood flows through a porous interface. *Mathematical Modelling and Numerical Analysis*, 42:961–990, 11 2008. ISSN 0764583X. doi: 10.1051/m2an:2008031.

[29] G. Fiore, U. Morbiducci, A. Redaelli, and F.Montevecchi. *Biomeccanica, analisi multiscala di tessuti biologici.* first edition, 2012.

[30] L. Formaggia, F. Nobile, A. Quarteroni, and A. Veneziani. Computing and visualization in science multiscale modelling of the circulatory system: a preliminary analysis, 1999.

[31] J. Forman, R. Beech, L. Slugantz, and A. Donnellan. A review of Tetralogy of Fallot and postoperative management, 9 2019. ISSN 08995885.

[32] D. Forti and L. Dedè. Semi-implicit BDF time discretization of the navier–stokes equations with VMS-LES modeling in a high performance computing framework. *Computers & Fluids*, 117:168–182, 2015.

[33] A. Frigiola, V. Tsang, J. Nordmeyer, P. Lurz, C. van Doorn, A. M. Taylor, P. Bonhoeffer, and M. de Leval. Current approaches to pulmonary regurgitation. *European Journal of Cardio-thoracic Surgery*, 34:576–581, 9 2008. ISSN 10107940. doi: 10.1016/j.ejcts.2008.04.046.

[34] I. Fumagalli. A reduced 3D-0D fsi model of the aortic valve including leaflets curvature. *arXiv preprint arXiv:2106.00571*, 2021. URL `http://arxiv.org/abs/2106.00571`.

[35] I. Fumagalli, M. Fedele, C. Vergara, L. Dede', S. Ippolito, F. Nicolò, C. Antona, R. Scrofani, and A. Quarteroni. An image-based computational hemodynamics study of the systolic anterior motion of the mitral valve. *Computers in Biology and Medicine*, 123, 8 2020. ISSN 18790534. doi: 10.1016/j.compbiomed.2020.103922.

[36] I. Fumagalli, R. Polidori, F. Renzi, L. Fusini, A. Quarteroni, G. Pontone, and C. Vergara. Fluid-structure interaction analysis of transcatheter aortic valve implantation. *International Journal for Numerical Methods in Biomedical Engineering*, accepted: e3704, 2022.

[37] J. Gales, R. A. Krasuski, and G. A. Fleming. Transcatheter valve replacement for right-sided valve disease in congenital heart patients, 9 2018. ISSN 18731740.

[38] T. Geva, K. Gauvreau, A. J. Powell, F. Cecchin, J. Rhodes, J. Geva, and P. D. Nido. Randomized trial of pulmonary valve replacement with and without right

ventricular remodeling surgery. *Circulation*, 122, 9 2010. ISSN 00097322. doi: 10.1161/CIRCULATIONAHA.110.951178.

[39] S. Ghiselli, C. Carro, N. Uricchio, G. Annoni, and S. M. Marianeschi. Mid-to long-term follow-up of pulmonary valve replacement with biointegral injectable valve. *European Journal of Cardio-thoracic Surgery*, 59:325–332, 2 2021. ISSN 1873734X. doi: 10.1093/ejcts/ezaa337.

[40] R. P. Ghosh, G. Marom, M. Bianchi, K. D'souza, W. Zietak, and D. Bluestein. Numerical evaluation of transcatheter aortic valve performance during heart beating and its post-deployment fluid-structure interaction analysis. *Biomechanics and modeling in mechanobiology*, 19(5):1725–1740, 2020.

[41] B. E. Griffith. Immersed boundary model of aortic heart valve dynamics with physiological driving and loading conditions. *International Journal for Numerical Methods in Biomedical Engineering*, 28:317–345, 2012. ISSN 20407947. doi: 10.1002/cnm.1445.

[42] M. Guglielmo, L. Fusini, M. Muratori, G. Tamborini, V. Mantegazza, D. Andreini, A. Annoni, M. Babbaro, A. Baggiano, E. Conte, et al. Computed tomography predictors of structural valve degeneration in patients undergoing transcatheter aortic valve implantation with balloon-expandable prostheses. *European Radiology*, pages 1–11, 2022.

[43] M. Handke, G. Heinrichs, F. Beyersdorf, M. Olschewski, C. Bode, and A. Geibel. In vivo analysis of aortic valve dynamics by transesophageal 3-dimensional echocardiography with high temporal resolution. *The Journal of thoracic and cardiovascular surgery*, 125(6):1412–1419, 2003.

[44] C. H. Huber, M. Hurni, V. Tsang, and L. K. von Segesser. Valved stents for transapical pulmonary valve replacement. *Journal of Thoracic and Cardiovascular Surgery*, 137:914–918, 4 2009. ISSN 00225223. doi: 10.1016/j.jtcvs.2008.09.024.

[45] S. N. Jonas, S. J. Kligerman, A. P. Burke, A. A. Frazier, and C. S. White. Pulmonary valve anatomy and abnormalities: A pictorial essay of radiography, computed tomography (CT), and magnetic resonance imaging (MRI). *Journal of Thoracic Imaging*, 31:W4–W12, 2016. ISSN 15360237. doi: 10.1097/RTI.0000000000000182.

[46] T. Katogi. Ross procedure: Prognosis of pulmonary autografts, 2012. ISSN 13411098.

[47] A. Keenon, E. D. Crouch, J. E. Faber, and G. A. Stouffer. Normal hemodynamics. *Cardiovascular Hemodynamics for the Clinician*, pages 37–55, 2017.

[48] A. G. Kidane, G. Burriesci, P. Cornejo, A. Dooley, S. Sarkar, P. Bonhoeffer, M. Edirisinghe, and A. M. Seifalian. Current developments and future prospects for heart valve replacement therapy, 1 2009. ISSN 15524973.

[49] T. Korakianitis and Y. Shi. Numerical simulation of cardiovascular dynamics with healthy and diseased heart valves. *Journal of Biomechanics*, 39:1964–1982, 2006. ISSN 00219290. doi: 10.1016/j.jbiomech.2005.06.016.

[50] A. E. Kostyunin, A. E. Yuzhalin, M. A. Rezvova, E. A. Ovcharenko, T. V. Glushkova, and A. G. Kutikhin. Degeneration of bioprosthetic heart valves: update 2020. *Journal of the American Heart Association*, 9(19):e018506, 2020.

[51] G. Kovacs, A. Berghold, S. Scheidl, and H. Olschewski. Pulmonary arterial pressure during rest and exercise in healthy subjects: a systematic review. *European Respiratory Journal*, 34(4):888–894, 2009.

[52] M. B. Leon, C. R. Smith, M. Mack, D. C. Miller, J. W. Moses, L. G. Svensson, E. M. Tuzcu, J. G. Webb, G. P. Fontana, R. R. Makkar, D. L. Brown, P. C. Block, R. A. Guyton, A. D. Pichard, J. E. Bavaria, H. C. Herrmann, P. S. Douglas, J. L. Petersen, J. J. Akin, W. N. Anderson, D. Wang, and S. Pocock. Transcatheter aortic-valve implantation for aortic stenosis in patients who cannot undergo surgery. *New England Journal of Medicine*, 363:1597–1607, 10 2010. ISSN 0028-4793. doi: 10.1056/nejmoa1008232.

[53] Life^{x}. URL `https://lifex.gitlab.io/lifex/`.

[54] G. Luraghi, F. Migliavacca, A. García-González, C. Chiastra, A. Rossi, D. Cao, G. Stefanini, and J. F. R. Matas. On the modeling of patient-specific transcatheter aortic valve replacement: a fluid–structure interaction approach. *Cardiovascular engineering and technology*, 10(3):437–455, 2019.

[55] G. Luraghi, J. F. R. Matas, M. Beretta, N. Chiozzi, L. Iannetti, and F. Migliavacca. The impact of calcification patterns in transcatheter aortic valve performance: a fluid-structure interaction analysis. *Computer Methods in Biomechanics and Biomedical Engineering*, pages 1–9, 2020.

[56] A. M. Maceira, S. K. Prasad, M. Khan, and D. J. Pennell. Reference right ventricular systolic and diastolic function normalized to age, gender and body surface area from steady-state free precession cardiovascular magnetic resonance. *European Heart Journal*, 27:2879–2888, 12 2006. ISSN 0195668X. doi: 10.1093/eurheartj/ehl336.

[57] F. Marcinno', A. Zingaro, I. Fumagalli, L. Dede', and C. Vergara. A computational

study of blood flow dynamics in the pulmonary arteries, 2021. URL `http://mox.polimi.it`.

[58] S. Marianeschi. Application of artificial valves in right ventricular tract reconstruction, Dec 2020. URL `https://peters-surgical.com/event/title-event/`.

[59] MathWorks. Matlab. URL `https://it.mathworks.com/products/matlab.html`.

[60] A. Messina. Coupling between 3D hemodynamics and reduced immersed valve dynamics for the pulmonary circulation, 2022. Tesi di Laurea Magistrale in Mathematical Engineering-Ingegneria Matematica, Politecnico di Milano (advisors:C Vergara and Ivan Fumagalli).

[61] M. Muratori, L. Fusini, G. Tamborini, P. Gripari, S. Ghulam Ali, M. Mapelli, F. Fabbiocchi, P. Trabattoni, M. Roberto, M. Agrifoglio, et al. Five-year echocardiographic follow-up after tavi: structural and functional changes of a balloon-expandable prosthetic aortic valve. *European Heart Journal-Cardiovascular Imaging*, 19(4):389–397, 2018.

[62] National, Institute, of, Biomedical, Imaging, Bioengineering, and (NIBIB). Computed tomography (CT). URL `https://www.nibib.nih.gov/science-education/science-topics/computed-tomography-ct`.

[63] F. Nicoud, H. B. Toda, O. Cabrit, S. Bose, and J. Lee. Using singular values to build a subgrid-scale model for large eddy simulations. *Physics of fluids*, 23(8):085106, 2011.

[64] T. Oosterhof, A. V. Straten, H. W. Vliegen, F. J. Meijboom, A. P. V. Dijk, A. M. Spijkerboer, B. J. Bouma, A. H. Zwinderman, M. G. Hazekamp, A. D. Roos, and B. J. Mulder. Preoperative thresholds for pulmonary valve replacement in patients with corrected tetralogy of Fallot using cardiovascular magnetic resonance. *Circulation*, 116:545–551, 7 2007. ISSN 00097322. doi: 10.1161/CIRCULATIONAHA.106.659664.

[65] Paraview. URL `https://www.paraview.org/`.

[66] G. Polazzo, A. Sapienza, and A. Zaccaria. Ricostruzione geometrica dell'arteria polmonare in pazienti con valvola autoespandibile., 2021. Laurea Triennale, Politecnico di Milano.

[67] H. A. Qethamy, T. Momenah, R. E. Oakley, A. A. Redhyan, M. Tageldin, and Y. A. Faraidi. Minimally invasive transventricular implantation of pulmonary xenograft. *Journal of Cardiac Surgery*, 23:339–340, 7 2008. ISSN 08860440. doi: 10.1111/j.1540-8191.2008.00612.x.

[68] A. Quarteroni, A. Veneziani, and C. Vergara. Geometric multiscale modeling of the cardiovascular system, between theory and practice. *Computer Methods in Applied Mechanics and Engineering*, 302:193–252, 4 2016. ISSN 00457825. doi: 10.1016/j.cma.2016.01.007.

[69] A. Quarteroni, T. Lassila, S. Rossi, and R. Ruiz-Baier. Integrated heart—coupling multiscale and multiphysics models for the simulation of the cardiac function. *Computer Methods in Applied Mechanics and Engineering*, 314:345–407, 2 2017. ISSN 00457825. doi: 10.1016/j.cma.2016.05.031.

[70] A. Quarteroni, A. Manzoni, and C. Vergara. The cardiovascular system: Mathematical modelling, numerical algorithms and clinical applications. *Acta Numerica*, 26: 365–590, 5 2017. ISSN 14740508. doi: 10.1017/S0962492917000046.

[71] A. Quarteroni, L. Dede', A. Manzoni, C. Vergara, et al. *Mathematical modelling of the human cardiovascular system: data, numerical approximation, clinical applications*, volume 33. Cambridge University Press, 2019.

[72] F. S. A. Quarteroni, F. Saleri, and P. Gervasio. *Calcolo scientifico*. Springer, 2008.

[73] F. Regazzoni, M. Salvador, P. Africa, M. Fedele, L. Dedè, and A. Quarteroni. A cardiac electromechanical model coupled with a lumped-parameter model for closed-loop blood circulation. *Journal of Computational Physics*, 457:111083, 2022. ISSN 0021-9991. doi: https://doi.org/10.1016/j.jcp.2022.111083. URL `https://www.sciencedirect.com/science/article/pii/S0021999122001450`.

[74] E. Ruckdeschel and Y. Y. Kim. Pulmonary valve stenosis in the adult patient: pathophysiology, diagnosis and management. *Heart*, 105:414–422, 3 2019. ISSN 1468201X. doi: 10.1136/heartjnl-2017-312743.

[75] M. S. Sacks, W. D. Merryman, and D. E. Schmidt. On the biomechanics of heart valve function, 8 2009. ISSN 00219290.

[76] S. M. Said, R. D. Mainwaring, M. Ma, T. A. Tacy, and F. L. Hanley. Pulmonary valve repair for patients with acquired pulmonary valve insufficiency. *Annals of Thoracic Surgery*, 101:2294–2301, 6 2016. ISSN 15526259. doi: 10.1016/j.athoracsur.2016.01.035.

[77] M. Salvador, M. Fedele, P. C. Africa, E. Sung, A. Prakosa, J. Chrispin, N. Trayanova, A. Quarteroni, et al. Electromechanical modeling of human ventricles with ischemic cardiomyopathy: numerical simulations in sinus rhythm and under arrhythmia. *Computers in Biology and Medicine*, 136:104674, 2021.

[78] M. Sarkar and V. Prabhu. Basics of cardiopulmonary bypass, 9 2017. ISSN 00195049.

[79] A. M. Sharkey and A. Sharma. Tetralogy of fallot: Anatomic variants and their impact on surgical management, 6 2012. ISSN 10892532.

[80] B. J. Shiland. *Mastering Healthcare Terminology*. Elsevier Health Sciences, 6th edition, 2019.

[81] S. Shimizu, D. Une, T. Kawada, Y. Hayama, A. Kamiya, T. Shishido, and M. Sugimachi. Lumped parameter model for hemodynamic simulation of congenital heart diseases, 3 2018. ISSN 18806546.

[82] C. R. Smith, M. B. Leon, M. J. Mack, D. Craig, J. W. Moses, L. G. Svensson, E. M. Tuzcu, J. G. Webb, G. P. Fontana, R. R. Makkar, M. Williams, T. Dewey, S. Kapadia, V. Babaliaros, V. H. Thourani, P. Corso, A. D. Pichard, J. E. Bavaria, H. C. Herrmann, J. J. Akin, W. N. Anderson, D. Wang, and S. J. Pocock. Transcatheter versus surgical aortic-valve replacement in high-risk patients, 2011.

[83] J. J. Takkenberg, L. M. Klieverik, P. H. Schoof, R. J. V. Suylen, L. A. V. Herwerden, P. E. Zondervan, J. W. Roos-Hesselink, M. J. Eijkemans, M. H. Yacoub, and A. J. Bogers. The ross procedure: A systematic review and meta-analysis, 1 2009. ISSN 00097322.

[84] B. T. Tang, T. A. Fonte, F. P. Chan, P. S. Tsao, J. A. Feinstein, and C. A. Taylor. Three-dimensional hemodynamics in the human pulmonary arteries under resting and exercise conditions. *Annals of Biomedical Engineering*, 39:347–358, 1 2011. ISSN 00906964. doi: 10.1007/s10439-010-0124-1.

[85] B. T. Tang, S. S. Pickard, F. P. Chan, P. S. Tsao, C. A. Taylor, and J. A. Feinstein. Wall shear stress is decreased in the pulmonary arteries of patients with pulmonary arterial hypertension: An image-based, computational fluid dynamics study. *Pulmonary Circulation*, 2:470–476, 10 2012. ISSN 20458940. doi: 10.4103/2045-8932.105035.

[86] G. Tasca, R. Vismara, F. Trinca, B. Riva, A. Gamba, and E. Lobiati. Opening/closing pattern of trifecta and freestyle valves versus native aortic valve: Are stentless valves more physiologic than a stented valve? *Journal of Cardiac Surgery*, 32:680–685, 11 2017. ISSN 15408191. doi: 10.1111/jocs.13231.

[87] J. Therrien, Y. Provost, N. Merchant, W. Williams, J. Colman, and G. Webb. Optimal timing for pulmonary valve replacement in adults after tetralogy of Fallot repair. *The American journal of cardiology*, 95(6):779–782, 2005.

[88] G. J. Tortora and B. Derrickson. *Introduction to the human body : the essentials of anatomy and physiology*. John Wiley Sons, 8th edition, 2010.

[89] VMTK, Vascular, Modeling, and Toolkit. URL `http://www.vmtk.org/index.html`.

[90] E. Votta, T. B. Le, M. Stevanella, L. Fusini, E. G. Caiani, A. Redaelli, and F. Sotiropoulos. Toward patient-specific simulations of cardiac valves: State-of-the-art and future directions. *Journal of Biomechanics*, 46:217–228, 1 2013. ISSN 00219290. doi: 10.1016/j.jbiomech.2012.10.026.

[91] S. Wang, S. Wang, Q. Zhu, Y. Wang, G. Li, F. Kong, J. Yang, and C. Ma. Reference values of right ventricular volumes and ejection fraction by three-dimensional echocardiography in adults: A systematic review and meta-analysis, 2021. ISSN 2297055X.

[92] Y. Yokoyama, T. Kuno, N. Toyoda, T. Fujisaki, H. Takagi, S. Itagaki, M. Ibrahim, M. Ouzounian, I. El-Hamamsy, and S. Fukuhara. Ross procedure versus mechanical versus bioprosthetic aortic valve replacement: A network meta-analysis, 8 2023. ISSN 20479980.

[93] A. Zingaro, I. Fumagalli, L. Dede', M. Fedele, P. C. Africa, A. F. Corno, and A. M. Quarteroni. A geometric multiscale model for the numerical simulation of blood flow in the human left heart. *Discrete and Continous Dynamical System - S*, 15(8): 2391–2427, 2022.

[94] A. Zingaro, M. Bucelli, R. Piersanti, F. Regazzoni, L. Dede', and A. Quarteroni. An electromechanics-driven fluid dynamics model for the simulation of the whole human heart. *arXiv preprint arXiv:2301.02148*, 2023.

[95] Zygote. URL `http://www.zygote.com`.

List of Figures

List of Tables